JOURNAL OF CAVE AND KARST STUDIES

March 2020
Volume 82, Number 1
ISSN 1090-6924
A Publication of the National Speleological Society

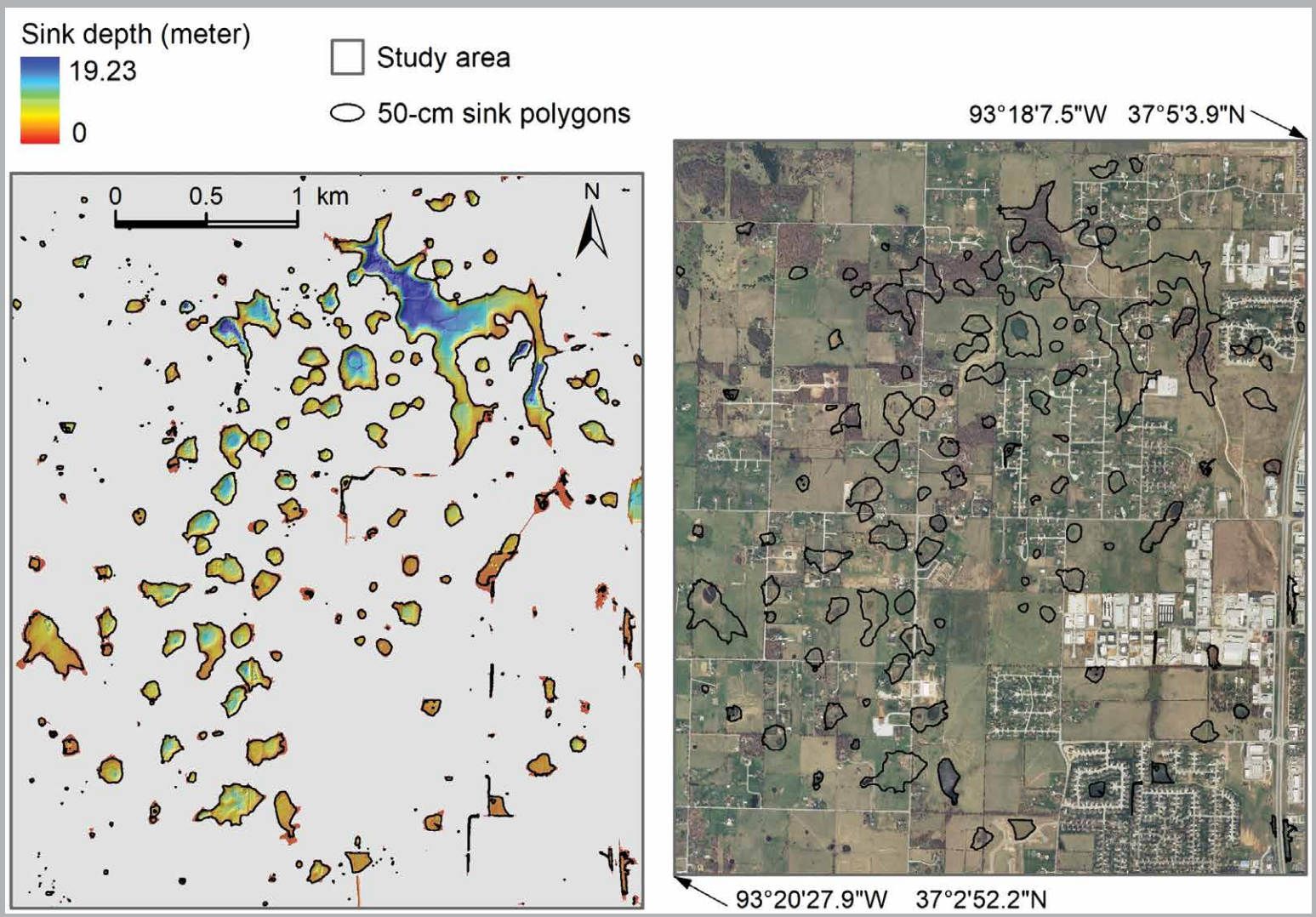

DEDICATED TO THE ADVANCEMENT OF SCIENCE, EDUCATION, EXPLORATION, AND CONSERVATION

Published By
The National Speleological Society

http://caves.org/pub/journal

Office
6001 Pulaski Pike NW
Huntsville, AL 35810 USA
Tel:256-852-1300
nss@caves.org

Editor-in-Chief
Malcolm S. Field
National Center of Environmental
Assessment (8623P)
Office of Research and Development
U.S. Environmental Protection Agency
1200 Pennsylvania Avenue NW
Washington, DC 20460-0001
703-347-8601 Voice 703-347-8692 Fax
field.malcolm@epa.gov

Production Editor
Scott A. Engel
Knoxville, TN
225-281-3914
saecaver@gmail.com

Journal Copy Editor

The *Journal of Cave and Karst Studies* , ISSN 1090-6924, CPM Number #40065056, is a multi-disciplinary, refereed journal published four times a year by the National Speleological Society. The *Journal* is available by open access on its website, or check the website for current print subscription rates. Back issues are available from the NSS office.

POSTMASTER: send address changes to the National Speleological Society Office listed above.

The Journal of Cave and Karst Studies is covered by the following ISI Thomson Services Science Citation Index Expanded, ISI Alerting Services, and Current Contents/Physical, Chemical, and Earth Sciences.

Front cover: Mapping sinkholes based on aerial imagery and GIS in Missouri. See Qiu et al. in this issue.

Xiaomin Qiu, Shuo-Sheng Wu, and Yan Chen. Sinkhole susceptibility assessment based on morphological, imagery, and contextual attributes derived from gis and imagery data. *Journal of Cave and Karst Studies*, v. 82, no. 1, p. 1-17. DOI:10.4311/2018ES0118

SINKHOLE SUSCEPTIBILITY ASSESSMENT BASED ON MORPHOLOGICAL, IMAGERY, AND CONTEXTUAL ATTRIBUTES DERIVED FROM GIS AND IMAGERY DATA

Xiaomin Qiu[1], Shuo-Sheng Wu[1,C], and Yan Chen[2]

Abstract

This study presents a GIS-based approach to efficiently assess sinkhole susceptibility based on their morphological and contextual attributes derived from GIS and imagery data. Using a 14-km^2 karst area in Nixa, Missouri as the study area, we first applied a sequence of GIS operations to extract sinks (i.e., topographic depressions), from bare-ground digital terrain models. We then derived three types of sink attributes from various GIS and imagery data, including four morphological attributes related to sink size, shape, depth, and terrain ruggedness; three imagery attributes denoting the impervious surface percentage, vegetation growth condition, and seasonal water conditions of sinks; and seven contextual attributes related to land use, population density, neighborhood sink density, hydrological flow, groundwater yield, bedrock depth, and historical sinkhole records. Sinks were ranked by each of the 14 attributes and assigned corresponding susceptibility scores, then combined by specified weights. The results identified high-priority sinkholes for mitigation activities or for further field-based inspection. The proposed computerized approach for sinkhole susceptibility ranking can be effectively used as a first-stage sinkhole examination to maximize the use of limited resources for further comprehensive investigation.

Introduction

Sinkholes are common geologic phenomena in karst landscapes where the dominant geological mechanism is the dissolution of soluble rocks, mostly carbonates, rather than mechanical erosion (Gutiérrez et al., 2014). Sinkholes are usually circular to ellipsoidal funnel-shaped depressions on the land surface; the size can be from several centimeters to hundreds of meters, and the depth can be from a few meters to tens of meters (Gutiérrez et al., 2008; Zisman, 2008; Parise, 2010).

While the development of sinkholes involves complex interaction of soil, rock, and groundwater that is unique for each site, two types of sinkholes can be distinguished, including solution sinkholes and subsidence sinkholes (Gutiérrez et al., 2008). Solution sinkholes are created by differential dissolution and lowering of the ground surface where soluble rocks are exposed at or near the surface. Subsidence sinkholes are formed by subsurface dissolution and downward gravitational movement of the cover materials (Gutiérrez et al., 2014).

Subsidence sinkholes can be classified on the basis of the affected materials and the formation processes (Gutiérrez et al., 2008, 2014). The affected materials may include soil cover, non-karst caprock, and karst bedrock; and the formation processes may include collapse, sagging, and suffosion. When the creation of a sinkhole involves more than one material or process, the sinkhole can be described with the dominant material and process followed by the secondary one (e.g., cover sagging and suffosion sinkholes, which are the common type of sinkholes in the study area of this research).

Sinkhole subsidence can cause severe damage to roads and buildings. They also pose threats to human beings and livestock. Assessing sinkhole risk and the potential hazard is critical for hazard mitigation and management (Parise, 2015a; Parise et al., 2015). Hazard analysis can be broadly classified into quantitative, qualitative, and semi-quantitative methods (Lee and Jones, 2004; De León and Carlos, 2006; Van Westen, 2013). The quantitative method aims to quantify the hazard probability or predict losses by deriving numerical expressions of the relationships between hazard parameters and relevant variables. Statistical analysis, such as multiple regression analysis and discriminant analysis, are often applied to build relationship models (Dai et al., 2002). Examples of quantitative analysis includes the studies by Komac (2006), Molina et al. (2010), Sarkar et al. (2010), and Schmidt et al. (2011).

The qualitative method adopts a heuristic approach to estimate potential hazard from relevant factors based on the knowledge and experience of the experts. The method often includes the use of index maps and logical analytical models (Chalkias et al., 2016) and describes hazard risk and vulnerability in qualitative terms, such as high, medium, and low (De León and Carlos, 2006). Examples of qualitative analysis include the studies by Barredo et al. (2000), Van Westen et al. (2003), and Abella and Van Westen (2008).

The semi-quantitative method hazard analysis estimates potential hazard by converting hazard variables into indices and combining them based on the weights determined by expert judgement (Nsengiyumva et al., 2018). The

[1]Department of Geography, Geology and Planning, Missouri State University
[2]School of Environmental Sciences and Engineering, Donghua University, Shanghai, China
[C] Corresponding author: sw1020@gmail.com

combined hazard values may be further divided into different numbers of classes to be used for different purposes (Abella and Van Westen, 2008). This method often requires varied degrees of grouping, standardizing, indexing, and weighting for input variables. Example of semi-quantitative analysis include the studies by Peduzzi et al. (2005, 2009), Abella and vanWesten (2007), Wati et al. (2010), Feizizadeh and Blaschke (2014), Chalkias et al. (2014, 2016), and Nsengiyumva et al. (2018).

As this study adopts a semi-quantitative hazard analysis method, the advantages and limitations of this method are discussed in more detail. The main advantage of the semi-quantitative method is that it can reasonably rely on existing datasets and does not require costly field data as needed for the quantitative method (Anderson, 2013; Nsengiyumva, 2018). Furthermore, by using the grouping and weighting approach, qualitative and categorical data can be conveniently incorporated and combined with quantitative information.

One problem with the semi-quantitative method is the high degree of simplification in grouping and indexing procedures (Dai et al., 2002). Another limitation is the subjectivity of weightings and the reproducibility of results (Anderson, 2013). Specifically, since the determination of variable weights relies on expert knowledge, it is difficult to test the relative efficacy of one expert's weightings over the other's, and the chosen weightings would have limited reproducibility.

A major difference between this study and other semi-quantitative hazard studies is that this study explicitly considers the quality of the spatial datasets for deriving hazard variables in determining suitable variable weights, in addition to taking hazard implication of the variables into account. Specifically, as our hazard variables are all derived from GIS and imagery data, the precision/quality of spatial data plays an important role in the reliability of the derived variables for predicting hazard. While past semi-quantitative studies often only consider hazard implication of variables in determining their weights, this study contributes to the field of hazard analysis by explicitly accounting for spatial data quality in the weighting procedures.

It is worth noting that the terms susceptibility assessment and hazard assessment may be explicitly differentiated. Specifically, susceptibility assessment indicates the relative probability of sinkhole incidence without referring to any time interval, while hazard assessment provides a quantitative measure of such probability within a time interval (Gutiérrez et al., 2008b; Galve et al., 2009a). In other words, the generic concept of susceptibility describes the potential that a sinkhole incidence may occur in a certain area in an infinite time interval (Taheri et al., 2015; Ciotolia et al., 2016). As this study does not analyze sinkhole data of different time intervals, we will use the term susceptibility assessment instead of hazard assessment for the rest of the article.

Traditionally sinkholes are identified through field-based investigation by probing/boring activities (Zisman, 2001; Bullock and Dillman, 2003; Del Prete et al., 2010; Festa et al., 2012), area reconnaissance (Thomas and Roth, 1999) and geophysical applications (Krawczyk et al., 2012; Kaufmann, 2014). Large-scale sinkhole mapping may be accomplished by examining existing topographic maps or geologic maps and digitizing geologic features (Applegate, 2003; Gutiérrez et al., 2008; Galve et al.; 2009b). However, the results may lack the desired precision due to low resolution of the maps (Brinkmann et al., 2008; Basso et al., 2013). The reliability of this approach that digitizes features from existing maps also depends on the drafter's experience (Angel et al., 2004).

The advancement of digital photogrammetry and laser altimetry, particularly the improved data resolution, has increased the capability of sinkhole detection (Atzori et al., 2015; Intrieri et al., 2015; Al-Halbouni et al., 2017; Zumpano et al., 2019). The conventional approach is to delineate sinkholes through visual interpretation of digital imagery (Reese and Kochanov, 2003; Seale et al., 2008), while many studies have explored automatic approaches for extracting sinkholes or modeling sinkhole susceptibility (Zhu et al., 2014; Wall et al., 2017; Zumpano et al., 2019). For example, Stocks (2007) used an object-based approach to classify pixels of digital photos as sinkholes, by first grouping image pixels into meaningful objects of different hierarchies based on similar pixel statistics, and then classifying hierarchical objects into different land classes through iterated training processes. Galve et al. (2008) used a digital image classification approach to classify areas of different sinkhole susceptibility based on 27 geomorphologic, hydrogeological, and human factors derived from existing GIS data. Lamelas et al. (2008) used logistic regression to map sinkhole probability based on a variety of lithological, stratigraphic, geomorphological, and hydrological variables, as well as anthropogenic variables relevant to locations of man-made facilities. Siart et al. (2009) extracted sinkholes based on spectral values of satellite images; they then refined the results based on pre-defined size, slope, and elevation criteria for sinkholes.

Since the study area is situated in a hilly and vegetated karst terrain where field investigation is particularly labor-intensive and time-consuming, we propose a computerized assessment approach suitable for this type of landscape, and focus on sinkhole attributes that can be efficiently derived from common GIS and imagery data, including digital terrain models (DTMs), digital aerial photos, land parcel data, census population data, and well data. Specifically, four of the adopted sinkhole attributes are suitable for a hilly and vegetated landscape, including a terrain ruggedness index, a hydrological flow accumulation statistic, the Normalized Difference Vegetation Index (NDVI), and the seasonal surface water condition.

In addition to presenting a computerized assessment approach suitable for a hilly, vegetated karst terrain, and adopting sinkhole attributes that can be conveniently derived from common GIS and imagery data, this study contributes to sinkhole research by proposing three sinkhole attributes as hazard indicators that have not been used in past sinkhole susceptibility analyses. The three pioneering attributes are the terrain ruggedness index, the maximum hydrological flow accumulation, and the NDVI.

Study Area

An area approximately 14 km^2 (3.5 km by 4 km) in the northwest suburb of the city of Nixa, Missouri (Fig. 1), is used to demonstrate the methodology for sinkhole extraction and hazard assessment. The Nixa area is situated in the physiographic region of Springfield-Salem Plateaus that has a well-developed karst topography. The karst plateau is underlain by coarse-grained fossiliferous Mississippian-aged limestone and cherty limestone. Situated in a humid subtropical climate with overlying surficial soil up to 12-meter thick (Stohr et al., 1981), the region has hundreds of caves, springs, and sinkholes, with cover sagging and suffosion types of sinkholes most common.

The Nixa area sits on the drainage divide between the Finley River and the James River (Fig. 1). Flooding after heavy rain makes this area susceptible to erosion. Porter and Thomson (1975) documented a total of 266 sinkholes in the Nixa karst area. The current sinkhole database at Missouri Department of Natural Resources has approximately 300 sinkhole records, but only about three dozen are collapse sinkholes (Kaufmann, 2007; Gouzie and Pendergrass, 2009).

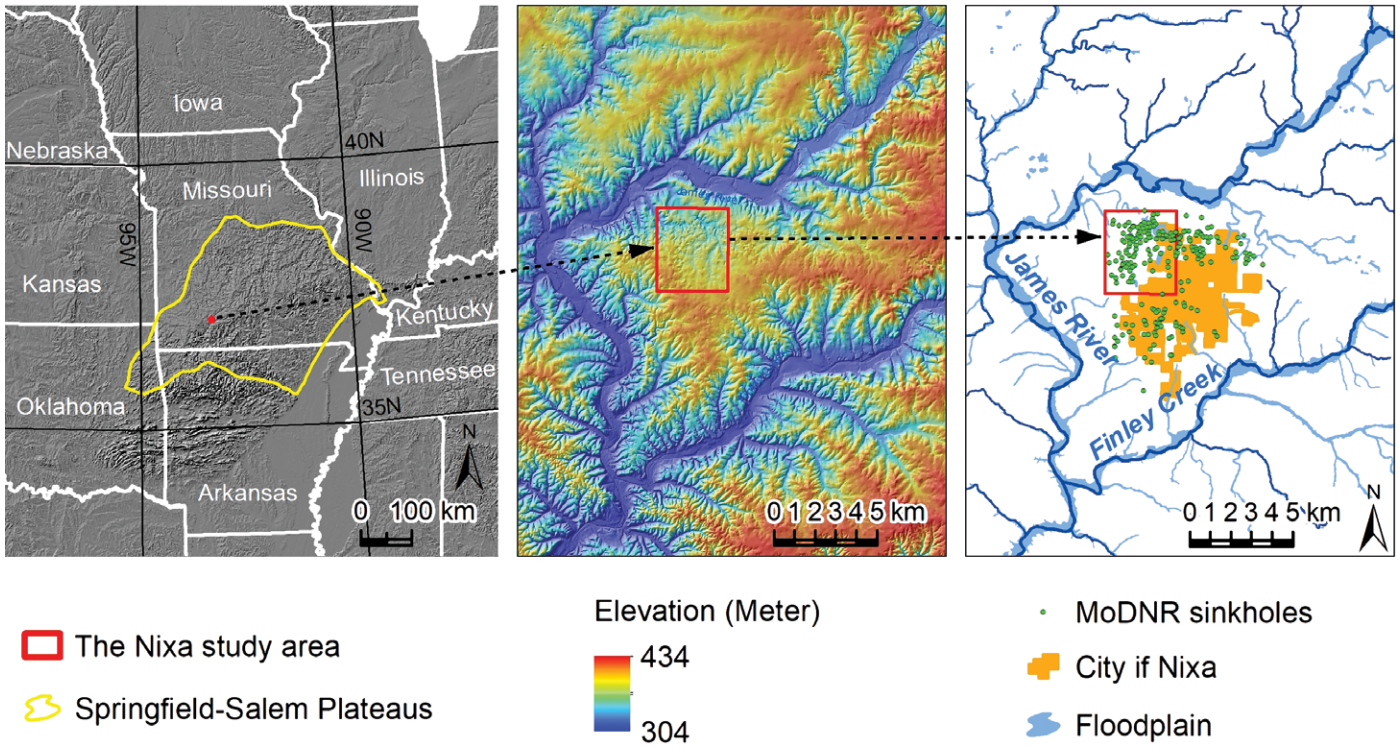

Figure 1. The Nixa study area (red rectangle) in the physiographic region of Springfield-Salem Plateaus (yellow polygon), with a hill-shaded relief map showing the topography (middle map), and a drainage map showing documented sinkholes in the area (right map).

Data Source

Data used in this study include DTMs, digital aerial photos, land use, building footprints, population, wells, and historical sinkhole data for the Nixa area. Firstly, we obtained bare-ground DTMs of one-meter spatial resolution from the U.S. Geological Survey (USGS) center at Rolla. The DTMs are originally derived from LiDAR remote-sensing data that were collect in 2006 and have been processed to remove vegetation and building points. The DTMs have a vertical accuracy of about 30 cm and a horizontal accuracy of about 50 cm. The DTMs will be used to extract sinks and to calculate the terrain ruggedness index and the hydrological flow accumulation for indicating potential sinkhole hazard.

We downloaded digital aerial photos of 3-band, 0.6-m resolution, taken during the winter of 2008 from the Missouri Spatial Data Information Service website (http://www.msdis.missouri.edu/). The 2008 photos will be used to derive seasonal water conditions during the winter and to compute impervious surface percentages, which will be used to infer human accessibility. We also downloaded digital aerial photos of four-band, one-meter resolution, taken during

the summer of 2009 from USGS The National Map website (http://nationalmap.gov). The 2009 photos will be used to derive seasonal water conditions during the summer and to calculate a vegetation growth index for indicating potential sinkhole hazard.

We obtained parcel zoning data from the Department of Planning and Development at Christian County, Missouri. The zoning data will be used to determine land uses for the areas where sinks are located. We downloaded building footprints data from ESRI ArcGIS Online (https://www.arcgis.com). The building footprints data, originally generated by Microsoft, will be used to refine/redistribute census block-level population from 2010 block-level population data from the U.S. Census Bureau American FactFinder website (https://factfinder.census.gov). The population data will be used to derive population density for the neighborhood area of sinks for indicating human exposure to potential sinkhole hazard. We further downloaded wells data and historical sinkhole data from Missouri Spatial Data Information Service. The wells data will be used to calculate a sinkhole risk measure based on the well yield (gallons per minute), and the historical sinkhole data will be used to calculate a sinkhole density measure to infer future hazard potential.

Analysis Methods

We used the per field classification technique in remote sensing (Wu et al., 2009) to derive attributes for sink polygons. The per field technique is commonly used for land use or land cover classification, in which areas within pre-determined polygonal fields are considered homogeneous and are classified based on relevant attributes of the fields (Aplin et al., 1999; Geneletti and Gorte, 2003). In this study, we used sink-depth isolines or their buffered areas as field boundaries for calculating the morphological, imagery, and contextual statistics for sinks.

In the following sections, we first describe the approach used for extracting sinks from DTMs using common GIS tools. We then explain the methods for deriving three types of sink attributes (Table 1) for sinkhole susceptibility assessment. Note that some of attributes are considered important in the sense of indicating human vulnerability to potential sinkhole incidences, instead of indicating the probability of geological activities of sinkholes (e.g., the rapid movement of soil cover).

Table 1. The three types of sink attributes and the used methods to assess the attributes.

Types	Attributes	Assessment Methods
Morphological	1. Size	1. Larger size → higher sinkhole susceptibility
	2. Shape complexity	2. Higher shape complexity → higher sinkhole susceptibility
	3. Depth to diameter ratio	3. Larger depth/diameter → higher sinkhole susceptibility
	4. Terrain ruggedness	4. More rugged → higher sinkhole susceptibility
Imagery	1. Impervious surface %	1. Higher impervious surface % → higher sinkhole susceptibility
	2. NDVI	2. Lower NDVI → higher sinkhole susceptibility
	3. Seasonal water condition	3. Impounded water → lower sinkhole susceptibility
Contextual	1. Land use	1. Commercial & residential land uses → higher sinkhole susceptibility
	2. Population density	2. Higher population density → higher sinkhole susceptibility
	3. Hydrological flow accumulation	3. Higher hydrological flow → higher sinkhole susceptibility
	4. Sink density	4. Higher sink density → higher sinkhole susceptibility
	5. Sinkhole record density	5. Higher sinkhole record density → higher sinkhole susceptibility
	6. Well yield	6. Higher well yield → higher sinkhole susceptibility
	7. Bedrock depth	7. Deeper bedrock → lower sinkhole susceptibility

Extracting Sinks from Bare-Ground DTMs

A sequence of GIS tools in ArcGIS software 10.4 is used to extract topographic depressions from the bare-ground DTMs. Specifically, we first filled the hydrological depressions on a DTM clipped to the study area. All depressions, regardless of depth, were filled in this process. Understanding that not applying a depth threshold at this stage of analysis would result in large amount of small and possibly artificial sinks being derived in later processes (Zhu et al., 2014; Qiu and Wu, 2017), we intended to later examine the size-distribution of the derived hydrological sinks to gain insight of the topography. The information will help decision making in selecting a suitable size threshold for filtering out reasonable sinks.

After creating the sink-filled DTM, we subtracted the smooth-surface DTM with the original bare-ground DTM to derive a sink-depth DTM (Figure 2). Sink-depth isolines of 50 cm were then computed from the sink-depth DTM, considering that the original DTM has a vertical accuracy of about 30 cm and the equivalent contour interval would be approximately 50 cm (USDA, 2011). Lastly, we converted the 50 cm sink-depth isolines to polygons, so they can be used as the field boundaries for deriving sink attributes. A total of 830 sinks were extracted for the study area.

We noted that there is one particularly large and irregularly-shaped sink in the north-east quadrangle of the study

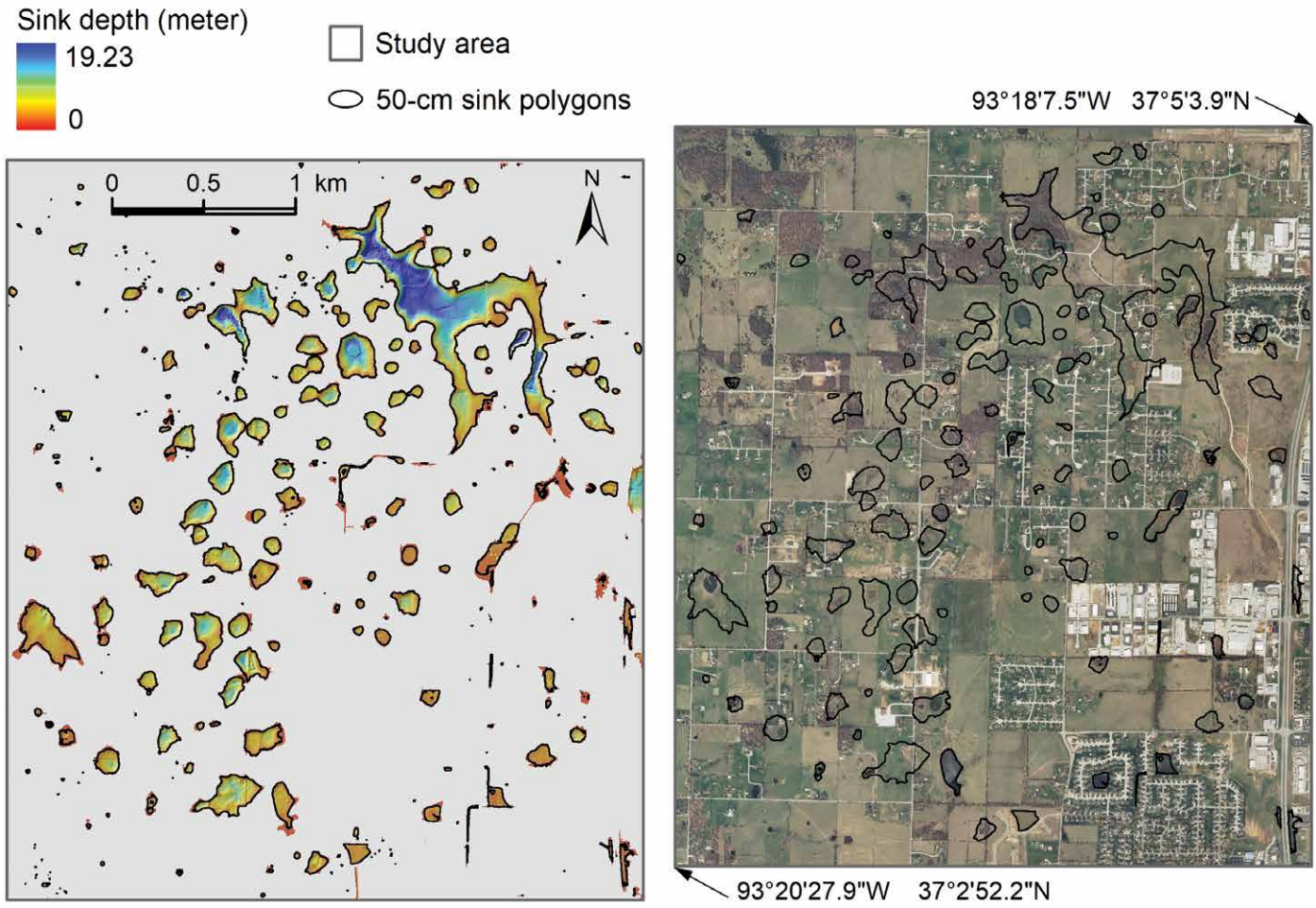

Figure 2. A hill-shaded sink-depth DTM with 50 cm depth sink polygons (left), and corresponding aerial photos with large sink polygons displayed (right).

area that contains varied landscape (Fig. 2). Although some part of this sink may be formed by a combination of geological and human factors, this outlier sink is excluded for further assessment so that we can focus on other sinks for classifying and comparing their attributes.

We also noted that a large portion of sinks are quite small (237 out of the 830 sinks are less than 1 m^2). Understanding that the sinks were extracted from 1 m DTMs, and the minimum data resolution for detecting a landscape object should be less than one-half the size of the feature (Jensen, 2005), we regard sinks smaller than 3 m^2 unreliable and possibly artifacts. Therefore, a total of 362 small sinks were removed and the remaining 468 sinks were retained for continued assessment. An initial examination of the sinks on aerial photos indicate some sinks appear to be man-made detention ponds in residential neighborhood areas (Fig. 2). This issue will be addressed later in our analysis.

Assessing Sinkhole Susceptibility based on Sinks Morphological Attributes

We first assessed sinkhole susceptibility relevant to sink area/size (Fig. 3A). As sinkholes develop and evolve, they are likely to expand in size and in depth until the underground crevices and voids are clogged and the overlying materials stop moving downward (Gouzie and Pendergrass, 2009; Parise, 2010; Gutierrez et al., 2014). Based on this sinkhole development process, smaller sinkholes seem to have more potential for continued growth and threatening human activities and properties, while large sinkholes may have evolved to a mature stage of development, and therefore, pose little risk to humans. Nevertheless, there is no direct relationship between sinkhole size and its potential for further development. In addition, we can never be certain what stage of development a sinkhole is at present. As a result, sinkhole susceptibility is assessed based on potential human exposure corresponding to the size of a sink. From a management point of view, larger sinks likely require more manual efforts for mitigation actions. For these reasons, higher susceptibility scores are assigned to sinks of larger size, which will be described in detail later.

We noticed that a few sinks in the south-east quadrangle of the study area have considerably jagged and elongated shapes (Fig. 2B). A close examination of current and historical aerial photos indicates that these irregularly-shaped sinks are man-made roadside swales and subdivision detention basins. To filter out these man-made sinks, we applied

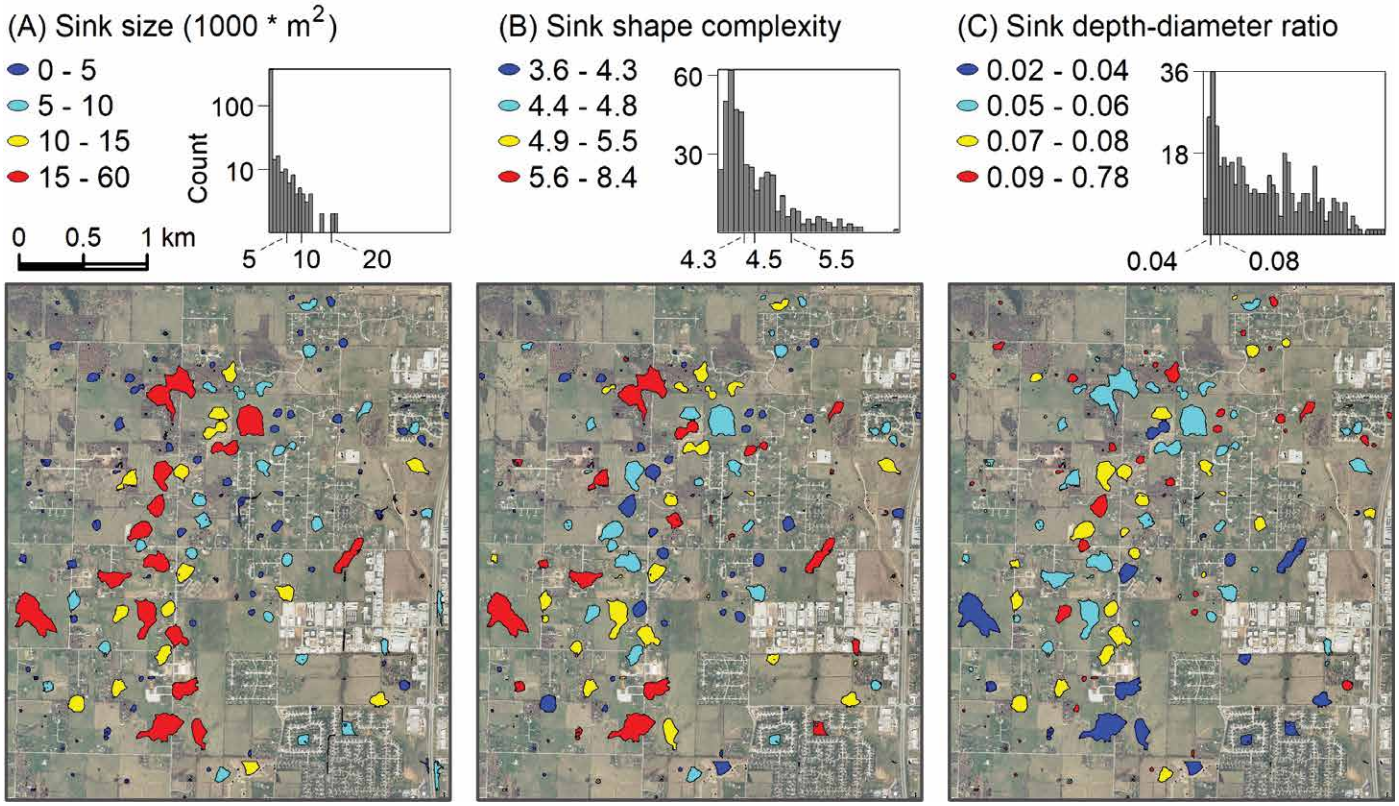

Figure 3. Ranking of sinks based on size (A), shape complexity (B), and depth to diameter ratio (C), with histograms showing the distributions.

a shape complexity index, calculated as the polygon perimeter divided by the square root of polygon area (Moser et al., 2002). A more complex shape will have a higher shape complexity index. Man-made sinks have a shape index larger than 7.4, therefore, a threshold of 7.4 is applied to exclude a total of 18 man-made sinks.

Some neighborhood detention ponds (e.g., sinks in the southwest and northeast corners of the study area) have relatively compact shapes. In contrast to jagged, elongated detention basins, these compact-shaped detention ponds may possibly have a geological origin but have been utilized for storm-water management purposes. For this reason, these compact-shaped detention ponds are retained for subsequent assessment. Mapping the remaining 450 sinks based on the shape complexity index (Fig. 3B), we noted that larger sinks tend to have more irregular shapes than smaller sinks. For sinkhole management purpose, sinks of more irregular shapes have boundaries harder to delineate in the field and would require more work for mitigation actions, e.g., putting up warning signs around the perimeter. For this reason, we consider sinks of more irregular shapes posing more risk to humans and would give them a higher sinkhole susceptibility score.

Most sinkholes are depressions with gentle slopes and smoother morphology formed by the sagging or suffosion process; and sinkholes with steep sides formed by the collapse process are relatively uncommon (Troester et al., 1984; Denizman, 2003; Caramanna et al., 2007; BGS, 2017). Sinkhole morphology is mainly determined by the mechanical strength of the surface materials in which they form. For example, sinkholes formed in alluvial sediment will have higher slopes and greater depths than sinkholes formed in mud (Al-Halbouni et al., 2017). Margiotta et al. (2012) indicated that cover collapse sinkholes are often steep with a diameter/depth ratio from 1.5 to 3. As the collapse process is considered relatively dangerous due to the rapid movement of surface materials, a higher susceptibility score is assigned to sinks with a larger depth to diameter ratio. For the study area, we noted that sinks with a higher depth/diameter ratio tend to be smaller in size and more compact in shape (Fig. 3C).

We further examined the topography of sink surfaces. Considering that sink surface is affected by the underlying geological structure, the terrain conditions may inform recent raveling activities that can facilitate surface water transport of soil down into cavities in underlying bedrock. As a result, sinks with a rougher surface are considered likely more geologically active than sinks with a smoother surface.

We created cross-sectional profiles for sinks to examine their terrain conditions (Fig. 4, left), and further derived a terrain ruggedness index to quantify the surface disturbing degree (Fig. 4, right). Specifically, the standard deviation of

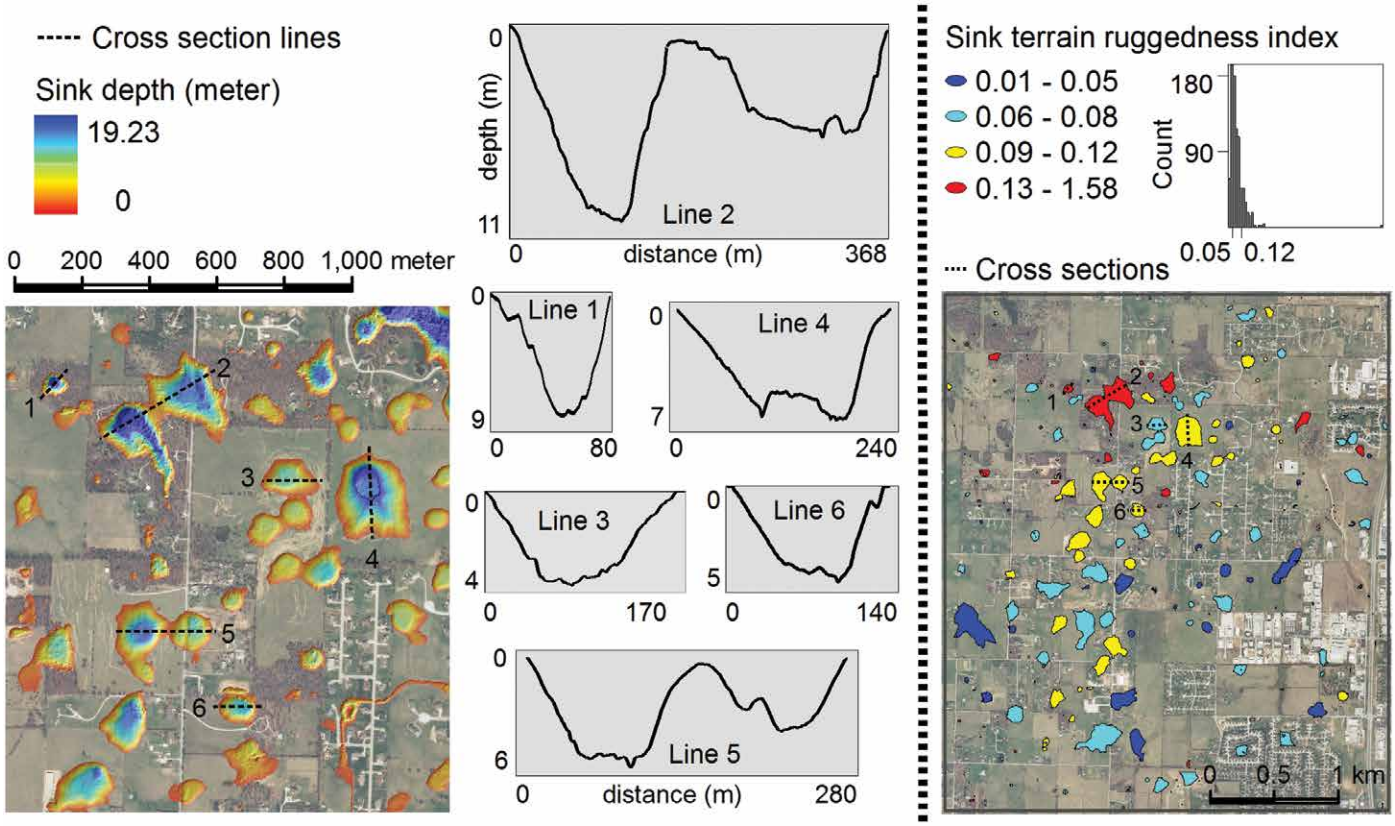

Figure 4. Cross-sectional profiles for six sinks (left), and ranking of sinks based on terrain ruggedness with histograms showing the distributions (right).

elevation in a 3×3 m moving window was first computed as the local terrain ruggedness index (Ascione et al., 2008). The average terrain ruggedness index within each sink polygon was then calculated as an attribute. Observe that sinks with a high ranking of terrain ruggedness index also have a relatively rugged profile (Fig. 4).

Some sinks (represented by 0.5 m depth isolines) appear to be congregations of two original sinks (Fig. 4). This phenomenon happens when sinks grow and expand throughout the years and eventually connect with neighboring sinks to form a large one. Sink coalescence would have some effects on the terrain ruggedness measure. Specifically, the connecting ridge area of two neighboring sinkholes are generally broader and less disturbed/rugged than the sloping area. As a result, when two neighboring sinks are connected, the local terrain is likely to become smoother. The new terrain ruggedness index for the congregated sink would be approximately an average of the two original ones.

Assessing Sinkhole Susceptibility based on Sinks Imagery Attributes

Many sinks in the study area are traversed by roads (Fig. 2). Since roads provide human accessibility, sinks close to roads would pose more sinkhole risk than sinks away from roads. Accordingly, we derived impervious surface percentages for sinks to indicate the human exposure level (Qiu and Wu, 2017). A raster layer of impervious surface was first generated through remote sensing imagery classification from the 0.6 m resolution aerial photos. The percentage of impervious surface within a 100-meter buffer of sink polygons was then calculated for each sink (Fig. 5A). Sinks with a higher impervious surface measure ratio will be given a higher susceptibility score.

Because sinks naturally accumulate water, there is often more vegetation growth around sinkholes than in surrounding areas (Handfelt and Attwooll, 1988; Sowers, 1996; Gutiérrez et al., 2008). And since vegetation stabilizes soil, sinkholes would be safer when there is denser vegetation nearby (Gutiérrez et al., 2008; Zhou and Beck, 2008). For example, because trees stabilize soil more effectively than grass does, sinks within woodlands pose less risk than those in grasslands. Also, grassland is more accessible to humans than woodland, which makes sinks located there potentially more unsafe to a greater number of passers-by. In the same way, sinks located on barren land are potentially more likely to cause the most problems.

Accordingly, we calculated the NDVI index in order to gauge vegetation growth conditions. The NDVI measures the chlorophyll pigment absorptions in the red band and the high reflectivity of plant materials in the near-infrared (NIR) band (ESRI, 2016). Such values were interpreted as shown in Table 2 (Weier and Herring, 2000).

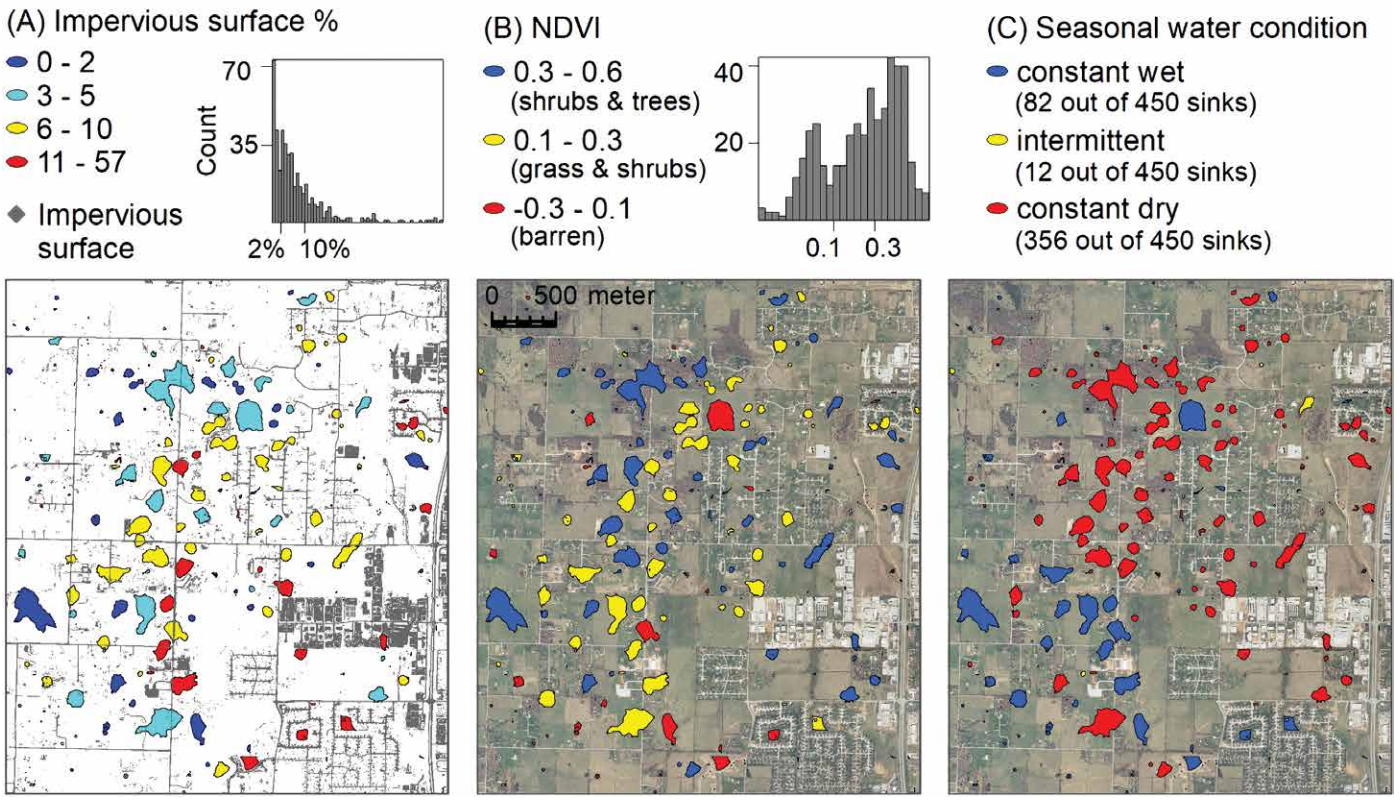

Figure 5. Ranking of sinks based on impervious surface percentage (A), NDVI (B), and seasonal water condition (C), with histograms showing the distributions.

Table 2. Interpretation of NDVI values.

Value	Interpretation
< 0.1	rock, sand, snow
0.2 – 0.3	shrubs, grassland
0.6 – 0.8	temperate and tropical rainforests

We derived a NDVI raster layer from the one-meter, 4-band, 2009 aerial photos. The average NDVI value within each sink polygon was then calculated as its attribute (Fig. 5B). Sinks having a lower NDVI are considered having higher sinkhole susceptibility.

Many sinks in the study area have impounded water that can be observed from aerial photos (Fig. 2). As water is a triggering mechanism for sinkhole incidence (Parise, 2010, 2015b; Kaufmann and Romanov, 2016), the surface water seasonal condition can inform potential sinkhole risk by showing whether the surface water can be easily flushed down into the bedrock or soil voids and how clogged the underground voids are (Qiu and Wu, 2017).

Three types of surface water conditions can be observed for sinks in our study area:

1. Sinks with perennially impounded water, which may be considered as a relatively inactive sinkhole with sinkhole throat clogged;
2. Sinks with seasonal surface water, which may indicate water slowly drains down sinkhole throats that are not completely clogged; and
3. Sinks that are constantly dry, which may indicate that the surface water can quickly drain out from the sinkhole throat.

A water-impounded sink may be a sagging or suffosion sinkhole that grows from top down, or a collapse sinkhole that grows from bottom up. In the latter case, surface water is temporarily retained due to an earlier collapse clogged the sinkhole throat. As the water-filled collapse sinkhole may continue to grow further, the growth becomes slower and the potential risk is reduced.

In this study, we focused on the water retaining mechanism for sagging/suffosion sinkholes for susceptibility assessment, since collapse sinkholes are relatively rare in the study area. Specifically, constantly dry sinks are considered posing the most potential sinkhole risk due to the constant transportation of water from surface to underground that expedites the dissolution process. In contrast, water-filled sinks have relatively inactive water flow and are considered posing less risk than (intermittently) dry sinks. From another point of view, the impounded surface water allows progressive geologic activities (e.g., rapid soil/rock movements), to be easier to detect, and thus, makes the water-filled sinks more manageable.

To derive the seasonal water condition for sinks, we classified the water cover class from both the 2008 winter aerial photo and the 2009 summer aerial photo. As winter is the dry season (an average rainfall of 196 mm) and summer is the wet season (an average rainfall 299 mm) in Nixa, Missouri, the water cover classes from the two seasons were compared, and sinks were categorized as either constantly dry, intermittently dry, or constantly wet (Fig. 5C).

Assessing Sinkhole Susceptibility based on Sinks Contextual Attributes

What type of land use a sink is located has implications in human exposure to potential sinkhole incidence. For example, commercial land use usually has more human activities than other land uses; therefore, sinks located on commercial land use are considered to pose higher potential sinkhole risk. In contrast, sinks on agricultural or manufacturing land use often have the least traffic and thus present the least risk to humans.

To assess sinkhole susceptibility based on land use, we used parcel data to infer land use information for sinks. Land parcels were categorized into four land use types, including commercial, agricultural/manufacturing, and two types of residential land use: rural and suburban (Fig. 6A). For the two residential land use, suburban residential is considered to have more human activities/traffic and, therefore sinks located on it would pose higher human threats. When a sink falls on more than one land use, the land use occupying more sink surface takes priority over others.

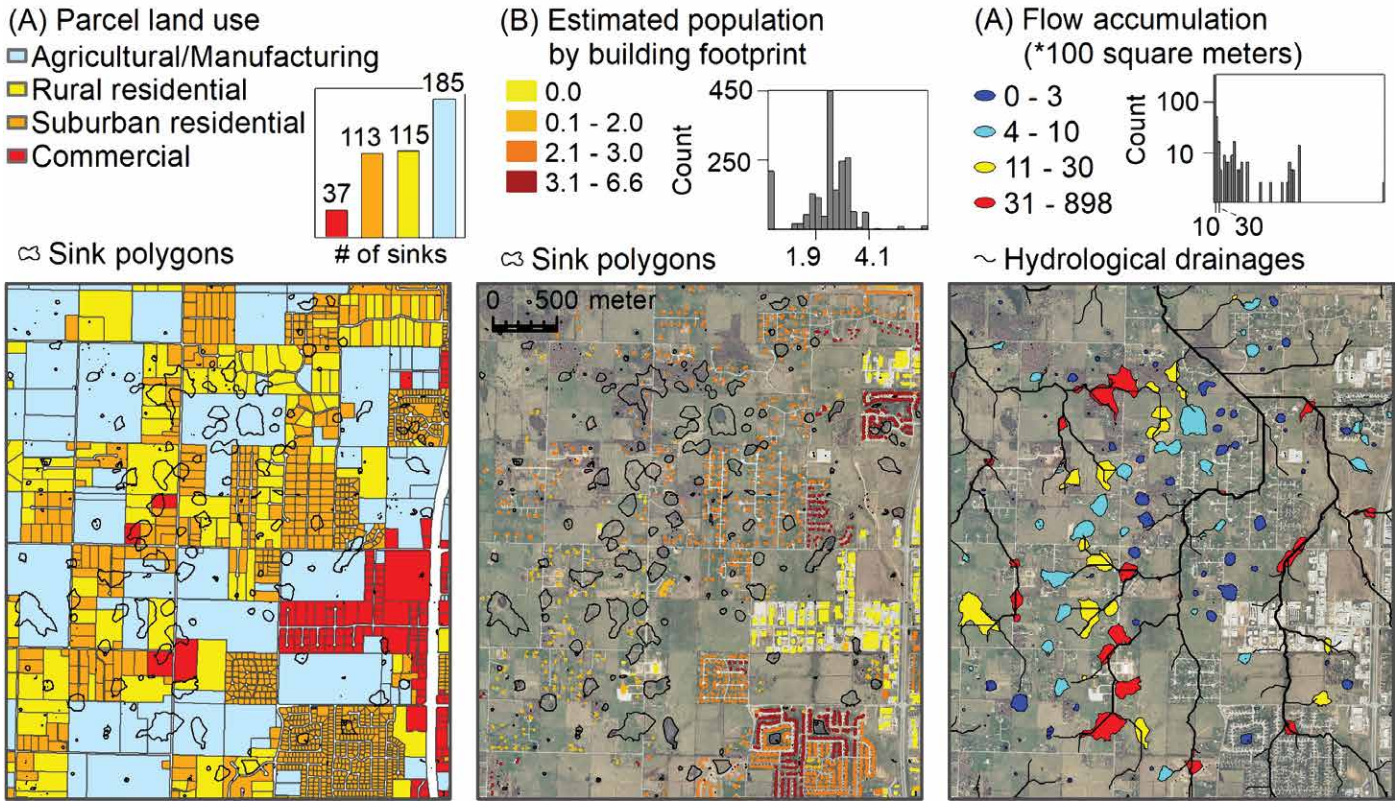

Figure 6. Four types of parcel land use with a chart showing the number of sinks in each land use (A), redistributed census block populations based on land use types and building footprints (B), and ranking of sinks based on hydrological flow accumulation (C), with histograms showing the distributions.

In addition to land use types, population density for the nearby area of sinks has implications in human exposure to potential sinkhole incidence. Therefore, sinks with higher population density are considered to pose more sinkhole threats to humans than sinks with lower population density.

We calculated the population density within a 400-meter buffer of sink polygon to infer neighborhood population density for sinks. The reason a 400-meter (0.25 miles, about 5-minute walk) buffer is used to calculate population density is that this distance is widely used as an acceptable walking distance in many studies (Atash, 1994; Krizek, 2003; McCormack et al., 2008). The calculation was performed in the following three steps:

1. Using the dasymetric mapping approach to redistribute block-level population to residential buildings, based on building footprints and land use data with predefined population ratios for different land uses (Fig. 6B).
2. Calculating the total population within a 400-meter buffer of each sink polygon by summing the building populations within the buffer.
3. Calculating population density for the buffered area and assigning the measure to respective sinks.

We further examined the hydrological flow for sinks to assess sinkhole susceptibility. Since sinks with larger accumulated flows would have more water supply to facilitate the progressive geological process, they are considered to have higher risk than sinks with smaller accumulated flows.

To calculate the accumulated flow for sinks, we first filled the hydrological depressions on a 10-m DTM resampled from the 1 m DTM to generate a smooth surface so that the subsequent flow direction calculation will be more accurate. A flow direction raster was then derived with the cells values representing one of the eight possible flow directions from the center cell to the neighboring cell with the steepest descent. A flow accumulation raster was further derived with the cell values representing the total number of upslope cells flowing into each downslope cell. Lastly, the maximum accumulated flow value within each sink polygon was calculated, which can be seen as the water catchment areas for the lowest point of the sink.

We noted that sinks situated on hydrological drainages naturally have high flow accumulations (Fig. 6C). Sinks located in the general downstream areas (the north) do not necessarily have larger flow accumulation than sinks located in upstream areas (the south), because the most important factor for determining a sink's flow accumulation is whether the sinks is situated within a drainage valley, which depends on local topography around the sink.

Another contextual attribute that this study incorporated for sinkhole susceptibility assessment is the density of neighboring sinks, since locations with a high density of sinks are prone to sinkhole incidence (Galve et al., 2009c). We calculated the density of neighboring sinks within a 400-m buffer of the sink of interest to indicate the degree of sinkhole susceptibility (Fig. 7A). There appears to be high density of sinks in the north-central area (shown as red).

Existing sinkhole records may provide insight to potential sinkhole risk. Using the sinkhole database compiled by the Division of Geology and Land Survey at Missouri Department of Natural Resources, we calculated a sinkhole-potential surface (Fig. 7B) based on the weighted density of sinkhole records. The weights are based on the reliability of the sinkhole records, considering those created from data sources of higher resolutions and/or have been verified by field visits more reliable and given higher weights. A sinkhole-potential measure was then calculated based on combined sinkhole-potential values within a 400-meter buffer of the sink.

Understanding that groundwater withdraw contributes to sinkhole risk, we calculated a well yield (gallons per minute) surface using the well yield (gallons per minute) information in the wells data (Fig. 7C). A sinkhole risk measure was then derived based on the total well yield within a 400-meter buffer of the sink.

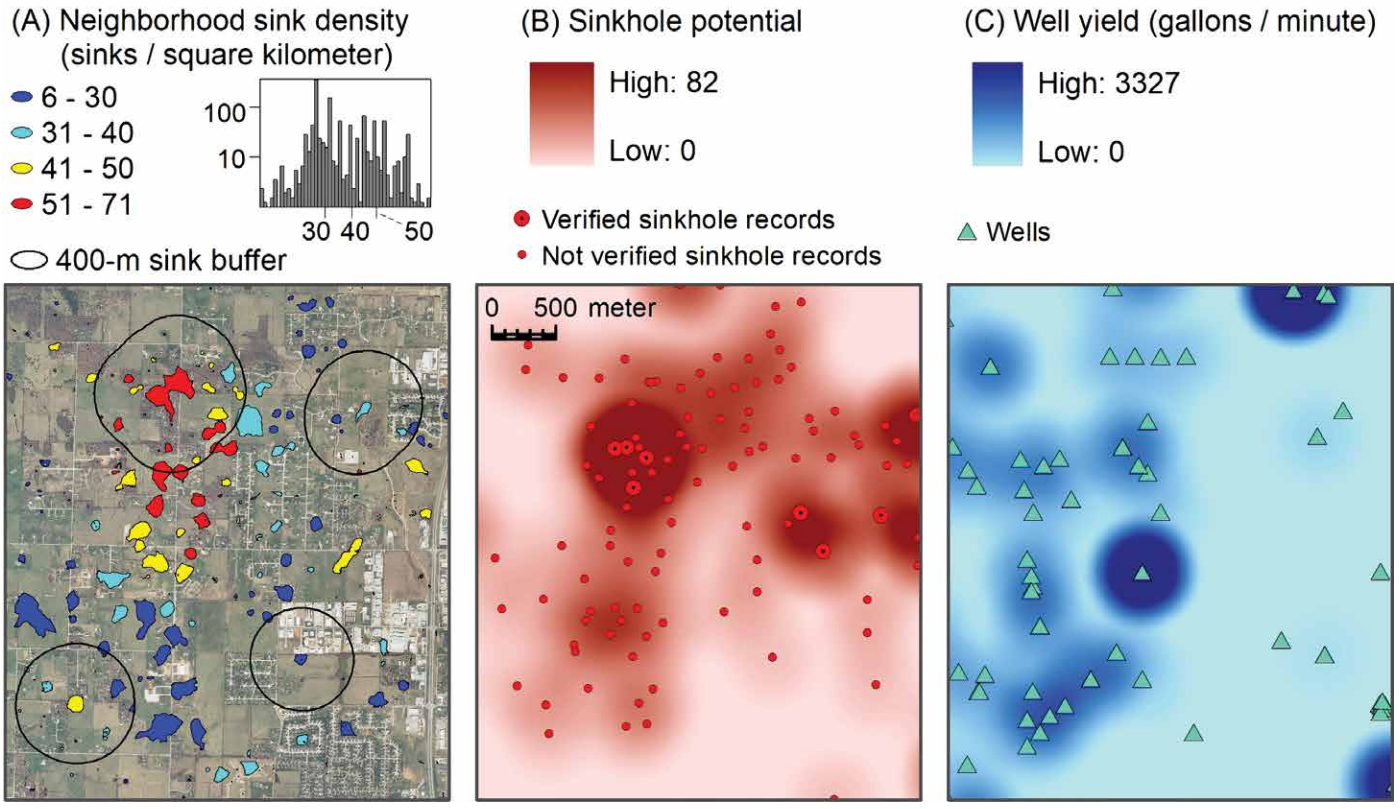

Figure 7. Ranking of sinks based on 400-m-buffer sink density (A), interpolated sinkhole potential surface based on existing sinkhole records (B), and interpolated well-yield surface from wells data (C).

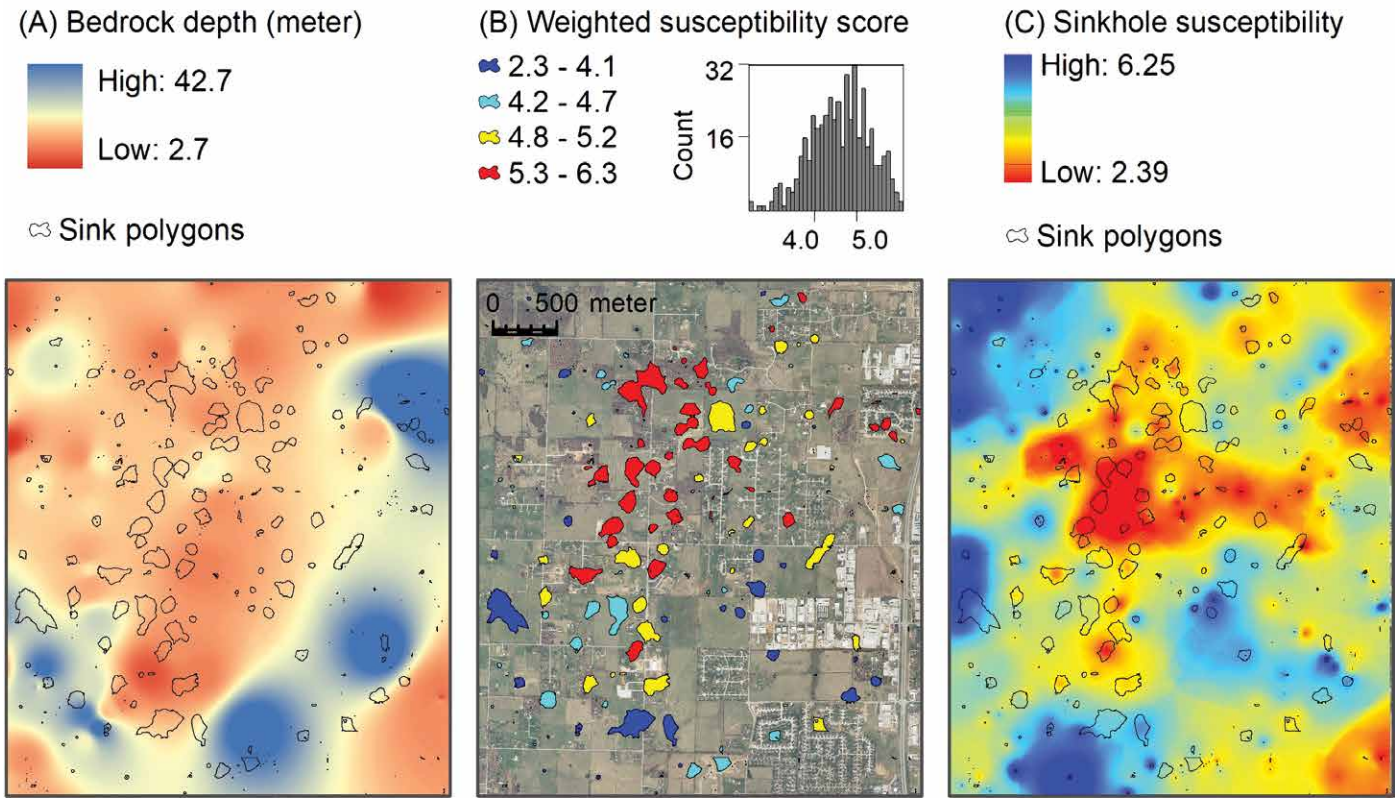

Figure 8. Interpolated bedrock depth surface based on wells data (A), ranking of sinks based on the weighted susceptibility score from all attributes (B), and an interpolated surface of sinkhole susceptibility (C).

Considering that the depth to bedrock has an effect on the probability of sinkhole collapse, we estimated the bedrock depth (Fig. 8A) based on descriptions and depth information of formations in the wells data. A bedrock depth surface was then interpolated from the bedrock depth data. Further, a sinkhole risk measure was calculated based on the maximum bedrock depth within a 100-meter buffer of the sink.

Combining all Sinks Attributes for Sinkhole Susceptibility Assessment

Lastly, all sink attributes were combined for susceptibility assessment. Each ratio variable of sink attributes was classified into nine ranges with each range of 50 sink records. Classifying sink attributes by broad range allows minimizing the inherent uncertainty of sink attributes in denoting sinkhole susceptibility. Sinks in each range were assigned a corresponding susceptibility score from 1 to 9, with 9 being the most potentially dangerous or of highest priority for sinkhole management (Table 3).

For categorical variables, including the seasonal water condition and land use types, a score between 2 and 8 was assigned based on the risk implication of the attribute. We did not use the score range of 1 to 9 as others have done in order to minimize the uncertainty and potential error in quantifying categorical variables. Specifically, using a smaller interval with a larger minimum and a smaller maximum will make categorical variables less influential to the overall susceptibility scores combined from all variables.

To identify high-priority sinkholes for sinkhole prevention and mitigation efforts, we combined susceptibility scores from each attribute through a weighting approach. In principle, the weight should be determined by how the attribute denotes the probability of sinkhole-causing property damage and human injury. Practically, the weight is decided based on the analysis objectives as well as the assessor's opinions of what are considered important. In this study, higher weights are assigned to the attributes that we considered as important risk indicators, while lower weights are given to attributes that we considered less reliable due to spatial data precision (Table 4). Specifically, the following five criteria are utilized in assigning weights:

1. Unless meeting the following criteria, all attributes are taken as moderate risk indicators and are assigned a neutral weight of 1;
2. If the attribute is commonly used as sinkhole susceptibility indicator with solid theoretical support, it is given a weight of 2;
3. The attribute of land use is given a weight of 4, considering that sinkhole management priority is usually given to the developed/developing urban areas, which are mainly commercial and residential land use.

Table 3. Classification of sink attributes and the value ranges in each class.

Attributes	Classes (Susceptibility Scores)	Value Ranges
Size (square meters)	9	5342 – 59648
	8	858 – 5341
	7	177 – 857
	6	45 – 176
	5	22 – 44
	4	13 – 21
	3	8 – 12
	2	6 – 7
	1	3 – 5
Shape complexity	9	5.73 – 8.42
	8	5.07 – 5.72
	7	4.77 – 5.06
	6	4.44 – 4.76
	5	4.25 – 4.43
	4	4.10 – 4.24
	3	3.98 – 4.09
	2	3.86 – 3.97
	1	3.64 – 3.85
Depth to diameter ratio	9	0.53 – 0.78
	8	0.44 – 0.52
	7	0.37 – 0.43
	6	0.28 – 0.36
	5	0.20 – 0.27
	4	0.14 – 0.19
	3	0.10 – 0.13
	2	0.07 – 0.09
	1	0.02 – 0.06
Terrain ruggedness	9	0.167 – 1.585
	8	0.125 – 0.166
	7	0.105 – 0.124
	6	0.084 – 0.104
	5	0.072 – 0.083
	4	0.060 – 0.071
	3	0.049 – 0.059
	2	0.037 – 0.048
	1	0.008 – 0.036
Impervious surface (%)	9	16.5 – 56.9
	8	11.6 – 16.4
	7	8.5 – 11.5
	6	6.3 – 8.4
	5	4.7 – 6.2
	4	3.4 – 4.6
	3	1.7 – 3.3
	2	0.6 – 1.6
	1	0.0 – 0.5
NDVI	9	−0.30 – −0.04
	8	−0.03 – 0.06
	7	0.07 – 0.19
	6	0.20 – 0.27
	5	0.28 – 0.33
	4	0.34 – 0.39
	3	0.40 – 0.43
	2	0.44 – 0.48
	1	0.49 – 0.61
Seasonal water condition	7	Constant dry
	5	Intermittent
	3	Constant wet

4. The attribute of seasonal water condition is given a weight of 0.5, considering that the susceptibility score for a corresponding category is relatively generalized and may be unreliable;
5. The attribute of vegetation growth index is given a weight of 0.5, considering that vegetation would not have much stabilizing effects when surficial materials above bedrock are thick, and a sinkhole collapse will occur at some time regardless of the vegetation cover.

Using the defined weight for each sink attribute, we calculated the overall weighted susceptibility scores for sinks and ranked them by four ranges with similar number of sinks in each range (Fig. 8B). As the final, combined susceptibility scores are interpreted in broad ranges, it is reasonable to mark sinks in higher ranks with higher priority for further investigation or prevention management than sinks in lower ranks. It appears that high-susceptibility sinks cluster in the central part of the study area. Understanding that many small sinks cannot be observed on maps, we interpolated a sinkhole susceptibility surface from the susceptibility scores based on the centroids of sink polygons (Fig. 8C). The interpolated susceptibility surface highlights the red risk zones of high sinkhole susceptibility. Those red areas are considered having high priority for further field-based geophysical investigation, as well as for conducting sinkhole prevention and mitigation activities. Some sinkhole management strategies may include:

- Minimizing new land development and construction activities in the area;
- Regularly monitoring the ground conditions for sinks in the area;
- Educating/notifying land owners of the potential sinkholes in their properties.

Discussion

This study presents a computerized approach for sinkhole susceptibility assessment based on sink attributes that can be efficiently derived from digital data of elevation, aerial photos, parcel land use/zoning, and census demographics. The advantage of this approach is that emergency managers and planners can use it to quickly identify high-priority sinkholes. The disadvantage of the approach is that it could not confirm the existence of sinkholes, because the assessment is based on sinkhole risk indicators and human vulnerability considerations. The actual geological activities underground can only be verified through geophysical investigation using ground penetrating radar (GPR). Nevertheless, from another point of view, results from this

Table 3. (Continued).

Attributes	Classes (Susceptibility Scores)	Value Ranges
Land use	8	Commercial
	6	Suburban residential
	4	Rural residential
	2	Agricultural/ Manufacturing
Population density (persons/square kilometer)	9	451 – 1660
	8	298 – 450
	7	222 – 297
	6	161 – 221
	5	140 – 160
	4	116 – 139
	3	78 – 115
	2	49 – 77
	1	0 – 48
Hydrological flow accumulation (square meters)	9	10977 – 89841
	8	1245 – 10976
	7	468 – 1244
	6	226 – 467
	5	89 – 225
	4	29 – 88
	3	11 – 28
	2	5 – 10
	1	0 – 4
Sink density (sinks/square kilometer)	9	62 – 71
	8	54 – 61
	7	49 – 53
	6	44 – 48
	5	37 – 43
	4	32 – 36
	3	28 – 31
	2	23 – 27
	1	6 – 22
Sinkhole potential	9	21 – 33
	8	12 – 20
	7	9 – 11
	6	8
	5	6 – 7
	4	5
	3	4
	2	2 – 3
	1	1
	0	0
Well yield	9	581 – 960
	8	376 – 580
	7	251 – 375
	6	231 – 250
	5	181 – 230
	4	141 – 180
	3	98 – 140
	2	36 – 97
	1	1 – 35
	0	0
Bedrock depth	9	6.6 – 10.4
	8	10.5 – 12.0
	7	12.1 – 12.7
	6	12.8 – 14.1
	5	14.2 – 16.0
	4	16.1 – 18.3
	3	18.4 – 21.0
	2	21.1 – 29.3
	1	29.4 – 42.7

computerized approach can be used as an initial framework to prioritize limited resources for sinkhole investigation and mitigation (Zumpano et al., 2019).

This study assessed sinkhole susceptibility based on fourteen sink attributes. The advantage of the proposed attributes is that many of them are intended to be suitable for a hilly, vegetated karst terrain and are, therefore, applicable to areas of similar landscape. Furthermore, the proposed attributes can be conveniently derived from common GIS and imagery data without time-consuming data collection in the field.

There are two potential disadvantages of using the proposed sink attributes for susceptibility assessment. The first is the inherent errors in data source and in computational analysis. Particularly, the resolutions of the DTMs and aerial photos, and the rigor of the procedures used to derive the attributes affect the accuracy of all the attributes. The second disadvantage of using these attributes for susceptibility assessment is the inherent uncertainty in the relevancy of the attributes denoting sinkhole risk, since the relationships between attribute and sinkhole incidence are hard to quantitatively define.

As this study combined all criteria for sinkhole susceptibility assessment by mathematically adding the susceptibility scores, it is worth noting that different sinkhole variables may not be comparable and, therefore, their respective susceptibility (scores) may not be accumulated directly. Nevertheless, multiple-criteria decision analysis (MCDA) requests certain conclusions be drawn to aid decision making. Accordingly, we combined susceptibility scores and classified the combined scores in four broad ranges to minimize the inherent errors while allowing for ranking and prioritizing sinkholes.

As the attribute weights are assigned based on our perception and understanding of what attributes are considered important and/or reliable, other studies using the same variables may adjust the weights based on their analysis needs/objectives. Furthermore, future research may model how the attributes collectively relate to quantified sinkhole incidence (e.g., using linear regression analysis). Through the calibration of model parameters, the attribute weights for combing susceptibility scores may be defined more objectively and with a higher precision.

Specific rock materials play a significant role in how sinkholes are formed as well as the probability of sinkhole incidence. For example, in our karst study area dominated by carbonate limestone, if the rock materials contain impure

Table 4. The weights assigned to each sink attribute for combining them for sinkhole susceptibility assessment.

Attributes	Weights	Considerations for Assigning Weights
• Size	1	• Reasonable susceptibility indicator
• Shape complexity	1	• Reasonable susceptibility indicator
• Depth to diameter ratio	2	• Solid theoretical support
• Terrain ruggedness	1	• Reasonable susceptibility indicator
• Impervious surface %	1	• Reasonable susceptibility indicator
• NDVI	0.5	• Vegetation matters little when soil is thick
• Seasonal water condition	0.5	• Categorical variable with inherent uncertainty
• Land use	4	• Strong policy implications
• Population density	2	• Solid theoretical support
• Hydrological flow accumulation	2	• Solid theoretical support
• Sink density	2	• Solid theoretical support
• Sinkhole potential	2	• Solid theoretical support
• Well yield	1	• Reasonable susceptibility indicator
• Bedrock depth	1	• Reasonable susceptibility indicator

carbonate rocks or interbedded insoluble lithology in limestone sequences, the dissolution process would operate at relatively slow rates, which allows sagging and suffusion sinkholes to be more common than otherwise. In contrast, if the carbonate rocks contain pure minerals of calcite and dolomite, the rocks will be considerably soluble to allow voids and cracks to form; and collapse sinkholes will have a higher probability to occur than otherwise.

Past researchers have shown that sinkholes are likely to occur along geological faults (Florea 2005*;* Closson and Karaki 2009). For the Ozark karst region, the overall direction of faults is from northwest to southeast. Nevertheless, we did not consider the location of fault as a criterion for susceptibility assessment because our study area is relatively small without major faults. For studies covering large area with many faults, the location and direction of existing faults may be regarded as an important factor for assessing sinkhole susceptibility.

There are many man-made sinks in our study area and we only filter out those with considerably elongated or jagged shapes through a shape complexity index. Understand that some apparent man-made sinks may be initially created by natural, geological mechanism but later reshaped by human activities. For example, in developed urban areas, humans may build detention ponds and roadside swales upon existing land depressions. In undeveloped rural areas, naturally formed sinks or lakes may be disturbed by agriculture or farm activities.

The geologic process and formation of sinkholes may be induced or expedited by human activities, such as mining, deforestation, over irrigation, groundwater pumping, broken sewer lines or water mains, inappropriately buried organic debris, and improperly compacted construction soil after excavation (Kochanov, 1999; Gutiérrez et al. 2008*,* 2014). Due to this complex human-landscape interaction, detailed geophysical investigation is needed to verify whether the appeared man-made sinks are solely created by human activities or have geological origins with potential sinkhole hazard.

When assessing sinkhole susceptibility based on impervious surface percentage, we classified the impervious surface land cover from digital aerial photos using the traditional, most commonly used, maximum likelihood classification algorithm. A close examination of the classified results on aerial photos indicates that some barren lands were misclassified as impervious surface, while some road surfaces were not classified as they should. More advanced classification algorithms such as neural network and decision tree, or more sophisticated object-based image software such as e-Cognition or Feature Analyst, may help improve the classification results. Nevertheless, more advanced image classification approaches often have more algorithm/software parameters for users to consider. The determination of optimal parameters often requires a calibration process consisting of trial-and-error experiments that may be time consuming (Wu et al., 2009).

To derive the seasonal water condition for sinks, we used a straightforward change detection method in remote sensing in which a pair of winter and summer aerial photos are classified individually and then compared. Future sinkhole analysis may test other change detection techniques that may be more efficient and/or accurate. For example, algebra-based approaches like image differencing, image regression, and change vector analysis may streamline the analysis, though initial radiometric normalization between the two photos would be required.

This study examines the surface water conditions of sinks in order to estimate potential sinkhole risk. The advantage of this approach is that it is convenient to detect the existence of surface water from aerial photos. It is worth noting that groundwater supply also plays a role in the formation and stability of sinkholes. Specifically, the lowering of the groundwater table during the dry season or from excessive groundwater pumping may facilitate the formation of cover-collapse sinkholes due to the effect of the drawdown of the piezometric surface in the karst aquifer (Tharp, 2002).

Conclusions

This study develops robust methodology for computerized sinkhole susceptibility assessment based on common GIS and imagery data. The methodology of extracting sinks and assessing potential sinkhole risk by sink attributes can be efficiently applied to other karst areas, particularly areas in a hilly and vegetated landscape.

The selected sinkhole attributes for susceptibility assessment can be conveniently derived with available GIS tools, specifically tools in the widely-accessible ArcGIS software. For the fourteen sinkhole attributes used in this study, three of their uses are deemed innovative, considering that they have not been used in past studies to assess sinkhole susceptibility. These three sinkhole attributes include:

- The terrain ruggedness index and the maximum hydrological flow accumulation, which can be derived from bare-ground DTMs;
- The Normalized Difference Vegetation Index (NDVI), which can be derived from 4-band digital photos.

The proposed computerized susceptibility ranking approach can be effectively used as an initial sinkhole analysis to determine where more detailed site investigation and data collection are warranted. The findings of the high-susceptibility sinkholes as well as the corresponding 'risk zone' in the Nixa karst area can be used to support decision making in prioritizing limited emergency planning and management resources. For example, field-based investigation using GPR can be further conducted for those high-priority sinks to examine their underground geophysical structures and the probability of further sinkhole activities. If high probability of future sinkhole incidents is confirmed, the landowner should build a barrier at a safe distance to prevent access to the sinkhole. Further, if the confirmed high-risk sinkholes are located in a populated neighborhood, it may be necessary to properly fill and physically stabilize the void to mediate the potential of future collapse.

References

Al-Halbouni, D., Holohan, E.P., Saberi, L., Alrshdan, H., Sawarieh, A., Closson, D., Walter, T.R., and Dahm, T., 2017, Sinkholes, subsidence and subrosion on the eastern shore of the Dead Sea as revealed by a close-range photogrammetric survey: Geomorphology, v. 285, p. 305−324. .https://doi.org/10.1016/j.geomorph.2017.02.006

Angel, J.C., Nelson, D.O., and Panno, S.V., 2004, Comparison of a new GIS-based technique and a manual method for determining sinkhole density: An example from Illinois' sinkhole plain: Journal of Cave and Karst Studies, v. 66, no. 1, p. 9−17.

Aplin, P., Atkinson, P.M., and Curran, P.J., 1999, Fine spatial resolution simulated satellite sensor imagery for land cover mapping in the United Kingdom: Remote Sensing of Environment, v. 68, no. 3, p. 206−216. https://doi.org/10.1016/S0034-4257(98)00112-6.

Applegate, P., 2003, Detection of sinkholes developed on shaley Ordovician limestones, Hamilton County, Ohio, using digital topographic data: Dependence of topographic expression of sinkholes on scale, contour interval, and slope: Journal of cave and karst studies, v. 65, no. 2, p. 126−129.

Ascione, A., Cinque, A., Miccadei, E., Villani, F., and Berti, C., 2008, The Plio-Quaternary uplift of the Apennine chain: New data from the analysis of topography and river valleys in Central Italy: Geomorphology, v. 102, no. 1, p. 105−118. https://doi.org/10.1016/j.geomorph.2007.07.022.

Atash, F., 1994, Redesigning suburbia for walking and transit: Emerging concepts: Journal of Urban Planning and Development, v. 120, no. 1, p. 48−57. https://doi.org/10.1061/(ASCE)0733-9488(1994)120:1(48).

Atzori, S., Baer, G., Antonioli, A., and Salvi, S., 2015, InSAR-based modeling and analysis of sinkholes along the Dead Sea coastline: Geophysical Research Letters, v. 42, no. 20, p. 8383−8390. https://doi.org/10.1002/2015GL066053.

Barredo, J., Benavides, A., Hervas, J., and van Westen, C.J., 2000, Comparing heuristic landslide hazard assessment techniques using GIS in the Tirajana basin, Gran Canaria Island, Spain: International Journal of Applied Earth Observation and Geoinformation, v. 2, no. 1, p. 9–23. https://doi.org/10.1016/S0303-2434(00)85022-9.

Basso, A., Bruno, E., Parise, M., and Pepe, M., 2013, Morphometric analysis of sinkholes in a karst coastal area of southern Apulia (Italy): Environmental earth sciences, v. 70, no. 6, p. 2545−2559. https://doi.org/10.1007/s12665-013-2297-z.

Brinkmann, R., Parise, M., and Dye, D., 2008, Sinkhole distribution in a rapidly developing urban environment: Hillsborough County, Tampa Bay area, Florida: Engineering Geology, v. 99, no. 3−4, p. 169−184. https://doi.org/10.1016/j.enggeo.2007.11.020.

BGS (British Geological Survey), 2017, Dolines and sinkholes, http://www.bgs.ac.uk/mendips/caveskarst/Karst_3.htm [accessed August 18, 2019].

Bullock, P.J., and Dillman, A., 2003, Sinkhole detection in Florida Using GPR and CPT, http://citeseerx.ist.psu.edu/viewdoc/download?-doi=10.1.1.540.5058&rep=rep1&type=pdf [accessed August 18, 2019].

Castellanos Abella, E.A., and Van Westen, C.J., 2007, Generation of a landslide risk index map for Cuba using spatial multi-criteria evaluation: Landslides, v. 4, no. 4, p. 311−325. https://doi.org/10.1007/s10346-007-0087-y.

Castellanos Abella, E.A., and Van Westen, C.J., 2008, Qualitative landslide susceptibility assessment by multicriteria analysis: a case study from San Antonio del Sur, Guantánamo, Cuba: Geomorphology, v. 94, no. 3−4, p. 453−466. https://doi.org/10.1016/j.geomorph.2006.10.038.

Chalkias, C., Ferentinou, M., and Polykretis, C., 2014, GIS supported landslide susceptibility modeling at regional scale: An expert-based fuzzy weighting method: ISPRS International Journal of Geo-Information, v. 3, no. 2, p. 523−539. https://doi.org/10.3390/ijgi3020523.

Chalkias, C., Polykretis, C., Ferentinou, M., and Karymbalis, E., 2016, Integrating expert knowledge with statistical analysis for landslide susceptibility assessment at regional scale: Geosciences, v. 6, no. 1, p. 14. https://doi.org/10.3390/geosciences6010014.

Ciotoli, G., Di Loreto, E., Finoia, M.G., Liperi, L., Meloni, F., Nisio, S., and Sericola, A., 2016, Sinkhole susceptibility, Lazio Region, central Italy: Journal of Maps, v. 12, no. 2, p. 287−294. https://doi.org/10.1080/17445647.2015.1014939.

Closson, D., and Karaki, N.A., 2009, Salt karst and tectonics: Sinkholes development along tension cracks between parallel strike-slip faults, Dead Sea, Jordan: Earth Surface Processes and Landforms, v. 34, no. 10, p. 1408−1421. https://doi.org/10.1002/esp.1829.

Dai, F.C., Lee, C.F., and Ngai, Y.Y., 2002, Landslide risk assessment and management: an overview: Engineering Geology, v. 64, no. 1, p. 65–87. https://doi.org/10.1016/S0013-7952(01)00093-X.

De León, V., and Carlos, J., 2006, Vulnerability: a conceptional and methodological review, http://collections.unu.edu/eserv/unu:1871/pdf3904.

pdf [accessed August 18, 2019].
Del Prete, S., Iovine, G., Parise, M., and Santo, A., 2010, Origin and distribution of different types of sinkholes in the plain areas of Southern Italy: Geodinamica Acta, v. 23, no. 1−3, p. 113−127. https://doi.org/10.3166/ga.23.113-127.
Denizman, C.A.N., 2003, Morphometric and spatial distribution parameters of karstic depressions, Lower Suwannee River Basin, Florida: Journal of Cave and Karst Studies, v. 65, no. 1, p. 29−35.
Doctor, D.H., and Young, J.A., 2013, An evaluation of automated GIS tools for delineating karst sinkholes and closed depressions from 1-meter LIDAR-derived digital elevation data, https://scholarcommons.usf.edu/cgi/viewcontent.cgi?article=1156&context=sinkhole_2013 [accessed August 18, 2019]. https://doi.org/10.5038/9780979542275.1156.
ESRI, 2016, NDVI Function, http://desktop.arcgis.com/en/arcmap/10.4/manage-data/raster-and-images/ndvi-function.htm [accessed August 18, 2019].
Feizizadeh, B., and Blaschke, T., 2014, An uncertainty and sensitivity analysis approach for GIS-based multicriteria landslide susceptibility mapping: International Journal of Geographical Information Science, v. 28, no. 3, p. 610−638. https://doi.org/10.1080/13658816.2013.869821.
Festa, V., Fiore, A., Parise, M., and Siniscalchi, A., 2012, Sinkhole evolution in the Apulian karst of southern Italy: a case study, with some considerations on sinkhole hazards: Journal of Cave and Karst Studies, v. 74, no. 2, p. 137−147. https://doi.org/10.4311/2011JCKS0211.
Florea, Lee J. 2005, Using State-wide GIS data to identify the coincidence between sinkholes and geologic structure. Journal of Cave and Karst Studies, v. 67, no. 2, p. 120−124
Galve, J.P., Bonachea, J., Remondo, J., Gutiérrez, F., Guerrero, J., Lucha, P., Cendrero, A., Gutiérrez, M., and Sánchez, J.A., 2008, Development and validation of sinkhole susceptibility models in mantled karst settings: A case study from the Ebro valley evaporite karst (NE Spain): Engineering Geology, v. 99, no. 3−4, p. 185−197. https://doi.org/10.1016/j.enggeo.2007.11.011.
Galve, J.P., Gutiérrez, F., Lucha, P., Guerrero, J., Bonachea, J., Remondo, J., and Cendrero, A., 2009a, Probabilistic sinkhole modelling for hazard assessment: Earth Surface Processes and Landforms, v. 34, no. 3, p. 437−452. https://doi.org/10.1002/esp.1753.
Galve, J.P., Gutiérrez, F., Cendrero, A., Remondo, J., Bonachea, J., Guerrero, J., and Lucha, P., 2009b, Predicting sinkholes by means of probabilistic models: Quarterly Journal of Engineering Geology and Hydrogeology, v. 42, no. 2, p. 139−144. https://doi.org/10.1144/1470-9236/08-039.
Galve, J.P., Gutiérrez, F., Remondo, J., Bonachea, J., Lucha, P., and Cendrero, A., 2009c, Evaluating and comparing methods of sinkhole susceptibility mapping in the Ebro Valley evaporite karst (NE Spain): Geomorphology, v. 111, no. 3−4, p. 160−172. https://doi.org/10.1016/j.geomorph.2009.04.017.
Geneletti, D., and Gorte, B.G.H., 2003, A method for object-oriented land cover classification combining Landsat TM data and aerial photographs: International Journal of Remote Sensing, v. 24, no. 6, p. 1273−1286. https://doi.org/10.1080/01431160210144499.
Gouzie, D., and Pendergrass, G., 2009, Investigation and remediation of the 2006 Nixa, Missouri, collapse sinkhole, Environmental & Engineering Geoscience, v. 15, no. 1, p. 13−27. https://doi.org/10.2113/gseegeosci.15.1.13.
Gutierrez, F., Cooper, A.H., and Johnson, K.S., 2008, Identification, prediction, and mitigation of sinkhole hazards in evaporite karst areas: Environmental Geology, v. 53, no. 5, p. 1007−1022. https://doi.org/10.1007/s00254-007-0728-4.
Gutiérrez, F., Parise, M., De Waele, J., and Jourde, H., 2014, A review on natural and human-induced geohazards and impacts in karst: Earth-Science Reviews, v. 138, p. 61−88. https://doi.org/10.1016/j.earscirev.2014.08.002.
Handfelt, L.D., and Attwooll, W.J., 1988, Exploration of karst conditions in central Florida, *in* Sitar, N., ed., Geotechnical Aspects of Karst Terrains: Exploration, Foundation Design and Performance, and Remedial Measures: ASCE, p. 40−52.
Intrieri, E., Gigli, G., Nocentini, M., Lombardi, L., Mugnai, F., Fidolini, F., and Casagli, N., 2015, Sinkhole monitoring and early warning: An experimental and successful GB-InSAR application: Geomorphology, v. 241, p. 304−314. https://doi.org/10.1016/j.geomorph.2015.04.018.
Jensen, J.R., 2005, Introductory digital image processing: A remote sensing perspective, Upper Saddle River, N.J.: Prentice Hall.
Kaufmann, J.E., 2007, Catastrophic Sinkhole Collapse in Missouri, http://pubs.usgs.gov/fs/2007/3060 [accessed August 18, 2019].
Kaufmann, G., 2014, Geophysical mapping of solution and collapse sinkholes: Journal of Applied Geophysics, v. 111, p. 271−288. https://doi.org/10.1016/j.jappgeo.2014.10.011.
Kaufmann, G., and Romanov, D., 2016, Structure and evolution of collapse sinkholes: Combined interpretation from physico-chemical modelling and geophysical field work: Journal of Hydrology, v. 540, p. 688−698. https://doi.org/10.1016/j.jhydrol.2016.06.050.
Kochanov, W.E., 1999, Sinkholes in Pennsylvania: Pennsylvania Geological Survey, 4th ser., Educational Series, v. 11, p. 33.
Komac, M., 2006, A landslide susceptibility model using the analytical hierarchy process method and multivariate statistics in perialpine Slovenia: Geomorphology, v. 74, no. 1–4, p. 17–28. https://doi.org/10.1016/j.geomorph.2005.07.005.
Krawczyk, C.M., Polom, U., Trabs, S., and Dahm, T., 2012, Sinkholes in the city of Hamburg—new urban shear-wave reflection seismic system enables high-resolution imaging of subrosion structures: Journal of Applied Geophysics, v. 78, p. 133−143. https://doi.org/10.1016/j.jappgeo.2011.02.003.
Krizek, K.J., 2003, Neighborhood services, trip purpose, and tour-based travel: Transportation, v. 30, no. 4, p. 387−410. https://doi.org/10.1023/A:1024768007730.
Lamelas, M.T., Marinoni, O., Hoppe, A., and De La Riva, J., 2008, Doline probability map using logistic regression and GIS technology in the central Ebro Basin (Spain): Environmental Geology, v. 54, no. 5, p. 963−977. https://doi.org/10.1007/s00254-007-0895-3.
Lee, E.M., and Jones, D.K., 2004, Landslide Risk Assessment. London: Thomas Telford.
Margiotta, S., Negri, S., Parise, M., and Valloni, R., 2012, Mapping the susceptibility to sinkholes in coastal areas, based on stratigraphy, geomorphology and geophysics: Natural Hazards, v. 62, no. 2, p. 657−676. https://doi.org/10.1007/s11069-012-0100-1.
McCormack, G.R., Giles-Corti, B., and Bulsara, M., 2008, The relationship between destination proximity, destination mix and physical activity behaviors: Preventive Medicine, v. 46, no. 1, p. 33−40. https://doi.org/10.1016/j.ypmed.2007.01.013.
Molina, S., Lang, D.H., and Lindholm, C.D., 2010, SELENA–An open-source tool for seismic risk and loss assessment using a logic tree computation procedure: Computers & Geosciences, v. 36, no. 3, p. 257−269. https://doi.org/10.1016/j.cageo.2009.07.006.
Moser, D., Zechmeister, H.G., Plutzar, C., Sauberer, N., Wrbka, T., and Grabherr, G., 2002, Landscape patch shape complexity as an effective measure for plant species richness in rural landscapes: Landscape Ecology, v. 17, no. 7, p. 657−669. https://doi.org/10.1023/A:1021513729205.
Nsengiyumva, J.B., Luo, G., Nahayo, L., Huang, X., and Cai, P., 2018, Landslide susceptibility assessment using spatial multi-criteria evaluation model in Rwanda: International Journal of Environmental Research and Public Health, v. 15, no. 2, p. 243. https://doi.org/10.3390/ijerph15020243.
Parise, M., 2010, Hazards in karst, *in* Sustainability of the Karst Eenvironment: Dinaric Karst and Other Karst Regions, Bonacci, O., ed., IHP-VII UNESCO, Series on Groundwater No. 2, p. 155−162.

Parise, M., 2015a, A procedure for evaluating the susceptibility to natural and anthropogenic sinkholes: Georisk, v. 9, no. 4, p. 272−285. https://doi.org/10.1080/17499518.2015.1045002.

Parise, M., 2015b, Karst geo-hazards: Causal factors and management issues: Acta Carsologica, v. 44, no. 3, p. 401. https://doi.org/10.3986/ac.v44i3.1891.

Parise, M., Ravbar, N., Živanović, V., Mikszewski, A., Kresic, N., Mádl-Szőnyi, J., and Kukurić, N., 2015, Hazards in karst and managing water resources quality, *in* Karst Aquifers—Characterization and Engineering, Springer, Cham, p. 601−687. https://doi.org/10.1007/978-3-319-12850-4_17.

Peduzzi, P., Dao, H., Herold, C., and Mouton, F., 2009, Assessing global exposure and vulnerability towards natural hazards: the Disaster Risk Index: Natural Hazards and Earth System Sciences, v. 9, no. 4, p. 1149−1159. https://doi.org/10.5194/nhess-9-1149-2009.

Peduzzi, P., and Herold, H.D.C., 2005, Mapping disastrous natural hazards using global datasets: Natural Hazards, v. 35, no. 2, p. 265−289. https://doi.org/10.1007/s11069-004-5703-8.

Porter, J., and Thomson, K.C., 1975, Geology, geomorphology and karst development in the Nixa karst area, Southwestern Missouri: Geosciences Series 2, Department of Geography and Geology, Southwest Missouri State University.

Qiu, X. and Wu, S., 2017, A Knowledge-based computerized approach to the development of a sinkhole database: The Professional Geographer, v. 69, no. 2, p. 239−250. https://doi.org/10.1080/00330124.2016.1229622.

Reese, S.O., and Kochanov, W.E., 2003, Digital karst density layer and compilation of mapped karst features in Pennsylvania, U.S. Geological Survey Open-File Report, p. 3−471.

Sarker, J.K., Ansary, M.A., Rahman, M.S., and Safiullah, A.M.M., 2010, Seismic hazard assessment for Mymensingh, Bangladesh: Environmental Earth Sciences, v. 60, no. 3, p. 643−653. https://doi.org/10.1007/s12665-009-0204-4.

Schmidt, J., Matcham, I., Reese, S., King, A., Bell, R., Henderson, R., Smart, G., Cousins, J., Smith, W., and Heron, D., 2011, Quantitative multi-risk analysis for natural hazards: A framework for multi-risk modelling: Natural Hazards, v. 58, no. 3, p. 1169−1192. https://doi.org/10.1007/s11069-011-9721-z.

Seale, L.D., Florea, L.J., Vacher, H.L., and Brinkmann, R., 2008, Using ALSM to map sinkholes in the urbanized covered karst of Pinellas County, Florida—1, methodological considerations: Environmental geology, v. 54, no. 5, p. 995−1005. https://doi.org/10.1007/s00254-007-0890-8.

Siart, C., Bubenzer, O., and Eitel, B., 2009, Combining digital elevation data (SRTM/ASTER), high resolution satellite imagery (Quickbird) and GIS for geomorphological mapping: A multi-component case study on Mediterranean karst in Central Crete: Geomorphology, v. 112, no. 1−2, p. 106−121. https://doi.org/10.1016/j.geomorph.2009.05.010.

Sowers, G.F., 1996, Building on sinkholes: design and construction of foundations in karst terrain, American Society of Civil Engineers. https://doi.org/10.1061/9780784401767.

Spooner, J.D., and Kaufmann, J.E., 2007, Identifying the primary factors that determine the occurrence of sinkholes in the Ozarks, *in* Poster session presented at the annual meeting of the Geological Society of America, Denver, CO.

Stocks, L., 2007, Image-object analysis for sinkhole inventory, *in* Papers and Proceedings of Applied Geography Conferences, v. 30, p. 447.

Stohr, C.J., Ivany, G.S., and Williams, J.H., 1981, Geologic aspects of hazardous-waste isolation in Missouri, Missouri Department of Natural Resources, Division of Geology and Land Survey, 55 p.

Taheri, K., Gutiérrez, F., Mohseni, H., Raeisi, E. and Taheri, M., 2015, Sinkhole susceptibility mapping using the analytical hierarchy process (AHP) and magnitude–frequency relationships: A case study in Hamadan province, Iran: Geomorphology, v. 234, p. 64−79. https://doi.org/10.1016/j.geomorph.2015.01.005.

Thomas, B., and Roth, M.J., 1999, Evaluation of site characterization methods for sinkholes in Pennsylvania and New Jersey: Engineering Geology, v. 52, no. 1−2, p. 147−152. https://doi.org/10.1016/S0013-7952(98)00068-4.

Troester, J.W., White, E.L., and White, W.B., 1984, A comparison of sinkhole depth frequency distributions in temperate and tropic karst regions, *in* Multidisciplinary Conference on Sinkholes, v. 1, p. 65−73.

USDA, 2011, Digital Elevation Model (DEM) Whitepaper, https://www.nrcs.usda.gov/Internet/FSE_DOCUMENTS/stelprdb1047930.pdf [accessed August 18, 2019].

Van Westen, C.J., Rengers, N., and Soeters, R., 2003, Use of geomorphological information in indirect landslide susceptibility assessment: Natural Hazards, v. 30, no. 3, p. 399−419. https://doi.org/10.1023/B:NHAZ.0000007097.42735.9e.

Van Westen, C.J., 2013, Remote sensing and GIS for natural hazards assessment and disaster risk management: Treatise on geomorphology, v. 3, p. 259−298. https://doi.org/10.1016/B978-0-12-374739-6.00051-8.

Wall, J., Bohnenstiehl, D.R., Wegmann, K.W., and Levine, N.S., 2017, Morphometric comparisons between automated and manual karst depression inventories in Apalachicola National Forest, Florida, and Mammoth Cave National Park, Kentucky, USA: Natural Hazards, v. 85, no. 2, p. 729−749. https://doi.org/10.1007/s11069-016-2600-x.

Weier, J., and Herring, D., 2000, Measuring Vegetation (NDVI & EVI), https://earthobservatory.nasa.gov/features/MeasuringVegetation [accessed August 18, 2019].

Wu, S., Qiu, X., Usery, E.L., and Wang, L., 2009, Using geometrical, textural, and contextual information of land parcels for classification of detailed urban land use: Annals of the Association of American Geographers, v. 99, no. 1, p. 76−98. https://doi.org/10.1080/00045600802459028..

Wu, S., Wang, L., and Qiu, X., 2008, Incorporating GIS building data and census housing statistics for sub-block-level population estimation: The Professional Geographer, v. 60, no. 1, p. 121−135. https://doi.org/10.1080/00330120701724251.

Zhou, W., and Beck, B.F., 2008, Management and mitigation of sinkholes on karst lands: an overview of practical applications: Environmental Geology, v. 55, no. 4, p. 837−851. https://doi.org/10.1007/s00254-007-1035-9.

Zhu, J., Taylor, T.P., Currens, J.C., and Crawford, M.M., 2014, Improved karst sinkhole mapping in Kentucky using LiDAR techniques: a pilot study in Floyds Fork Watershed: Journal of Cave and Karst Studies, v. 76, no. 3, p. 207. https://doi.org/10.4311/2013ES0135

Zisman, E.D., 2001, A standard method for sinkhole detection in the Tampa, Florida, area: Environmental & Engineering Geoscience, v. 7, no. 1, p. 31−50. https://doi.org/10.2113/gseegeosci.7.1.31.

Zisman, E.D., 2008, A method of quantifying sinkhole risk, *in* Sinkholes and the Engineering and Environmental Impacts of Karst, p. 278−287. https://doi.org/10.1061/41003(327)27..

Zumpano, V., Pisano, L., and Parise, M., 2019, An integrated framework to identify and analyze karst sinkholes: Geomorphology, v. 332, p. 213−225. https://doi.org/10.1016/j.geomorph.2019.02.013.

Michal Rendoš, Dana Miklisová, Ľubomír Kováč, and Andrej Mock. Dynamics of Collembola (Hexapoda) in a forested limestone scree slope, Western Carpathians, Slovakia. *Journal of Cave and Karst Studies*, v. 82, no. 1, p. 18-29. DOI:10.4311/2018LSC0140

DYNAMICS OF COLLEMBOLA (HEXAPODA) IN A FORESTED LIMESTONE SCREE SLOPE, WESTERN CARPATHIANS, SLOVAKIA

Michal Rendoš[1,C], Dana Miklisová[2], Ľubomír Kováč[3], and Andrej Mock[3]

Abstract

A labyrinth of air-filled voids in forested scree slopes represents one of the most common types of terrestrial shallow subterranean habitats in the temperate zone, characterized by relatively strong seasonal fluctuations of temperature and the occurrence of subterranean species of invertebrates. We carried out a year-long study to define the monthly activity dynamics of Collembola communities inhabiting a depth profile (95 cm from the ground surface) of a forested limestone scree in the Western Carpathians, Slovakia. We assessed the response of species sorted into four separate ecological forms, reflecting their affinity to the subterranean environment and to temperature parameters fluctuating over the year. Of the 62 collembolan species identified, 28 were assigned to trogloxenes, 19 to subtroglophiles, 12 to eutroglophiles, and 3 to troglobionts. Fluctuations of activity/numbers during the year were observed in all four ecological forms of Collembola and at all depths. Troglobionts and eutroglophiles, associated predominantly with deeper layers of the scree slope profile, preferred the lower temperature ranges and were typical for the autumn months. Trogloxenes and subtroglophiles were active most of the year near the surface, but specifically during the spring months characterized by higher temperature ranges. The study contributes to the general knowledge of dynamics of invertebrate activity in a forested temperate zone scree slope.

Introduction

The interior of forested scree slopes at the foot of steep valley sides comprises a relatively common type of terrestrial shallow subterranean habitat in the temperate climate zone (Culver and Pipan, 2008, 2014). The *Milieu Souterrain Superficiel* (MSS), as this habitat is generally referred to (Juberthie et al., 1980, 1981), lies between the base of the soil horizon and bedrock and consists of an extensive network of lightless air-filled voids that formed within the multiple layers of fragmented rocks. In karst areas, the network of voids is ordinarily interconnected with deep subterranean habitats (i.e., caves, along with adjacent narrow fissures formed in the limestone bedrock) (Juberthie, 1983, 2000; Juberthie and Decu, 2004; Giachino and Vailati, 2010; Mammola et al., 2016). Compared to the deepest parts of the caves, where the temperature fluctuates only minimally during the year, an MSS habitat with a developed soil layer is still largely influenced by the seasonality of the above-ground weather (Pipan et al., 2010; Mammola et al., 2016). Although the temperature regime inside forested scree slopes is characterized by a reduction of temperature extremes, as well as by moderating daily temperature fluctuations, it usually exhibits relatively strong seasonal temperature variations (e.g. Nitzu et al., 2006–2007; Zacharda et al., 2007; Rendoš et al., 2012; Gilgado et al., 2014; Mammola et al., 2017).

The proximity of soil and deep cave habitats causes the scree slope interior to be populated by diverse invertebrate fauna varying in affinity to the subterranean environment. Besides the invertebrate species typically found to inhabit soil, subterranean species known from caves, many of them with apparent morphological adaptations to life in a constantly dark environment, occur in this habitat (Juberthie, 2000; Nitzu et al., 2014; Jiménez-Valverde et al., 2015; Mammola et al. 2016; Rendoš et al., 2016). Despite the intensive research on shallow subterranean habitats conducted in several European countries over the last decades (e.g. Juberthie et al., 1980; Růžička and Klimeš, 2005; Giachino and Vailiati, 2010; Laška et al., 2011; Pipan et al., 2010; Nitzu et al., 2014; Jiménez-Valverde et al., 2015; Mammola et al., 2017), very little is still known about the impact of seasonal temperature variations on the activity of particular invertebrate species living therein. Previous authors (e.g. Racovitza and Şerban, 1982; Rendoš et al., 2012, Nitzu et al., 2014) have pointed out that the activity of various invertebrate groups inhabiting shallow subterranean habitats fluctuates considerably throughout the year. Crouau-Roy et al. (1992) observed the abundance of the troglobitic beetle *Speonomus hydrophilus* (Jeannel, 1907) to be associated with seasonal temperature changes that occurred in the MSS; it markedly declined in both summer and winter.

We carried out a year-long study focused on Collembola, one of the most diversified groups of invertebrates in subterranean habitats (Deharveng, 2004), inhabiting a limestone forested scree slope in the Western Carpathians, Slovakia. Our aim was: (1) to describe the activity dynamics of collembolan communities along the scree profile during the year, and (2) to assess the response of particular collembolan species to temperature parameters fluctuating over the

[1]Department of Ecology, Faculty of Humanities and Natural Sciences, University of Prešov, 17. novembra 1, SK-08116, Prešov, Slovakia.
[2]Institute of Parasitology, Slovak Academy of Sciences, Hlinkova 3, SK-04001, Košice, Slovakia.
[3]Institute of Biology and Ecology, Faculty of Science, P.J. Šafárik University, Šrobárova 2, SK-04154, Košice, Slovakia.
[C]Corresponding Author: michal.rendos@gmail.com

year. We hypothesized that subterranean species of Collembola would prefer, unlike the common soil-dwelling species, narrow ranges of temperature and would be active in the scree slope predominantly in cooler months. We expected all collembolans to be frost-sensitive.

Material and Methods

Study Site

The Sivec Nature Reserve, located 8 km southwest of the village of Malá Lodina in Eastern Slovakia, is a small karst island within the Čierna Hora Mountains (Western Carpathians, Central Europe) built predominantly on old crystalline rocks (Hochmuth, 2008). The reserve territory, with an area of 1.7 km^2, includes the approximately 1.5 km long upper part of the Malý Ružínok Valley along with an extensive Mesozoic limestone cliff on the valley's left side, flanked by steep scree slopes. Several shallow caves harbouring endemic invertebrates, including Collembola, have formed inside the cliff (Mock and Tajovský, 2008; Kováč and Papáč, 2010).

The study site has a typical northern temperate climate. According to climatic data provided by the nearby meteorological station of the Slovak Hydrometeorological Institute in the village of Košická Belá, the mean annual temperature (November 2008–October 2009) was +10.6 °C, and the average annual precipitation was 61.2 mm. The coldest month was January with an average monthly temperature of −2.9 °C, and the warmest was July (+21.6 °C). The highest precipitation amounts were recorded in December (96.5 mm) and the lowest in November (21.7 mm). A layer of snow covered the nature reserve continuously from late January to early March. More details about the climatic characteristics are given in Figure 1.

The sampling stand (coordinates: 48°50.5′ N, 21°06.6′ E) is situated a few metres below the top of an 15–20° inclined forested scree slope facing north-east at an altitude of 530 m and overgrown with *Tilieto-Aceratum* forest and a scarce herbal layer formed by *Asplenium alternifolium*, *Dentaria* sp., *Lamium* sp., *Mercurialis perennis*, *Urctica dioica,* young seedlings of *Sambucus* sp., and ferns. The investigated scree slope profile consists of three distinct layers: leaf litter and humus (0–15 cm), an organo-mineral layer (15–45 cm) clearly separated from scree that occupies a horizon from 45 cm downwards and is formed by rock fragments with a diameter of 10–15 cm. The dominant soil type on the stand was rendzina (FAO classification of soil types) (IUSS Working Group WRB, 2015).

Sampling and Species Determination

To sample Collembola, subterranean pitfall traps were buried once beneath the scree slope surface after Schlick-Steiner and Steiner (2000). Each trap consisted of a plastic cylinder (length 110 cm, diameter 10.5 cm) circumferentially perforated by openings (diameter 0.8 cm) at ten regular horizontal levels (5, 15, 25, up to 95 cm). A demountable set of 10 plastic cups (volume 500 ml) filled with 4% formaldehyde preservative solution was inserted into the plastic cylinder interior. The cups were placed right under the openings on the cylinder surface, enabling individuals to be trapped at the particular level (for more details on subterranean trap design, see Rendoš et al., 2016). A triplet of subterranean pitfall traps were placed 50 cm from one another over a previously excavated pit more than a metre deep. Thereafter, the pit was backfilled with the dugout soil and rocks in the original order of the layers and the tops of cylinders were tightly closed with a plastic lid. The plastic cups were pulled out of the plastic cylinder and emptied once a month, from November 2008 to October 2009. The individuals trapped were poured into plastic bottles, transferred to the laboratory and sorted to the level of higher taxa. Collembola were mounted on permanent microscopic slides after Rusek (1975) and determined to the species level using a Leica DM1000 phase-contrast microscope and identification keys, such as those by Pomorski (1998), Bretfeld (1999), Potapov (2001), Thibaud et al. (2004), and others. Based on the experience of biospeleological inventories carried out in the Slovak caves in the past decades (e.g., Kováč, 2000; Kováč et al., 2016), the Collembola species were divided into four ecological forms reflecting their degree of affinity for subterranean environment, as proposed by Sket (2008): (1) Trogloxenes – species inhabiting the ground surface and uppermost layers of the soil horizon (leaf litter and humus). Their occurrence in subterranean habitats is accidental, as they are unable to reproduce and complete their life cycle in them; (2) Subtroglophiles – species commonly found in subterranean habitats but still intimately interacting with the surface and uppermost layers of the soil horizon during certain periods to complete some of their biological functions, such as dispersal, feeding, or reproduction; (3) Eutroglophiles – essentially edaphic species that are able to maintain permanent and self-sustaining subterranean populations; and (4) Troglobionts – species exclusively inhabiting subterranean habitats.

Temperature Measurements

The temperature was measured continuously throughout the study period at four-hour intervals using two series of iButton DS1921G thermo-data loggers affixed to the top of the plastic lid (=surface) closing the subterranean trap and to the walls of plastic cups at the depths of 15, 35, 55, 75 and 95 cm. For each sampling period and each measured depth, the temperature data were converted into the following variables: monthly temperature mean (*Tmean*), monthly temperature maximum (*Tmax*) and minimum (*Tmin*), and derived monthly temperature range (*Trange* = *Tmax* − *Tmin*).

Both thermo-data loggers placed at 75 cm stopped functioning for a long period, which caused incomplete temperature data from this depth.

Data Analysis

The values of monthly collembolan activity were calculated as the average number of individuals sampled by the triad of subterranean traps standardized for 30 days (1 month). The dynamics of collembolan activity during the study period were depicted graphically for each depth and ecological form separately. We performed redundancy analysis (RDA) to evaluate associations of collembolan communities from four depths (15, 35, 55 and 95 cm) with 12 months and the measured temperature parameters. In this analysis, depth, month, temperature mean and temperature average were employed as explanatory variables. Response variables were represented by the activity of selected collembolan species based on numbers. To obtain a clear ordination plot, only species with total activity ≥ 5 (19 species altogether) were included in the analysis, covering 98.5 % of total collembolan numbers. A log-transformation was applied to the data. The analyses were performed using Canoco for Windows 5 software package (Ter Braak and Šmilauer, 2012).

Results

Temperature Characteristics

The temperature regime recorded within the scree slope profile was characterized by gradual reduction of daily temperature fluctuations with increasing depth (i.e., the temperature remained constant for several consecutive days in deeper layers of the scree slope profile; for more details, see Figure 1 in Rendoš et al., 2012). Deeper under the surface, the long-term temperature fluctuations still coincided with the seasonal climate variations occurring on the surface (Fig. 1). In winter, the temperature dropped below the freezing point only on the surface for a few days at the turn of December and January, with the lowest recorded temperature of −4.0 °C. The monthly temperature means increased from the surface downwards, while the monthly temperature ranges were gradually diminished by increasing depth. During the year, the monthly temperature means on the surface ranged between 0.2 °C (January) to 16.6 °C (July). In contrast, these means at the depth of 95 cm ranged between 3.5 °C (March) to 15.2 °C (August). Monthly temperature ranges varied from 5.0 °C (February) to 12.5 °C (September) on the surface and from 0.5°C (February, March) to 4.5 °C (June) at 95 cm (Table 1).

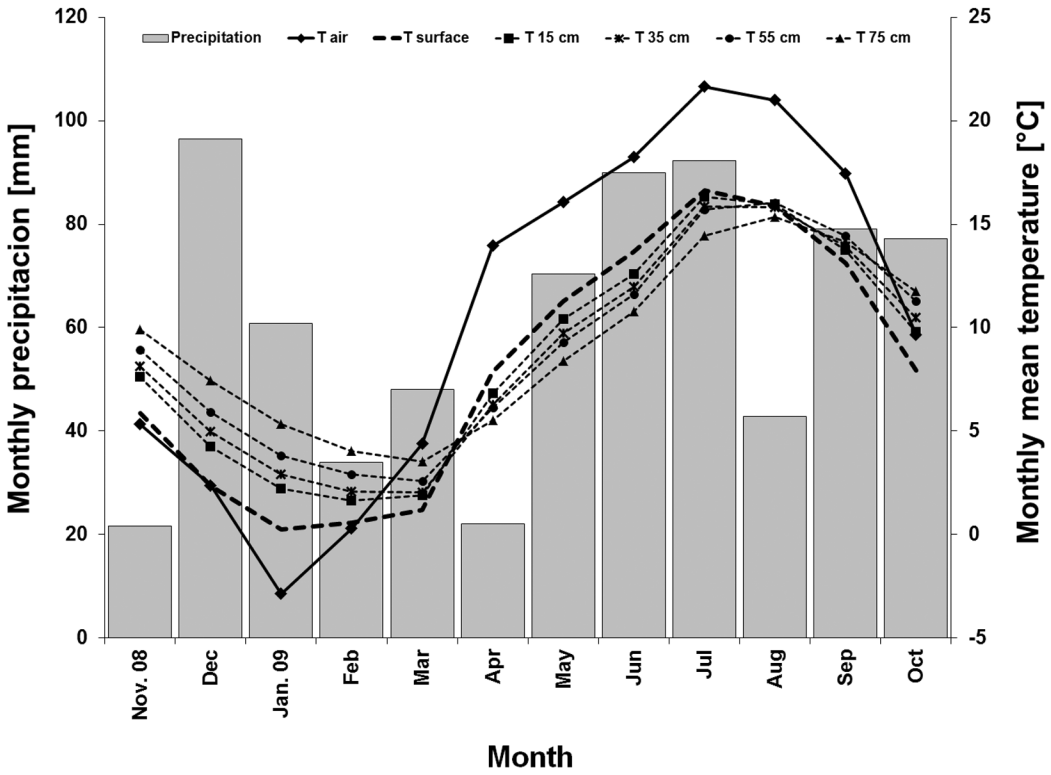

Figure 1. Monthly data of mean air temperature (T air) and precipitation recorded by the nearest meteorological station in the village of Košická Belá along with monthly data of mean air temperature during the study period (Nov. 2008–Oct. 2009) measured by thermo-data loggers on the soil surface (T surface) and at the depths of 15 cm (T 15), 35 cm (T 35), 55 cm (T 55), and 95 cm (T 95).

Diversity and Seasonal Dynamics of Collembolan Communities

In the course of the study, more than 17,000 Collembola individuals representing 62 species were trapped across the depth profile by a triplet of subterranean pitfall traps. Variations in collembolan activity and species number among the triplet of traps buried in the scree slope profile can be seen in Appendix 1. Of the total species number identified, 28 species were assigned to trogloxenes (*n* = 486), 19 to subtroglophiles (*n* = 14,619), 12 to eutroglophiles (*n* = 1821) and 3 to troglobionts (*n* = 353) (Table 2). At the depths of 5 to 25 cm, we found the species number to be the highest between April and June. Deeper in the scree

Table 1. Monthly temperature characteristics recorded along the scree slope profile.

Month	Depth, cm	Monthly temperature, °C			
		Mean	Min	Max	Range
November 2008					
	Surface	7.0	1.8	12.3	10.5
	15	8.5	5.0	11.5	6.5
	35	9.0	6.3	11.5	5.3
	55	9.7	7.5	11.5	4.0
	75	...	...	...	...
	95	10.5	9.0	11.8	2.8
December 2008					
	Surface	2.4	-1.3	6.0	7.3
	15	4.3	2.5	5.5	3.0
	35	5.1	3.8	6.8	3.0
	55	6.1	5.0	7.8	2.8
	75	...	...	...	...
	95	7.6	6.5	9.0	2.5
January 2009					
	Surface	0.2	-2.3	3.5	5.8
	15	2.2	1.5	2.5	1.0
	35	2.9	2.3	3.8	1.5
	55	3.8	3.0	5.0	2.0
	75	...	...	...	...
	95	5.4	4.5	6.5	2.0
February 2009					
	Surface	0.6	0.0	5.0	5.0
	15	1.6	1.5	2.5	1.0
	35	2.1	1.8	2.5	0.8
	55	2.9	2.5	3.0	0.5
	75	...	...	...	...
	95	4.0	3.8	4.3	0.5
March 2009					
	Surface	1.5	-1.0	8.3	9.3
	15	2.1	1.0	4.5	3.5
	35	2.2	1.5	3.8	2.3
	55	2.7	2.5	3.5	1.0
	75	...	...	...	...
	95	3.5	3.5	4.0	0.5
April 2009					
	Surface	8.4	5.5	12.8	7.3
	15	7.4	5.0	8.5	3.5
	35	6.9	4.3	7.8	3.5
	55	6.7	4.0	7.8	3.8
	75	...	...	...	...
	95	6.0	4.0	7.3	3.3
May 2009					
	Surface	11.6	8.0	16.8	8.8
	15	10.8	8.5	13.0	4.5
	35	10.2	7.8	12.0	4.3
	55	9.8	7.8	11.3	3.5
	75	...	...	...	...
	95	9.0	7.3	10.3	3.0
June 2009					
	Surface	15.3	10.0	19.3	9.3
	15	14.2	11.0	16.5	5.5
	35	13.4	10.3	15.8	5.5
	55	12.8	10.0	15.5	5.5
	75	...	...	...	...
	95	11.7	9.8	14.3	4.5
July 2009					
	Surface	16.6	13.0	20.5	7.5
	15	16.4	14.5	18.5	4.0
	35	16.0	14.5	17.5	3.0
	55	16.0	15.0	17.5	2.5
	75	15.3	14.3	16.0	1.8
	95	14.9	14.0	15.3	1.3
August 2009					
	Surface	15.2	10.0	20.0	10.0
	15	15.5	11.0	17.0	6.0
	35	15.5	11.5	17.0	5.5
	55	15.8	13.5	17.0	3.5
	75	15.3	13.8	16.3	2.5
	95	15.2	14.3	15.8	1.5
September 2009					
	Surface	11.2	3.5	16.0	12.5
	15	12.4	8.0	14.5	6.5
	35	12.8	9.0	14.0	5.0
	55	13.4	10.8	14.8	4.0
	75	13.3	11.3	14.8	3.5
	95	13.4	11.8	14.8	3.0
October 2009					
	Surface	5.6	1.5	10.5	9.0
	15	7.4	5.5	9.5	4.0
	35	8.3	7.0	10.0	3.0
	55	9.1	7.8	10.8	3.0
	75	9.5	8.3	11.8	3.5
	95	10.0	8.5	11.8	3.3

slope profile, the species number increased rather tardily from the end of winter and attained the maximum values at the turn of summer and autumn (August, September).

Looking at overall seasonal dynamics of locomotory activity in particular ecological forms of Collembola, we found troglobionts to have the lowest activity among the other forms (Fig. 2). Throughout the study period, the presence of troglobionts was concentrated primarily in the deeper layers of the scree slope profile (65–95 cm). Activity of troglobitic collembolans increased slightly from the beginning of spring (March) to early summer (June). After a mild summer decline, an autumn increase of troglobiont activity was recorded. In contrast, trogloxenes occurred almost exclusively in the uppermost level (5 cm) of the depth profile during the year, with maximum activity registered in spring (April–June). Unlike the previous two ecological forms, eutroglophiles and subtroglophiles were active across the entire depth profile throughout the year. At most depths, the activity of eutroglophiles had a similar pattern, characterized by the gradual increase from the end of winter (March) to spring (April, May). After an apparent decrease in summer, the activity of eutroglophiles increased again, reaching a second peak at the end of summer (August), which continued at the deepest levels (85 and 95 cm) until the following autumn months (September, October). At the depths of 55 to 85 cm, the second peak of eutroglophile activity was more pronounced than the first one. During the year, the highest activity of subtroglophiles was recorded at the uppermost levels (5 and 15 cm), with the maximum values attained in April. At most deeper layers of the scree slope profile, two rather prolonged activity peaks were observed during the year in subtroglophiles: the first at the turn of spring and

Table 2. List of collembolan species collected over the study period in the scree slope profile and the sums of their monthly activities calculated as the average number of individuals sampled by the triad of subterranean traps and standardized for 30 days.

Species	Ecological Form	Total Number of Individuals	Monthly Activity												Total Activity
			Nov 2008	Dec 2008	Jan 2009	Feb 2009	Mar 2009	Apr 2009	May 2009	Jun 2009	Jul 2009	Aug 2009	Sep 2009	Oct 2009	
Allacma fusca (Linné, 1758)	Trogloxene	12	···	···	···	···	···	1.21	1.61	0.31	···	0.61	···	···	3.74
Anurida vontoernei Nosek, 1962	Trogloxene	1		···	···	···	···	···	···	···	···	0.30	···	···	0.30
Caprainea marginata (Schött, 1893)	Trogloxene	30	0.24	···	···	···	···	1.52	2.58	3.13	1.11	0.30	···	0.59	9.46
Ceratophysella denticulata (Bagnall, 1941)	Eutroglophile	98	···	···	···	···	7.43	2.12	1.94	11.25	1.11	4.24	1.25	0.29	29.63
Ceratophysella granulate Stach, 1949	Eutroglophile	26	···	···	0.65	···	···	1.82	3.55	···	2.59	···	···	···	8.60
Ceratophysella luteospina (Stach, 1920)	Subtroglophile	2	···	···	···	···	···	···	···	0.31	···	···	···	0.29	0.61
Ceratophysella silvatica (Rusek, 1964)	Subtroglophile	122	0.95	0.59	···	···	2.57	4.85	5.48	6.56	0.74	14.24	0.75	0.29	37.03
Desoria divergens(Axelson, 1900)	Subtroglophile	5	···	···	···	···	···	1.21		0.31	···	···	···	···	1.52
Desoria hiemalis (Schött, 1893)	Subtroglophile	1	···	···	···	···	0.29	···	···	···	···	···	···	···	0.29
Desoria propinqua (Axelson, 1902)	Subtroglophile	42	0.24	0.88	0.97	4.64	2.00	···	0.97	0.31	0.37	···	···	2.94	13.32
Desoria tigrina Nicolet, 1842	Subtroglophile	1795	2.14	1.18	2.58	4.64	9.43	79.70	137.74	183.44	54.07	72.42	13.25	3.82	564.42
Deuterosminthurus sp. juv.		6	···	···	···	···	···	0.91	0.65	···	···	0.30	···	···	1.86
Deutonura conjuncta (Stach, 1926)	Trogloxene	2	···	···	···	···	···	···	···	0.63	···	···	···	···	0.63
Dicyrtoma fusca (Lubbock, 1873)	Trogloxene	48	···	···	···	···	10.57	1.21	0.32	0.94	0.37	0.61	···	···	14.02
Dicyrtomina ornata (Nicolet, 1842)	Trogloxene	80	···	···	···	···		12.12	6.45	2.19	0.74	1.52	···	1.76	24.78
Dicyrtomina violacea (Krausbauer, 1898)	Trogloxene	16	···	···	···	···	···	4.85	···	···	···	···	···	···	4.85
Entomobryidae juv.		9	···	···	···	···	0.57	···	1.94	···	0.37	···	···	···	2.88
Folsomia fimetaria (Linné, 1758)	Subtroglophile	119	0.24	···	···		0.29	0.61	3.23	2.19	1.85	13.64	9.50	2.94	34.47
Folsomia lawrencei Rusek, 1984	Eutroglophile	16	···	···	···	0.36	···	···	0.32	0.63	···	1.21	1.50	0.59	4.61
Folsomia manolachei Bagnall, 1939	Trogloxene	32	···	···	···	···	···	1.21	1.29	3.75	0.74	2.73	0.25	···	9.97
Folsomia penicula Bagnall, 1939	Trogloxene	2	···	···	···	···	···	···	···	···	···	···	···	0.59	0.59
Friesea mirabilis (Tullberg, 1871)	Trogloxene	1	···	···	···	···	···	0.30	···	···	···	···	···	···	0.30
Gisinianus flammeolus Gisin, 1957	Trogloxene	2	0.24	···	···	···	···	···	···	···	···	0.30	···	···	0.54
Hymenaphorura sp.	Subtroglophile	1	···	···	0.32	···	···	···	···	···	···	···	···	···	0.32
Choreutinula inermis (Tullberg, 1871)	Trogloxene	8	···	···	···	···	···	···	···	···		2.42	···	···	2.42
Isotomiella minor (Schäffer, 1896)	Subtroglophile	7	···	···	···	···	···	···	···	···	0.74	1.21	0.25	···	2.20
Kalaphorura paradoxa (Schäffer, 1900)	Eutroglophile	3	···	0.88	···	···	···	···	···	···	···	···	···	···	0.88
Lepidocyrtus lignorum (Fabricius, 1775)	Subtroglophile	12053	247.86	77.65	64.84	33.21	218.29	1464.24	750.32	240.94	60.37	52.42	87.75	315.88	3613.77

Table 2. (Continued).

Species	Ecological Form	Total Number of Individuals	Monthly Activity												Total Activity
			Nov 2008	Dec 2008	Jan 2009	Feb 2009	Mar 2009	Apr 2009	May 2009	Jun 2009	Jul 2009	Aug 2009	Sep 2009	Oct 2009	
Lepidocyrtus violaceus (Fourcroy, 1785)	Trogloxene	8	···	···	···	···	···	···	0.65	0.63	0.37	0.91	···	···	2.55
Lipothrix lubbocki (Tullberg, 1872)	Trogloxene	8	···	···	···	···	···	···	0.65	1.56	0.37	···	···	···	2.58
Megalothorax carpaticus Papáč et Kováč, 2013	Troglobiont	1	···	···	···	···	···	···	···	···	···	···	···	0.29	0.29
Megalothorax hipmani Papáč et Kováč, 2013	Troglobiont	27	···	···	···	···	···	···	0.32	0.63	1.11	4.55	0.50	1.18	8.28
Megalothorax incertus Börner, 1903	Eutroglophile	13	···	···	···	···	···	···	0.32	0.63	···	2.42	···	0.59	3.96
Megalothorax minimus Willem, 1900	Eutroglophile	1	···	···	···	···	···	···	0.32	···	···	···	···	···	0.32
Micranurida pygmaea Börner, 1901	Trogloxene	1	···	···	···	···	···	···	···	···	0.37	···	···	···	0.37
Morulina verrucosa (Börner, 1903)	Trogloxene	62	0.95		0.32		0.29	1.52	7.74	7.19	0.37	0.61	···	0.29	19.28
Neanura pseudoparva Rusek, 1963	Trogloxene	5	···	···	···	···	···	···	···	0.94	0.37	···	···	0.29	1.60
Neelides minutus (Folsom, 1901)	Subtroglophile	12	···	···	···	···	···	···	···	0.31	0.74	1.82	0.25	0.59	3.71
Neelus koseli Kováč et Papáč, 2010	Troglobiont	325	0.24	1.18	1.29	2.50	1.43	11.21	15.48	21.56	5.19	14.85	9.75	14.12	98.79
Oncopodura *crassicornis* Shoebotham, 1911	Eutroglophile	37	···	···	···	···	0.29	0.30	1.29	1.25	···	4.85	2.00	0.88	10.86
Onychiuroides pseudogranulosus (Gisin, 1951)	Subtroglophile	29	0.24	0.29	3.23	···	0.29	1.21	0.97	1.88	0.37	0.61	···	···	9.08
Orchesella flavescens (Bourlet, 1839)	Trogloxene	50	0.24	···	···	···	0.29	···	1.29	1.56	3.70	6.67	1.25	0.59	15.59
Pachyotoma recta (Stach, 1930)	Trogloxene	1		···	···	···	···	···	···	···	···	···	···	0.29	0.29
Parisotoma notabilis (Schäffer, 1896)	Subtroglophile	83	0.24	···	0.32	···	···	1.52	5.48	9.06	3.70	5.45	0.50		26.28
Plutomurus carpaticus Rusek et Weiner, 1978	Eutroglophile	952	0.24	···	1.94	2.14	2.00	10.30	10.97	20.31	10.74	107.58	62.25	48.82	277.29
Pogonognathellus flavescens (Tullberg, 1871)	Subtroglophile	187	0.24	···	···	0.36	0.29	1.52	9.68	17.81	9.26	13.94	3.50	2.06	58.64
Protaphorura armata (Tullberg, 1869)	Eutroglophile	352	0.71	1.18	3.23	5.71	8.29	39.09	25.48	10.63	1.85	4.55	4.25	3.24	108.20
Protaphorura aurantiaca (Ridley, 1880)	Subtroglophile	8	0.24				0.29	0.30	0.65	0.31	0.37	0.30			2.46
Pseudachorutella asigillata (Börner, 1901)	Trogloxene	7	···	···	···	···	···	0.61	0.32	···	0.37	···	···	0.88	2.18
Pseudachorutes corticicolus (Schäffer, 1896)	Trogloxene	1	···	···	···	···	···	0.30	···	···	···	···	···	···	0.30
Pseudachorutes dubius Krausbauer, 1898	Trogloxene	59	0.95	···	···	···	3.14	4.55	2.26	4.69	1.11	···	1.00	···	17.70
Pseudachorutes palmiensis (Börner, 1903)	Trogloxene	1	···	···	···	···	···	···	···	···	···	···	···	0.29	0.29
Pseudosinella horaki Rusek, 1985	Subtroglophile	7	···	···	···	···	···	0.61	···	0.63	···	0.91	···	···	2.14

Table 2. (Continued).

Species	Ecological Form	Total Number of Individuals	Monthly Activity												Total Activity
			Nov 2008	Dec 2008	Jan 2009	Feb 2009	Mar 2009	Apr 2009	May 2009	Jun 2009	Jul 2009	Aug 2009	Sep 2009	Oct 2009	
Pygmarrhopalites bifidus Stach, 1945	Eutroglophile	8	···	···	···	···	···	···	···	···	···		0.25	2.06	2.31
Pygmarrhopalites elegans Cassagnau et Delamare Deboutteville, 1953	Subtroglophile	141	···	···	···	···	···	···	···	5.31	1.11	6.67	17.00	9.12	39.21
Pygmarrhopalites principalis Stach, 1945	Eutroglophile	39	···	···	···	···	···	···	1.94	7.50	1.48	0.61	0.75		12.27
Pygmarrhopalites pygmaeus (Wankel, 1860)	Eutroglophile	276	1.67	5.59	4.84	3.93	3.71	13.03	11.94	3.75	1.11	···	0.75	33.24	83.55
*Pygmarrhopalites spinosus*Rusek, 1967	Subtroglophile	1	···	···	···	···	···	···	0.32	···	···	···	···	···	0.32
Sminthurinus aureus (Lubbock, 1862)	Trogloxene	39	2.86	0.29	···	···	···	···	···	···	···	···	0.25	7.35	10.75
Sminthurinusniger (Lubbock, 1867)	Trogloxene	1	0.24	···	···	···	···	···	···	···	···	···	···		0.24
Tetrodontophora bielanensis (Waga, 1842)	Subtroglophile	4	···	···	···	···	···	···	···	0.31	···	0.30	···	0.59	1.20
Vertagopus arboreus (Linné, 1758)	Trogloxene	5	···	···	···	0.36	0.57	0.30	···	···	0.37	···	···	···	1.60
Xenylla brevicauda Tullberg, 1869	Trogloxene	2	···	···	···	···	···	0.61	···	···	···	···	···	···	0.61
Xenylla schillei Börner, 1903	Trogloxene	2	···	···	···	0.36	···	0.30	···	···	···	···	···	···	0.66
Total number of individuals per activity		17294	261.0	89.7	84.5	58.2	272.3	1665.2	1016.5	575.3	169.6	346.1	218.8	456.8	5213.8
Species number		···	20	10	12	11	20	32	34	37	33	34	23	31	62

summer (May, June) and the second, after a short-term decline, in August. An exception was at the depth of 95 cm, where only one noticeable activity peak (September) was found during the year.

Collembolan Activity-Environmental Characteristics Relationship

The redundancy analysis (RDA) revealed activity of particular collembolan species to be affected by thermal conditions fluctuating over the year. The eigenvalues of RDA ordination axes 1 and 2 were 0.337 and 0.153, respectively, and they accounted for 61 % of total variation. The species-environment correlations were 0.883 in axis 1 and 0.949 in axis 2. The permutation test on all axes confirmed their statistical significance ($F = 4.7$, $p = 0.002$). The resulting RDA biplot diagram (Fig. 3) illustrates that the spring months (April–May) were characterized by higher temperature ranges, and the species *Ceratophysella silvatica*, *Desoria tigrina*, *Dicyrtomina ornata*, *Parisotoma notabilis*, *Pogonognathellus flavescens*, and *Pygmarrhopalites principalis* were specific to these months. In contrast, *Megalothorax hipmani*, *Neelus koseli*, *Oncopodura crassicornis*, *Protaphorura armata*, *Pygmarrhopalites elegans*, *P. pygmaeus*, *Plutomurus carpaticus* and *Pygmarrhopalites bifidus*, associated with deeper layers of the scree slope profile, preferred rather lower temperature ranges and were typical for the autumn months (September–October). *Dicyrtoma fusca* and *Lepidocyrtus lignorum*, the species inhabiting the upper layers of the scree slope profile, were characteristic for mid-summer (July). *Folsomia fimetaria* and *F. lawrencei* were grouped with a higher temperature means during the summer months, while the occurrence of *Desoria propinqua* was associated with lower temperatures in late autumn (November) and early spring (March).

Discussion

Our earlier investigation (Rendoš et al., 2012) stressed the impact of seasonal temperature changes on the activity dynamics of higher invertebrate taxa inhabiting a limestone scree slope identical with the present study. Subsequent identification of the sampled invertebrates at the species level revealed Collembola to be the only taxon among the others that includes species representing all four ecological forms differing in degree of affinity to subterranean environment. We used these Collembola as a suitable model group for the first thorough study on activity dynamics of species communities in the shallow subterranean habitat with differences in

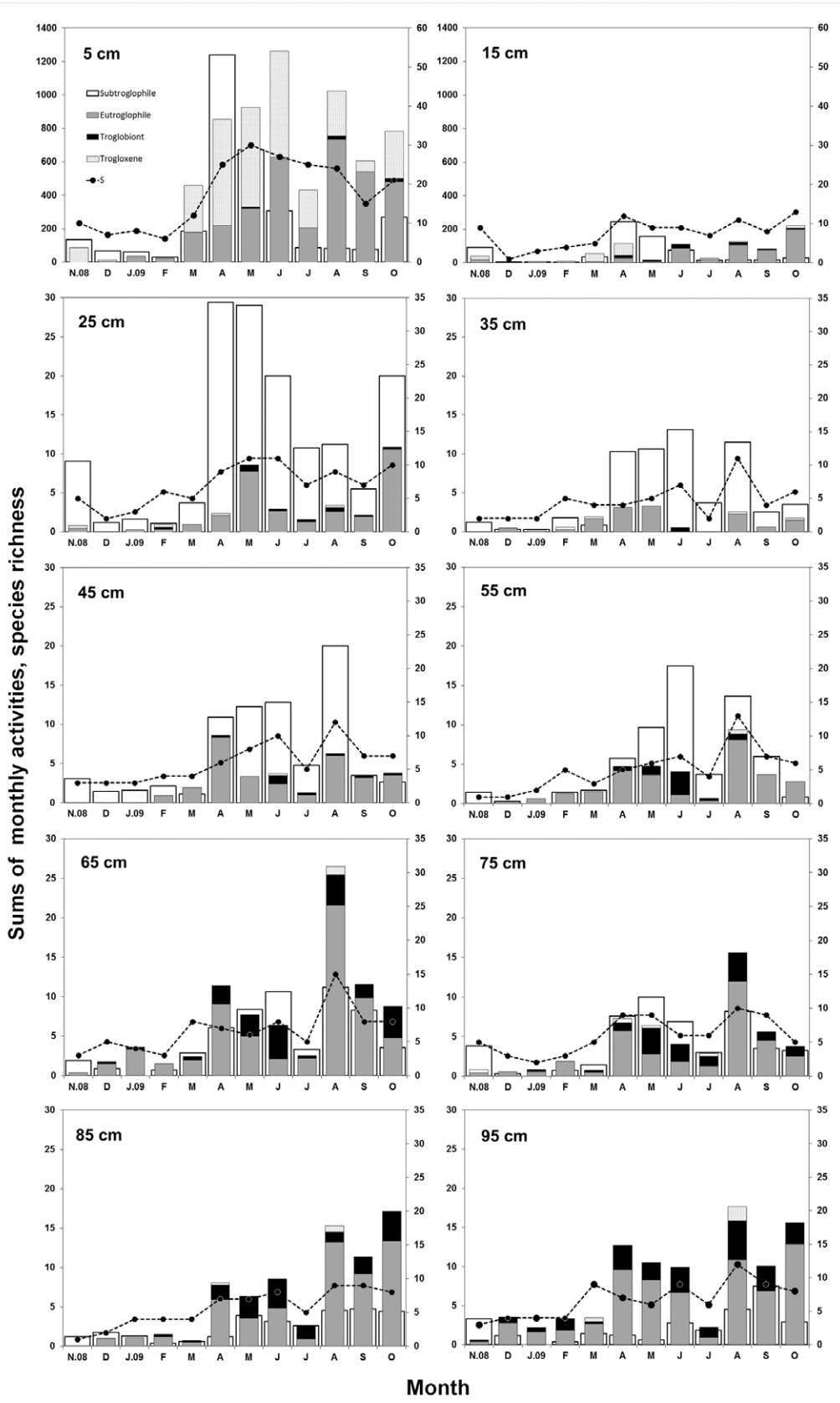

Figure 2. Activity dynamics of four collembolan ecological forms during the study period (Nov. 2008–Oct. 2009) along the scree slope profile. The activity (numbers) of subtroglophiles is depicted on the left y-axis, while the activity of trogloxenes, eutroglophiles, troglobionts and the collembolan species number (s) is depicted on the right y-axis. The graphs depicting collembolan activity at the depths of 5 and 15 cm have different scaling due to the large number of individuals captured.

temperature fluctuations between scree depth horizons.

It is important to point out that burying subterranean pitfall traps may disrupt the structure of the scree slope habitat by impermanent clogging of the air-filled voids (Mock et al., 2015; Růžička and Dolanský, 2016), which may subsequently result in the mixing of invertebrate communities occupying the scree interior and the absence of some sensitive subterranean species for a period of several months to even years. As already noted by Rendoš et al. (2016), the effect of disruption of the scree slope structure on collembolans appears to be negligible. The depth distribution of particular ecological forms as well as activities of subterranean collembolan species, including troglobionts, were not found to be noticeably altered a month after the traps had been buried in the scree slope. The individual and species number may vary within a single studied site, as found by Jiménez-Valverde et al. (2015), who buried several traps individually across a scree slope. Our study was primarily focused on activity dynamics of Collembola communities along a scree depth profile during the year. To obtain as many individuals as possible with all ecological collembolan forms represented, we preferred to bury a triplet of subterranean pitfall traps into a single pit, being aware of possible variations in community structure within the studied forested scree slope.

In temperate regions, spring and autumn activity peaks occur in collembolans inhabiting leaf litter and

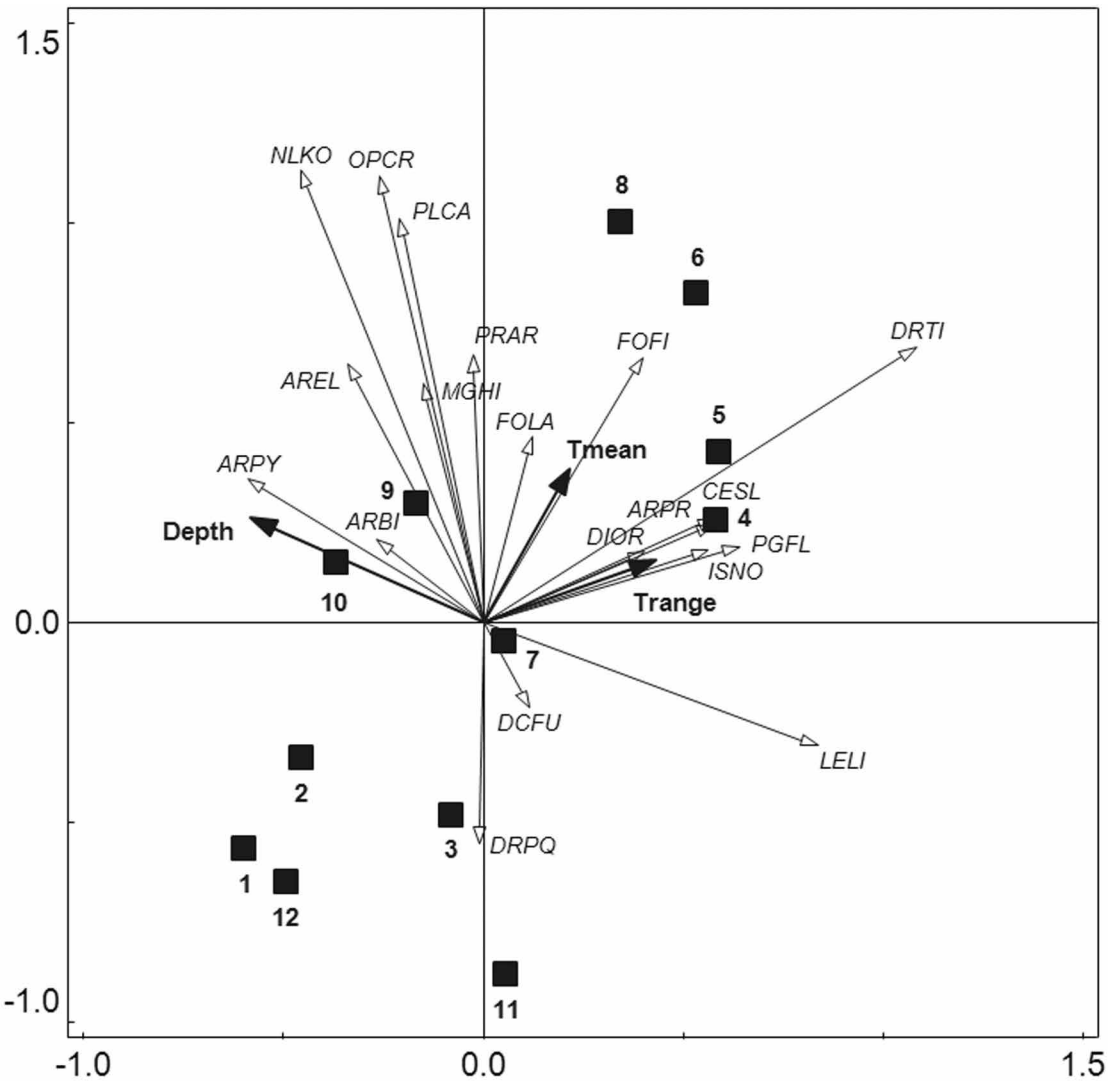

Figure 3. The RDA ordination biplot indicating associations of collembolan communities with months (black squares attended by Arabic numerals), depth, monthly temperature means (*Tmean*), and monthly temperature ranges (*Trange*). Collembolan species included in the analysis: Trogloxenes: DCFU – *Dicyrtoma fusca*, DIOR – *D. ornata*; Subtroglophiles: AREL – *Pygmarrhopalites elegans*, CESL – *Ceratophysella silvatica*, DRPQ – *Desoria propinqua* DRTI – *Desoria tigrina*, FOFI – *Folsomia fimetaria*, ISNO – *Parisotoma notabilis*, LELI – *Lepidocyrtus lignorum*, PGFL – *Pogonognathellus flavescens*; Eutroglophiles: ARBI – *Pygmarrhopalites bifidus*, ARPR – *Pygmarrhopalites principalis*, ARPY – *Pygmarrhopalites pygmaeus*, FOLA – *Folsomia lawrencei*, OPCR – *Oncopodura crassicornis*, PLCA – *Plutomurus carpaticus*, PRAR – *Protaphorura armata*; Troglobionts: MGHI – *Megalothorax hipmani*, NLKO – *Neelus koseli*.

underlying topsoil, which is largely related to the favourable microclimatic conditions (i.e. lower temperature values along with higher relative humidity) for oviposition and ensuing development of juveniles in these seasons (Coleman et al., 2017). A long-term decline in soil collembolans activity is evident in winter. In summer, the activity usually drops for a short period of time (Christiansen, 1964; Hopkin, 1997). In our study, such a pattern of seasonal activity dynamics continued from the topsoil to the deepest part of the scree slope profile and was more or less typical of all four ecological forms of Collembola. We support the findings of previous authors (Racovitza and Şerban, 1982; Crouau-Roy et al. 1992; Rendoš et al., 2012, Nitzu et al., 2014) that seasonal activity of invertebrates in shallow subterranean habitats is intensely affected by microclimatic fluctuations during the year. The most prominent activity peak was observed in subtroglophiles occupying the uppermost levels of the depth profile in spring due to a mass occurrence of juvenile stages of some species (especially *Desoria tigrina* and *Lepidocyrtus lignorum*). Typically, the increase in collembolan activity, regardless of the ecological form, was rather moderate within the scree slope. In deeper layers, the activity peaks tended to be long-term, i.e. they lasted for several consecutive months, which was presumably associated with a reduction of daily temperature fluctuations resulting in prolongation of microclimate suitable for collembolan development.

Some studies consider deep layers of screes to represent a seasonal refuge for some invertebrates seeking temporary shelter during adverse environmental conditions. Nitzu et al. (2014), for instance, reported several Collembola and Coleoptera species inhabiting the surface of loose screes stabilized by a tiny amount of soil to migrate vertically into the scree interior during summer heat. Similarly, Polak (2012) observed subterranean coleopterans inhabiting an ice cave migrating into the adjacent MSS to avoid temperatures below the freezing point, which tend to occur in this cave during winter. In both cases, the authors found communities of subterranean and soil-dwelling species to overlap within the MSS. In our study, no species migration was recorded. Furthermore, our results suggest a strong spatial

separation of troglobiont and trogloxene activity all year round. While troglobionts were active predominantly at lower and thermally more stable layers of the depth profile characterized by negligible fluctuations of daily temperatures, the second form was almost exclusively found in the uppermost layer possessing the most variable temperature parameters among all the investigated depths. Eutroglophiles as well as subtroglophiles were distributed along the entire depth profile throughout the year. This pattern of seasonal activity of Collembola ecological forms along the depth profile was presumably associated with the character of the scree slope site. In this study, we investigated a scree slope stabilized with a relatively thick layer of soil and overgrown with dense forest. On such types of scree slopes, the treetops greatly dampen high summer temperatures, thus protecting the soil surface from overheating and subsequent drying. In winter, the scree surface seems to be influenced by warmer air deposited in the scree voids, which is consequently reflected in attenuation of low temperatures. We recorded slight short-term frost on the scree slope surface in winter, although the air temperature above the scree dropped deep below the freezing point in the long term (continuously less than −10 °C) in winter. Such thermal conditions seem to be favorable for all ecological forms of Collembola, and thus, none of them was forced to migrate into deeper layers of the scree slope profile.

The present study supported our hypotheses, and its results are consistent with observations from cave habitats that susceptibility to temperature fluctuations increases in proportion with degree of species affinity for subterranean environment (Tobin et al., 2013; Mammola et al., 2015; Raschmanová et al., 2018). Species limited to a subterranean environment are, in contrast to their soil-dwelling relatives, much more susceptible to desiccation due to the loss of most of the physiological mechanisms to control water balance. Since evaporation increases exponentially with rising temperature, subterranean species are considered to be capable of living exclusively within the areas with narrow temperature ranges (Peck, 1976; Howarth, 1980). The RDA analysis applied in this study revealed a general pattern of preferences of particular collembolan species to temperature parameters. Troglobionts and most eutroglophiles favored rather narrow temperature ranges deeper in the investigated scree slope profile in early autumn. On the contrary, trogloxenes and most subtroglophiles inclined to wider temperature ranges typical of upper parts of the scree profile during spring.

Conclusions

This study was focused on the activity dynamics of collembolan communities inhabiting the depth profile of a forested limestone scree slope — one of the most common types of terrestrial shallow subterranean habitats in temperate regions. During the year, fluctuations of activity dynamics were observed in all four ecological forms of Collembola and across the studied scree slope profile. Tolerance to temperature fluctuations decreases in proportion with the degree of affinity for subterranean environment. Subterranean species (troglobionts and eutroglophiles) tended to occupy deeper and thermally more stable parts of the depth profile, while soil-dwelling Collembola (trogloxenes and subtroglophiles) occurred mostly in the upper and thermally more variable parts of the depth profile. This study contributes to the general knowledge of invertebrate activity dynamics in forested scree slopes of the temperate zone.

Acknowledgements

This study was financially supported by grant 1/0346/18 from the Slovak Scientific Grant Agency Vega and by internal grant GaPU 21/2018 of the University of Prešov. We are very grateful to our colleagues and friends Michal Goga, Peter Ľuptáčik, Edita Maxinová, and Andrea Parimuchová for their kind assistance during the fieldwork and laboratory work. We thank the Slovak Hydrometeorological Institute for providing us with meteorological data for the study site. Our thanks also go to D. McLean for linguistic correction of the manuscript and to the two anonymous reviewers who helped improve early version of the manuscript.

References

Bretfeld, G., 1999, Symphypleona, *in* Dunger, W., ed., Synopses on Palaearctic Collembola, Part 2: Görlitz, Germany, Abhandlungen und Berichte des Naturkundemuseums, v. 71, p. 1–318.

Christiansen, K.A., 1964, Bionomics of Collembola: Annual Review of Entomology, v. 9, p. 147–178. https://doi.org/10.1146/annurev.en.09.010164.001051

Coleman, D., Callaham, M., and Crossley,D., 2017, Fundamentals of Soil Ecology: Cambridge, The United States of America, Academic Press, p. 376.

Crouau-Roy, B., Crouau, Y., and Ferre, C., 1992, Dynamic and temporal structure of the troglobitic beetle *Speonomus hydrophilus* (Coleoptera: Bathysciinae): Ecography, v. 15, p. 12–18. https://doi.org/10.1111/j.1600-0587.1992.tb00002.x

Culver, D.C., and Pipan, T., 2008, Superficial subterranean habitats – gateway to the subterranean realm?: Cave and Karst Science, v. 35, p. 5–12.

Culver, D.C., and Pipan, T., 2014, Shallow subterranean habitats: Ecology, Evolution and Conservation: Oxford, England, Oxford University Press, 304 p. https://doi.org/10.1093/acprof:oso/9780199646173.001.0001.

Deharveng, L, 2004, Insecta: Apterygota, in Gunn, J., ed., Encyclopedia of Caves and Karst Science: New York, The United States of America, Taylor and Francis, p. 962–964.

Giachino, P.M., and Vailati, D., 2010, The subterranean environment. Hypogean life, concepts and collecting techniques: Verona, Italy, World Biodiversity Association, WBA Handbooks, 132 p.

Gilgado, J.D., Ledesma, E., Cuesta, E., Arrechea, E., de la Vega, J.L.Z., Sánchez-Ruiz, A., and Ortuño, V.M., 2014, *Dima assoi* Perez Arcas 1872 (Coleoptera: Elateridae): from montane to hypogean life. An example of exaptations to the subterranean environment?: Annales de la Societe Entomologique de France, v. 50, p. 264–271. https://doi.org/10.1080/00379271.2014.981421

Hochmuth, Z., 2008, Krasové územia a jaskyne Slovenska: Geographia Cassoviensis, v. 2, p. 1–210.

Hopkin, S.P., 1997, Biology of the Springtails: (Insecta: Collembola): Oxford, England, Oxford University Press, 340 p.

Howarth, F.G., 1980, The zoogeography of specialized cave animals: a bioclimatic model: Evolution, v. 34, p. 394–406. https://doi.org/10.1111/j.1558-5646.1980.tb04827.x

IUSS Working Group WRB, 2015, World Reference Base for Soil Resources 2014, update 2015. International soil classification system for naming soils and creating legends for soil maps: Rome, Italy, World Soil Resources Reports No. 106. FAO, p. 192.

Jiménez-Valverde, A., Gilgado, J.D., Sendra, A., Pérez-Suaréz, G., Herrero-Borgoñón, J.J., and Ortuño, V.M., 2015, Exceptional invertebrate diversity in a scree slope in Eastern Spain: Journal ofInsect Conservation, v. 19, p. 713–728. https://doi: 10.1007/s10841-015-9794-1

Juberthie, C., 1983, Le milieu souterrain: Étendue et Composition: Mémoires de Biospéologie, v. 10, p.17–65.

Juberthie, C., 2000, The diversity of the karstic and pseudokarstic hypogean habitats in the world, *in* Wilkens, H., Culver, D.C., and Humphreys, W.F., eds., Subterranean Ecosystems, Ecosystems of the World 30: Amsterdam, The Netherlands, Elsevier, p. 17–39.

Juberthie, C., and Decu, V., 2004, Interstitial habitats (terrestrial), *in* Gunn, J., ed., Encyclopedia of Caves and Karst Science: New York, The United States of America, Taylor and Francis, p. 984–986.

Juberthie, C., Delay, B., and Bouillon, M., 1980, Extension du milieu souterrain en zone non calcaire:description d'un nouveau milieu et de son peuplement par les Coléoptéres troglobies: Mémoires de Biospéologie, v. 7, p. 19–52.

Juberthie, C., Delay, B., and Bouillon, M., 1981, Extension du milieu souterrain superficiel en zone calcaire: Mémoires de Biospéologie, v. 8, p. 77–93.

Kováč, Ľ., 2000, A review of the distribution of cave Collembola (Hexapoda) in the Western Carpathians: Mémoires de Biospéologie, v. 27, p. 71–76.

Kováč, Ľ., and Papáč, V., 2010, Revision of the genus *Neelus* Folsom, 1896 (Collembola, Neelida) with the description of two new troglobiotic species from Europe: Zootaxa, v. 2663, p. 36–52. http://dx.doi.org/10.11646/zootaxa.2663.1.2

Kováč, Ľ., Parimuchová, A., and Miklisová, D., 2016, Distributional patterns of cave Collembola (Hexapoda) in association with habitat conditions, geography and subterranean refugia in the Western Carpathians: Biological Journal of the Linnean Society, v. 119, p. 571–592. https://doi.org/10.1111/bij.12555

Laška, V., Kopecký, O., Růžička, V., Mikula, J., Véle, A., Šarapatka, B., and Tuf, I. H., 2011, Vertical distribution of spiders in soil: The Journal of Arachnology, v. 39, p. 393–398. https://doi.org/10.1636/P09-75.1

Mammola, S., Giachino, P.M., Piano, E., Jones, A., Barberis, M., Badino, G., and Isaia, M., 2016, Ecology and sampling techniques of an understudied subterranean habitat: the *Milieu Souterrain Superficiel* (MSS): The Science of Nature, v. 103, p. 88. https://doi.org/10.1007/s00114-016-1413-9

Mammola, S., Piano, E., Giachino, P.M., and Isaia, M., 2015, Seasonal dynamics and micro-climatic preference of two Alpine endemic hypogean beetles: International Journal of Speleology, v. 44, p. 239–249. http://dx.doi.org/10.5038/1827-806X.44.3.3

Mammola, S., Piano, E., Giachino, P.M., and Isaia, M., 2017, An ecological survey of the invertebrate community at the epigean/hypogean interface: Subterranean Biology, v. 24, p. 27–52. https://doi.org/10.3897/subtbiol.24.21585

Mock, A., and Tajovský, K., 2008, *Mecogonopodium carpathicum* n. sp. (Diplopoda: Chordeumatida: Attemsiidae), a new troglophilic millipede from Slovakia: Zootaxa, v. 1778, p. 26–36. https://doi: 10.5281/zenodo.182245

Mock, A., Šašková, T., Raschmanová, N., Jászay, T., Ľuptáčik, P., Rendoš, M., Tajovský, K., and Jászayová, A., 2015, An introductory study of subterranean communities of invertebrates in forested talus habitats in southern Slovakia: Acta Societatis Zoologicae Bohemicae, v. 79, p. 243–256.

Nitzu, E., Nae, A., Băncilă, R., Popa, I., Giurginca, A., and Plăiaşu, R., 2014, Scree habitats: ecological function, species conservation and vertical-temporal variation in the arthropod community: Systematics and Biodiversity, v. 12, p. 65–75. https://doi.org/10.1080/14772000.2013.878766

Nitzu, E., Nae, A., and Popa, I., 2006–2007, Eco-faunistic study on the invertebrate fauna (Araneae, Collembola and Coleoptera) from the Vârghiş Gorge Natural Reserve (Eastern Carpathians, Romania), with special note on the micro-refugial role of the subterranean habitats: Travaux du Muséum National d'Histoire Naturelle "Grigore Antipa", v. 45–46, p. 31–50.

Peck, S.B., 1976, The effect of cave entrances on the distribution of cave-inhabiting terrestrial arthropods: International Journal of Speleology, v. 8, p. 209–321. http://dx.doi.org/10.5038/1827-806X.8.4.1

Pipan, T., López, H., Oromí, P., Polak, S., and Culver, D.C., 2010, Temperature variation and the presence of troglobionts in terrestrial shallow subterranean habitats: Journal of Natural History, v. 45, p. 253–273. https://doi.org/10.1080/00222933.2010.523797

Polak, S., 2012, Vertical migration of the subterranean beetles as a respond to annual temperature fluctuations: 21th International Conference on Subterranean Biology, 2–7 September 2012, Košice, Slovakia , Pavol Jozef Šafárik University in Košice, p. 92

Pomorski, R.J., 1998, Onychiurinae of Poland (Collembola: Onychiuridae): Wrocław, Poland, Polish Taxonomical Society, 201 p.

Potapov, M.B., 2001, Isotomidae: *in* Dunger, W., ed., Synopses on Palaearctic Collembola, Part. 3: Görlitz, Germany, Abhandlungen und Berichte des Naturkundemuseums, v. 73, p. 1–603.

Racovitza, G., and Şerban, M., 1982, Recherches sur la dynamique de la faune du milieu souterrain superficiel: Travaux du Museum d'Histoire Naturelle "Grigore Antipa", v. 24, p. 33–42.

Raschmanová, N., Šustr, V., Kováč, Ľ., Parimuchová, A., and Devetter, M., 2018, Testing the climatic variability hypothesis in edaphic and subterranean Collembola (Hexapoda): Journal of Thermal Biology, v. 78, p. 391–400. https://doi.org/10.1016/j.jtherbio.2018.11.004

Rendoš, M., Mock, A., and Jászay, T., 2012, Spatial and temporal dynamics of invertebrates dwelling karstic mesovoid shallow substratum of NNR Sivec (Slovakia), with emphasis on Coleoptera: Biologi,: v. 67, p. 1143–1151. https://doi.org/10.2478/s11756-012-0113-y

Rendoš, M., Raschmanová, N., Kováč, Ľ., Miklisová, D., Mock, A., and Ľuptáčik, P., 2016, Organic carbon content and temperature as substantial factors affecting diversity and vertical distribution of Collembola on forested scree slopes: European Journal of Soil Biology, v. 75, p. 180–187. https://doi.org/10.1016/j.ejsobi.2016.06.001

Rusek, J., 1975, Eine Präparationstechnik für Sprungschwänze und ähnliche Gliederfüsser: Mikrokosmos, v.12, p. 376–381.

Růžička, V., and Dolanský, J., 2016, Catching of spiders in shallow subterranean habitats in the Czech Republic: Arachnologische Mitteilungen, v. 51, p. 43–48. https://doi:10.5431/aramit5106

Růžička, V., and Kimeš, L., 2005, Spiders (Araneae) communities of scree slopes in the Czech Republic: The Journal of Arachnology, v. 33, p. 280–289. https://doi.org/10.1636/04-44.1

Schlick-Steiner, B.C., and Steiner, F.M., 2000, Eine neue Subterranfalle and Fänge aus Kärnten: Carinthia II, v. 190, p. 475–482.

Sket, B., 2008, Can we agree on an ecological classification of subterranean animals?: Journal of Natural History, v. 42, p. 1549–1563. https://doi.org/10.1080/00222930801995762

Ter Braak, C.J.F., and Šmilauer, S., 2012, Canoco reference manual and user's guide: software for ordination, version 5.0: Ithaca, U.S.A., Microcomputer Power, 496 p.

Thibaud, J.M., Schulz, H.J., and Gama, M.M., 2004, Hypogastruridae, *in* Dunger, W., ed., Synopses on Palaearctic Collembola, Part 4: Görlitz, Germany, Abhandlungen und Berichte des Naturkundemuseums, v. 75: p. 1–287.

Tobin, B.W., Hutchins, B.T., and Schwartz, B.F., 2013, Spatial and temporal changes in invertebrate assemblages structure from the entrance to deep-cave zone of a temperate marble cave: International Journal of Speleology, v. 42, p. 203–214. http://dx.doi.org/10.5038/1827-806X.42.3.4

Zacharda, M., Gunde, M., and Růžička, V., 2007, Thermal regime of three low elevation scree slopes in Central Europe: Permafrost and Periglacial Processes, v. 18, p. 301–308. https://doi.org/10.1002/ppp.598.

Appendix 1. Values of monthly minimum (Min) and maximum (Max) collembolan activities (calculated per 30 days) and species numbers recorded during the year in individual subterranean pitfal traps.

Depth, cm	Activity						Species Number					
	Trap 1		Trap 2		Trap 3		Trap 1		Trap 2		Trap 3	
	Min	Max	Min	Max	Min	Max	Min	Max	Min	Max	Min	Max
5	3.2	657.1	33.9	1234.5	21.4	2376.4	2	22	2	20	4	21
15	2.1	107.3	1.0	256.4	9.6	384.5	1	8	1	7	1	8
25	1.1	30.0	1.7	35.8	1.0	61.0	1	6	1	10	1	7
35	1.0	18.4	1.1	18.2	0.9	16.5	1	5	1	6	1	5
45	0.9	29.1	0.9	43.6	1.0	26.3	1	8	1	8	1	6
55	1.7	30.9	0.9	38.4	0.7	26.1	1	6	1	8	1	5
65	1.1	62.7	1.1	52.7	1.4	20.9	1	9	1	11	2	6
75	1.0	35.5	0.9	40.0	1.1	24.5	1	7	1	10	1	6
85	0.7	26.4	1.1	16.4	1.7	59.1	1	6	1	7	1	7
95	1.0	20.9	0.9	18.2	2.9	59.1	1	8	1	9	2	8

Bianca Burke, Adrian Slee, Peter D. McIntosh, Harald Hofmann, and James Shulmeister. A reactivated cave system induces rapidly developing cover-collapse sinkholes in Tasmania, Australia. *Journal of Cave and Karst Studies*, v. 82, no. 1, p. 31-50. DOI:10.4311/2019ES0109

A REACTIVATED CAVE SYSTEM INDUCES RAPIDLY DEVELOPING COVER-COLLAPSE SINKHOLES IN TASMANIA, AUSTRALIA

Bianca Burke[1], Adrian Slee[2], Peter D. McIntosh[2,C], Harald Hofmann[1], and James Shulmeister[1]

Abstract

The reasons of rapid development of cover-collapse sinkholes near Railton, Tasmania were investigated after sinkholes first appeared in a mature pine plantation in 2011. Sinkhole monitoring, dye tracing, chemical analyses of stream water and field observations indicated that large sinkholes in Quaternary alluvium overlying Ordovician limestone resulted from deepening of a limestone quarry south of the plantation. Intersection of a cave system during quarrying lowered the local water table, initiated streamsinks, and caused streams that previously flowed north towards the Mersey River to flow south to the quarry, via streamsinks and reactivated subsurface channels. Concurrently, the thickness of the vadose zone in thick Quaternary sediments overlying the limestone increased, hydraulic support for the sediments decreased, and numerous cover-collapse sinkholes formed. Chemical data including isotope analyses confirmed that the local aquifer is mainly recharged after high winter rainfall during high stream flow, when a proportion of the water in surface streams also flows directly northwards to the Mersey River. During low (summer) flow most water in surface streams flows into streamsinks and south into the quarry via the cave system. It is then pumped to a surface stream running north through the area in question, returns into the cave system via streamsinks and sinkholes, and finally returns to the quarry. The study demonstrates that water-table lowering by quarrying in limestone is not confined to cones of depression but may extend for kilometres if relict subsurface stream channels are intersected. In this area, the rapid development of cover-collapse sinkholes presents risks to infrastructure (a railway line, an electricity transmission line, and roads); to stream biodiversity because of altered water flow duration and water quality; to the safety of forest contractors, particularly those using heavy machines; and to the future use of presently productive land for economic return.

Introduction

The hazards associated with karst landforms are widely recognized (Langer, 2001; Bonacci, 2004; Cooper et al., 2011; Gutiérrez et al., 2014; Parise, 2015; Siska et al., 2016). The chief hazard evoked by karst processes is collapse of sinkholes, generally a natural process that occurs as a result of loss of surface strength by the enlargement of karst voids. Collapse sinkholes can be subdivided into those associated with cave roof collapse and those associated with collapse of thick overburden deposits mantling karst; the latter are called cover-collapse sinkholes (Kiernan, 2002; Gutiérrez et al., 2014).

Both sinkhole types develop by subsurface processes. Consequently, collapse can be difficult to predict. Before surface collapse occurs, karst voids in limestone bedrock may enlarge and cause erosion of sediment from the base of overlying overburden deposits, so that voids gradually extend towards the surface (Augarde et al., 2003; Kaufmann and Romanov, 2016; Jia et al., 2018). Eventually a void may become so big that the roof of the void cannot support itself and the ground surface suddenly collapses into a vertical or steep-walled sinkhole (Cooley, 2002). Overburden composed of layers of varying mechanical strength is particularly susceptible to collapse (Al-Halbouni et al., 2018). Laboratory simulations of this process have been detailed by Soliman et al. (2018). Once a collapse sinkhole has formed, continued vertical or horizontal development depends on the capacity of the underlying karstic voids to remove the collapsed material by suffusion. If the underlying voids are small, debris may block the karst cavities and sinkhole development may slow. However, if the voids are large and connected and the cover material is clay-rich and mobile, the sinkhole will continue to develop, particularly during high rainfall: suffusion processes will initially act on the collapsed material and later on the walls of the sinkhole, leading to sinkhole enlargement, so that over time the cover-collapse sinkhole changes from a vertical-sided hole to a cone (Calligaris et al. 2017; Lipar et al., 2019).

A notable example of a bedrock-collapse sinkhole was one which consumed a number of cars in a car museum in Kentucky, USA (Polk et al., 2015). Unbeknownst to the museum, its showroom was built on top of a large cave developed in limestone. By natural processes the roof of this cave had become almost too thin to support its weight and the added weight of the cars initiated its collapse. Although final collapse may be catastrophic, such roof-collapse sinkholes generally develop slowly, an example being the development of sinkholes overlying caves in the Stockyard Gully karst of Western Australia (Lipar et al., 2019). In contrast, cover-collapse sinkholes can develop rapidly and may not overlie a

[1] School of Earth and Environmental Sciences, University of Queensland, St Lucia 4072, QLD, Australia
[2] Forest Practices Authority, 30 Patrick Street, Hobart 7000, TAS, Australia
[C] Corresponding Author: peter.mcintosh@fpa.tas.gov.au

large cave. They may form during floods (Zhou and Lei, 2018) during which water flow and transport capacity in karstic voids may reach a maximum, or after groundwater extraction (Heidari et al., 2011; Khanlari et al., 2012). Water under pressure may liquify clay in overburden deposits above the karst contact, thereby undercutting the ground surface until roof failure occurs (Jia et al., 2018; Soliman et al. 2018). Examples of cover-collapse sinkholes forming rapidly after heavy rain have been documented in Europe (Gutiérrez-Santolalla, 2005; Martinotti et al., 2017; Noury et al., 2018; Parise et al*.,* 2018), the US (Hyatt and Jacobs, 1996; Hunt et al., 2013), and in the Mole Creek karst of northern Tasmania (Slee et al., 2019).

There are also numerous documented examples of anthropogenic impacts triggering rapid development of cover-collapse sinkholes. A notable example is that presented by the draining of Victory Lake in Georgia (Jovanelly, 2014). This man-made recreational lake was entirely drained by the lowering of the groundwater table by limestone quarrying: as a result cover-collapse sinkholes formed beneath the lake bed and linked the water in the lake to an existing subsurface karst aquifer, which itself was connected to the quarry, causing the lake to drain overnight (Jovanelly, 2014). Similar aquifer drawdown impacts resulting from quarry and mine operations and aquifer over-exploitation have been described in Italy (Parise and Pascali, 2003; Dell'Aringa et al., 2014), China (Jia et al., 2018; Pan et al., 2018), Iran (Heidari et al., 2011; Khanlari et al., 2012) and Belgium (Kaufmann and Quinif, 2002), amongst numerous other examples of this phenomenon in the USA and elsewhere, as reviewed by Langer (2001, p. 15–30). If sinkholes and quarries are legally or illegally used to dispose of waste, then contamination of water supplies can occur (Delle Rose et al., 2007).

Globally, karst hazards have come under most scrutiny in urban or peri-urban environments close to housing or major infrastructure, where hazards like cover-collapse sinkholes pose substantial risk to structures and lives of residents, workers or travellers (Brinkmann et al., 2008). Careful planning can reduce risks, an example being the planning for urban expansion onto karst in the northern suburbs of Perth, Western Australia (Csaky, 2003), but, in general, laws and policy documents do not take into account the complexity and peculiarity of karst environments (LaMoreaux et al., 1997; Delle Rose et al., 2007).

Karst hazards in production forests generally receive less attention than those in urban or peri-urban areas. In Tasmania, karst underlain chiefly by Palaeozoic limestone and Proterozoic dolomite is extensive in forested terrain (Kiernan, 1989, 1995a, b) and commercial operations in these forests have the potential to affect karst values both by direct effects, such as physical damage to caves, and indirect effects, such as modification of surface and subsurface water quality and flow, which may affect stream biodiversity. Consequently, mapping of karst and the identification of potential hazards associated with forest operations have been important components of Tasmanian forest management since the 1980s (e.g., Jones et al., 1988; Eberhard, 1994, 1998; Kiernan, 1995a; Sharples, 2002). Prescriptions governing karst management were included in the Tasmania's first Forest Practices Code (Forest Practices Authority, 1987), since updated (Forest Practices Authority, 2015), which defines acceptable forest practices for the timber industry in the state.

Until 2011, it was considered that areas of active karst in Tasmania were well-known, the most obviously active areas being the Florentine and Tyenna valleys in the state's south and the Mole Creek area in the mid-northwest. In both these areas, maps of karst features have been prepared, many caves have been explored, and subsurface water flows monitored (Kiernan, 1995a, b; Eberhard, 1998). Other limestone or dolomite areas have received less attention. Relevant to the study described in this paper is that in 1961 karst pinnacles up to 30 m high overlain by Quaternary sediments were noted in the now disused Goliath quarry at Railton (Jennings, 1961) and in the 1970s and 1980s several karst sinkholes were documented in the Railton area (Matthews et al., 1983; Donaldson, 1984; Kiernan, 1995b, p. 181) and were related to water table lowering at the same quarry (Kiernan, 1995b, p. 182). In 2003, the Forest Practices Authority reported on cover-collapse sinkholes near the railway line north of Railton (N. Duhig, unpublished FPA report). Despite these signs of instability the Railton area was not considered to be susceptible to widespread karst development (Kiernan, 1995b; Eberhard, 2007) and a report investigating an alternative site for a proposed limestone quarry at Mt Cripps in northwest Tasmania (Grimes 1999) suggested quarrying at Railton would be environmentally less sensitive.

Recently, however, rapid development of large sinkholes in a *Pinus radiata* plantation north of Railton (Fig 1) has become a significant land management issue. In January 2011, a cover-collapse sinkhole 20 m diameter was noted in the southwest of the unharvested forest block, and by August 2011 it had expanded considerably. At this time, the sinkhole was considered to be an isolated occurrence and standard precautionary measures were applied: specifically, a no-machinery buffer zone around the sinkhole and re-location of a planned wood processing site (landing) from the vicinity of the sinkhole to elsewhere in the forest block. However, since harvest in 2012, many more sinkholes formed and it became clear that a comprehensive survey was required to assess risks and determine the causes of land instability.

This study was undertaken to record the evolution of the active karst landscape in the Railton Valley since 2011, relate sinkhole formation to surface and sub-surface flows, and attempt to identify why sinkholes have formed rapidly in a previously stable landscape.

Regional and Local Setting

The Railton Valley lies in the central north of Tasmania (Fig. 1) (41.31 ºS, 146.40 ºE). The valley is aligned approximately north–south and is a flat-floored depression about 20 km long and 3–6 km wide. The floor of the valley varies from 70 m above sea level (asl) in the south to 5 m asl in the north. The town of Railton lies in the southern part of the valley at an altitude of 65 m asl and the town of Latrobe and the Mersey River estuary lie at the north end of the valley. Immediately north of Railton is the Dulverton Pit (limestone quarry) and cement works operated by Cement Australia Pty Ltd (see Fig. 1).

The geology of the area was described by Jennings (1960) and McClenaghan (2003). The extensive Quaternary valley floor deposits are predominantly gravelly clays, assumed to have accumulated during the last glacial period or earlier when colluvial and alluvial processes were more active than at present (McIntosh et al., 2012). These sediments overlie a syncline with a north–south axis formed within Ordovician rocks, consisting of Gordon Group limestone overlying Moina Sandstone and Owen Conglomerate (which together form the Owen Group). The Badger Range (up to 548 m asl) west and south of the valley is formed by the resistant Owen Conglomerate. Bonneys Tier (up to 460 m asl) west and north of the valley consists of a Jurassic dolerite sill overlying subhorizontal Permian sedimentary rocks. The Dulverton hills (172 m asl) east of the valley are formed in Moina Sandstone. Because of lack of exposure, the Gordon

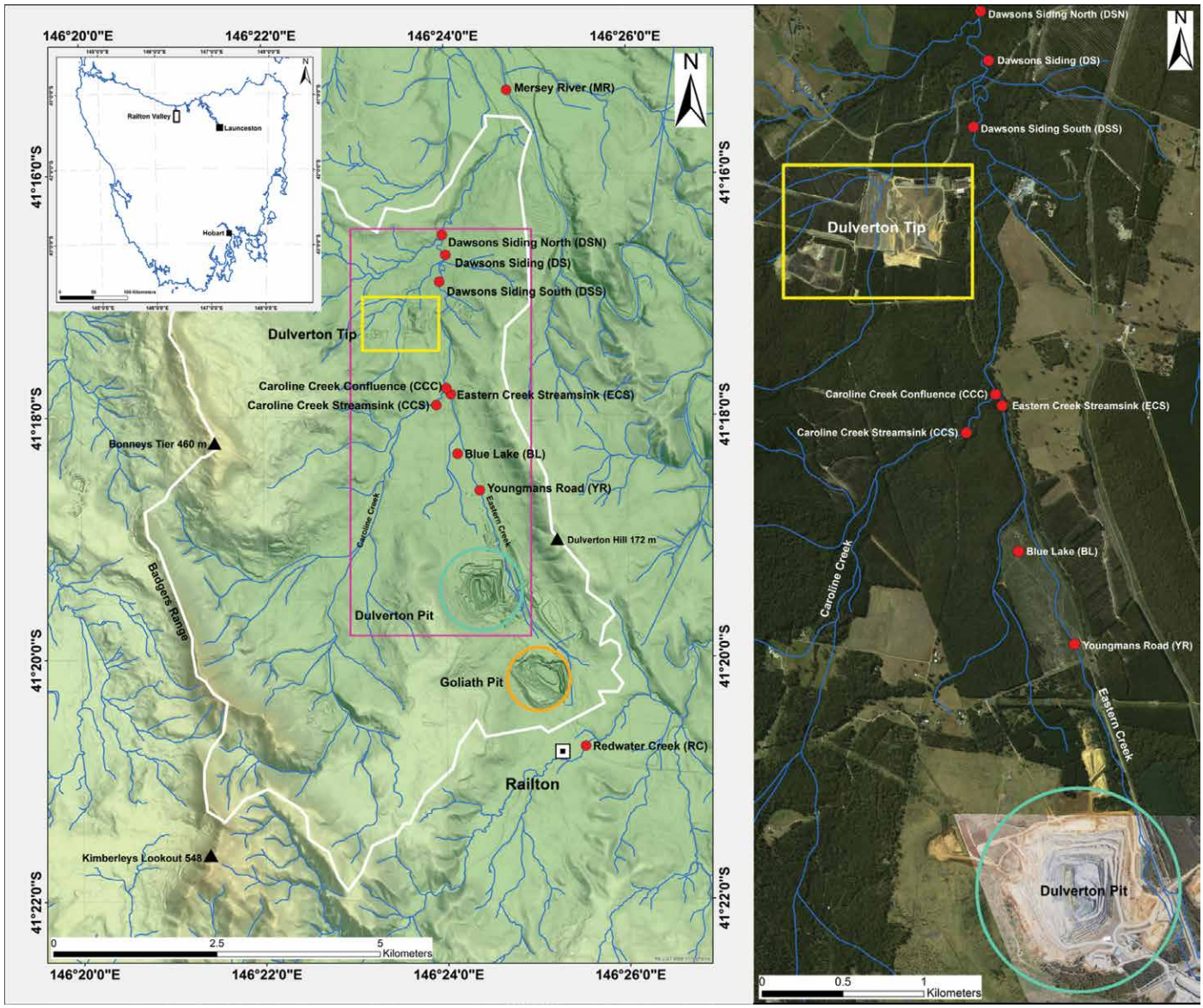

Figure 1. Left. General location map showing the Railton valley and the main topographic and drainage features of the study area. The locations indicated by red dots are karst sites at which experiments were conducted. The area of intensive study is outlined in pink. Right. Detail of intensive study area, showing sites at which experiments were conducted.

Group limestone has not been subdivided and mapped in the detail possible in other areas, where three formations have been identified (Brown et al., 1982). The limestone is up to 1000 m thick and contains about 88 % $CaCO_3$ and 5 % SiO_2 (Jennings, 1960). The limestone contact with overlying Quaternary deposits is highly irregular and in places consists of near-vertical limestone pinnacles 30 m high; in addition, gravelly cave fillings were observed in early quarries (Jennings, 1959, 1961). The deep relict karst features in the phreatic zone are likely to have been created during periods of lower sea level, as noted by Grimes (1994) for deep caves of South Australia. On the basis of the limestone's thickness, areal extent, and lack of lateral confinement along the syncline axis, the Railton karst is classified as 'deep-free flowing karst' (Grimes, 1999).

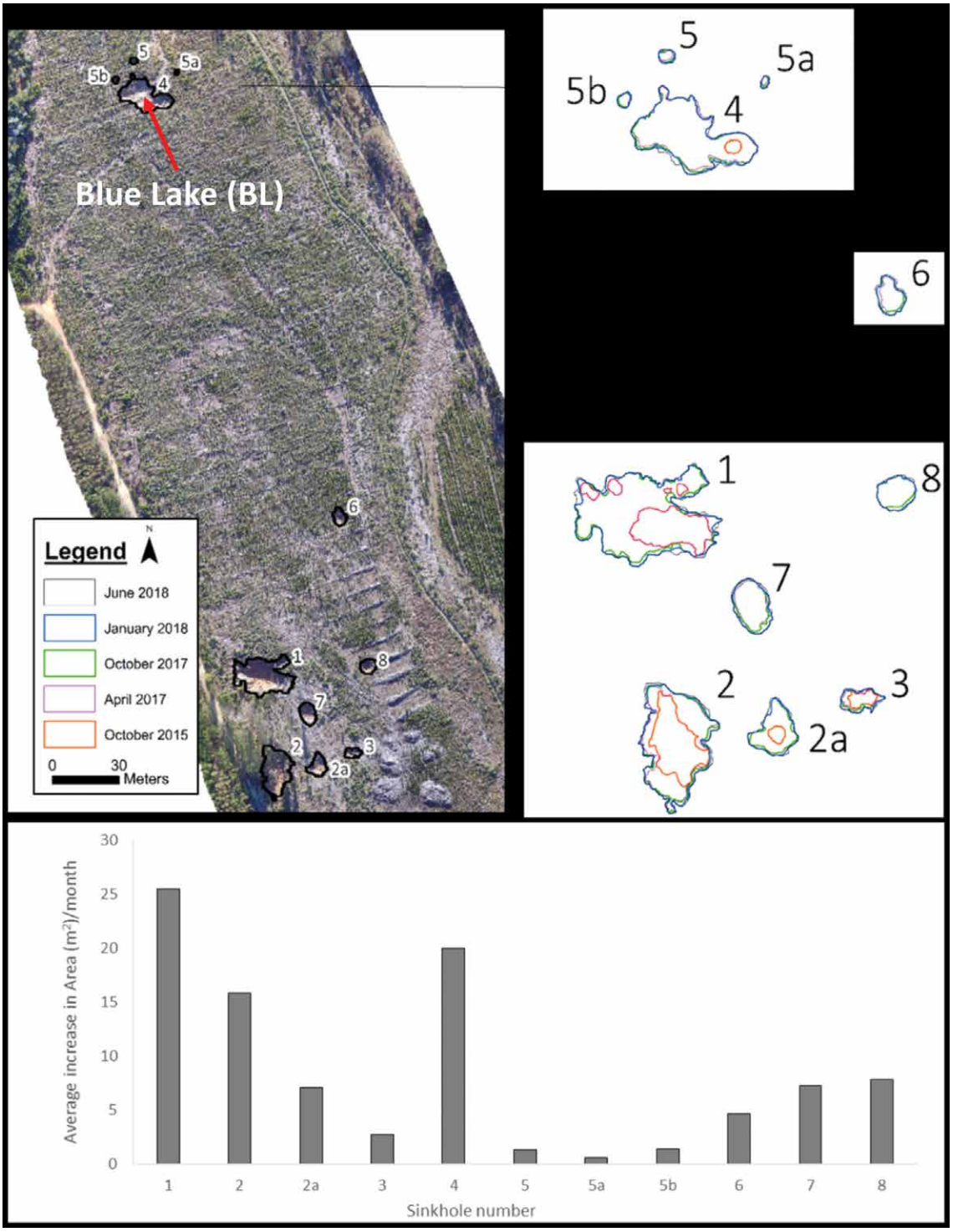

Figure 2. Sinkhole locations and development, October 2015 to June 2018. Blue Lake (Fig. 1) is arrowed for reference.

The southern end of the valley is drained by Redwater Creek that flows through the town of Railton and eastwards to the Mersey River (Fig. 1). The northern end of the valley and the plantation area is drained by Caroline Creek that has headwaters in the southwest of the valley. An unnamed stream running northwards from the limestone quarry (Dulverton Pit) on the eastern boundary of the plantation area that is the focus of this study is informally named Eastern Creek. It is largely a man-made channel and carries the drainage pumped from Dulverton Pit north to Caroline Creek. It is fabric-lined from Dulverton Pit to Youngmans Road (Fig. 1). Caroline Creek and its tributary Eastern Creek (Fig. 1) flow north to the Mersey River, which reaches the sea at Devonport, 25 km north of Railton.

Mean annual precipitation at Railton (Dowbiggin

St) is 1058 mm with a winter monthly maximum of 145 mm in July and a summer monthly minimum of 60 mm in January (Bureau of Meteorology, 2019). The mean monthly maximum and minimum temperatures at Sheffield, 9 km southwest of Railton are 22 ºC and 11 °C in January and 12 °C and 4 °C in June (Bureau of Meteorology 2019).

The valley has varied land use, including extensive areas of *Eucalyptus nitens* and *Pinus radiata* plantations managed by Forico Ltd., patches of native forest, small hobby farms primarily used for grazing, and limestone quarrying. Five kilometres north of Railton lies the Dulverton Tip, a major commercial waste solids and liquids disposal dump for northern Tasmania (Fig. 1).

Methods

To investigate the karst, we used combinations of field mapping, remote sensing, and hydrological and hydro-geochemical techniques. The project started in 2011 with observations and monitoring of sinkhole development. More intensive field mapping and hydrogeological investigations were carried out in 2017 and 2018.

Mapping And Monitoring

Documentation of the sinkholes and streamsinks present in the plantations north of Youngmans Road to began in early 2011. The first sinkhole documented (sinkhole 2, Fig. 2) was located in an unharvested *Pinus radiata* stand in 2011 and was mapped using a handheld GPS and a Leica Disto laser and compass. Between 2012 and 2014 development of sinkholes (including streamsinks) was monitored using a hand-held GPS and interpretation of photographic images (Fig. 2). In five surveys (in July 2015, October 2015, April 2017, October 2017 and January 2018) Forico Ltd employees mapped sinkhole extent using digital elevation models derived from high resolution imagery obtained from a DJI Phantom 4 drone equipped with a DJI FC330 camera. Each survey took on average 244 images with an average pixel size of 4.5 cm. Digital elevation models (DEMs) were extracted using the 'Maps Made Easy' software for each of the 2017 and 2018 surveys and resampled at 0.5 m, 1 m, and 3 m pixel sizes. Elevation data was not available for the 2015 survey. These images were supplemented by Google Earth Pro Imagery and the LiDar-derived shade maps of the area available on line at the List Tasmania website (www.thelist.com). Remote mapping was supplemented with field survey and ground-based photographs.

The semi-automated difference raster approach for defining sinkholes described by Doctor and Young (2013) was applied to ensure all sinkholes were identified, based on the assumption that depth values greater than 0.25 m were likely to indicate the presence of a sinkhole. Sinkhole boundaries were mapped in ArcMap v.10.5.10 by manual digitisation methods, aided by boundary enhancement using slope and curvature datasets. The evolution of sinkhole boundaries over 0.5, 1, 2, and 5 years was determined using Excel. For most sinkholes the exact date of initial collapse and significant enlargement was unable to be recorded, as neither foresters nor researchers were based close to the study site.

Although groundwater monitoring has been conducted in the area, the information is privately held and results were not available to the research team.

Stream Flow Measurements

Flow measurements in the two main streams (Caroline Creek and Eastern Creek) draining the northern end of the Railton Valley were recorded over a period of 6 months. Herron dipperlog NANO water pressure sensors (Heron Inc.) were positioned on stakes approximately 10 cm above the bottom of stream channels to measure water depths. The sensors were located at three sites on Caroline Creek: upstream of the main streamsink (CCS); at Eastern Creek upstream of its streamsinks (YR); and on the lower Caroline Creek at Dawsons Siding South (DSS) (Fig. 2). At these sites Hobo temperature loggers were also attached to the stakes to measure water temperature at half-hour intervals. Herron air pressure sensors were installed nearby so that water pressure measurements could be compensated for atmospheric pressure variation. At three logger locations (CCS, CCC and YR; Fig. 2) the channel cross sectional area was measured using the sag-tape surveying technique (Ray and Megahan, 1979) involving measuring channel depth from an established benchmark (bank-full height) at 20 cm intervals along a transect to calculate the cross-sectional area. We were unable to measure actual stream flow at different stream levels to produce a rating curve. Therefore, we applied the Manning equation (Marcus et al., 1992) to approximate flow rates at different stream levels. The calculated rates were verified using a digital flow meter (Hydro-Bios Digital Flow Meter) and by measuring the speed of a floating orange during site visits.

Autogenic recharge from point sources was determined from differential flow gauging similar to the method described by Scanlon et al. (2002), involving determining the difference in flow upstream and downstream of the recharge zone. Flow upstream was measured upstream of Eastern Creek Streamsink (ECS) and upstream of Caroline Creek Streamsink (CCS). Flow downstream was measured at Caroline Creek downstream of the Confluence (CCC) (Fig. 2). Autogenic recharge from point sources was determined using:

$$Q_{auto} = Q_{CCC} - (Q_{ECS} + Q_{CCS}), \quad (1)$$

where Q is discharge [L/T^3] and subscripts indicate sources as explained in the text above. Rainfall data were obtained for the station at Dowbiggin St, Railton, 4.55 km south of the study area (Bureau of Meteorology, 2019).

Dye-Tracing Experiments

Dye-tracing experiments are common practice in karst areas to trace groundwater flow through karst and to investigate the connections between sinkholes, streams, and groundwater or subsurface channels (Lauber et al., 2014; Frisbee et al., 2019). Within Tasmania dye-tracing experiments have been used primarily to prove connections between inaccessible reaches of cave systems, for example at Exit Cave (Kiernan, 1993; Osborne 1994) and Mole Creek (Kiernan, 1989, 1990; Kiernan et al., 1994) and in the Florentine Valley (Eberhard, 1998; Sharples, 2018). However, elsewhere dye tracing has been used in a broader range of karst and non-karst groundwater studies including the tracing of vadose zone karst water dispersal (Poulain et al., 2018) and the tracing of water drainage through sub-glacial meltwater channels (Flett et al., 2017; Miles et al., 2019).

Streamsinks were located early in this study, but no accessible caves were found and flow directions within the underlying karst were unknown. For this reason, four dye tracing experiments (Table 1) were undertaken to identify flow pathways during low and high stream flows. The first experiment was conducted in July 2017 (winter). The second was in January 2018 (summer). The third and fourth were conducted in July 2018 (winter). Experiments 3 and 4 included assessments of flow velocities.

Cumulative dye concentrations measured in charcoal bags retrieved from sampling sites (Fig. 1) were normalized (NC-ppb) by dye injection concentrations so that direct comparisons between dye-tracing experiments could be made. Normalized cumulative values were determined by dividing the received dye concentrations by the input dye concentration, to allow received concentration values to be directly compared between experiments (Goldscheider et al*.,* 2008). For all four experiments (Table 1) activated charcoal bags were sampled at each site before dye injection to detect any background dye pollution in the water.

The aim of Experiment 1 was to determine whether water flowing into Caroline Creek Streamsink (CCS) at low flow flowed north (to the lower reaches of Caroline Creek) or south (to the upper reach of Eastern Creek). The aim of Experiment 2 was to determine whether water flowing into Eastern Creek Streamsinks (ECS) at low flow flowed north (to the lower reaches of Caroline Creek or the Mersey River) or south (to the upper reach of Eastern Creek or Redwater Creek). The aim of Experiment 3 was to determine whether water flowing into Blue Lake (BL) at high flow flowed north (to the lower reaches of Caroline Creek) or south (to the upper reach of Eastern Creek or Redwater Creek). The aim of Experiment 4 was to determine whether water flowing into Caroline Creek Streamsink (CCS) at high flow flowed north (to the lower reaches of Caroline Creek) or south (to the upper reach of Eastern Creek or Redwater Creek) and to establish flow rates by accurate timing of dye arrival using a fluorimeter.

Fluorescein (green) and Rhodamine WT (red) were used as tracing dyes. Dye-tracing experiments used activated charcoal bags installed and removed from streams to establish subsurface flow pathways. After their removal from streams, bags were sent to Ozark Underground Laboratory, USA for dye analysis. For the third and fourth experiments, two Turner Cyclops C7 Fluorimeters were set up in Eastern Creek near Youngmans Road (YR) and at Caroline Creek at Dawsons Siding North (DSN). Charcoal bags were also used. The loggers were set up to record fluorescence at 1-min intervals over 178 h (7.5 days) beginning on July 27, 2018. Unfortunately, although the fluorimeter at DSN returned a complete dataset, the YR instrument malfunctioned.

Water Chemistry

Water was sampled for major ion chemistry and stable isotope analysis to supplement the dye-tracing experiments. The first water sampling was during low flow and was undertaken on January 16, 2018. Three days before water sample collection 8 mm of rainfall was recorded and no rainfall occurred during sampling. Sampling was undertaken at YR, DS, RC and MR (Fig. 1). Water was collected from streams in rinsed 250 mL bottles for

Table 1. Details of the four dye-tracing experiments.

Experiment	Location of dye injection[a]	Site Code[a]	Field notes	Date	Dye used	Amount, g	Location of charcoal bags and/or fluorometera,[b]
1	Caroline Creek Streamsink	CCS	Low Flow	June 7, 2017	Fluorescein	410	YR, DS
2	Eastern Creek Streamsink	ECS	Low Flow	Jan. 16, 2018	Fluorescein	454	YR, DS, RC, MR
3	Blue Lake	BL	High Flow	July 26, 2018	Rhodamine WT	907	YR, DSN, RC
4	Caroline Creek Streamsink	CCS	High Flow	July 27, 2018	Fluorescein	907	YR, DSN, RC

[a] For site locations see Figure 1.
[b] YR = Youngmans Road; DS = Dawsons Siding; DSN = Dawsons Siding North; BL = Blue Lake; RC = Redwater Creek; MR = Mersey River

major ions and 125 mL bottles for stable isotopes, ensuring no air was trapped in the bottles. Samples for major ion analysis were filtered with 0.45 µm filters and stored at ~2 °C before being analysed. *In situ* measurements for electrical conductivity (EC), dissolved oxygen (DO), pH and temperature (°C) were taken concurrently using ProDSS water-parameter water quality meters. Stable isotope values (δ^2H and $\delta^{18}O$) in rainfall were approximated from the Global Network of Isotopes in Precipitation (GNIP) archives for Cape Grim, Tasmania (GNIP 2018). The second water sampling was during high flow and was undertaken on January 25, 2018 at YR and DSN, on January 26 at CCS and ECS and on January 29 at five northern streams (not shown in Fig. 1). 29.4 mm of rain fell on January 24, 2018, 18.2 mm on January 25, 2018, no rain fell January 26–28, 2018 and 19 mm fell on January 29, 2018.

Chemical analyses followed the methods of Baublys et al. (2015) and Filippini et al. (2018) and were conducted at the School of Earth and Environmental Sciences at the University of Queensland. Major anions were measured by ion chromatography (IC) using a Dionx ICS 1100 instrument. Samples for major cation analysis were acidified with 70 % HNO_3 and cations were measured using ICP OES (Inductively Coupled Plasma Optical Emission Spectrometry). The precision for major ion concentrations was calculated from replicate samples and was ±2 %. Bicarbonate (HCO_3^-) and carbon dioxide (CO_2) concentrations were determined by pH titration both in the field and in the laboratory, within 7 days of sample collection. A Hatch Digital Titrator with an accuracy of ±1 % was used. Titration results expressed in HCO_3 of $CaCO_3$ were converted to HCO_3^- concentrations using the stoichiometric multiplication factor of 1.22.

Water-stable isotopes of $\delta^{18}O$ and δ^2H were analysed in the stable isotope laboratory at the University of Queensland (UQ-SIGL) following methods used by Baublys et al. (2015). An Isoprime dual inlet isotope mass spectrometer was used with an accuracy of ±0.08 per mL for ^{18}O and ±1.0 per mL for ^2H. δ^2H values were analysed after online equilibration at 40 °C with Hokko coils. $\delta^{18}O$ values were analysed after equilibration with carbon dioxide. δ^2H and $\delta^{18}O$ values in VSMOW ‰ were normalized to standard mean ocean water (VSMOW-SLAP), following a 3-point normalization based on replicate analyses with international standards USGS45 and USGS46. All laboratory standards were calibrated against IAEA (VSMOW, SLAP, GISP). Accuracy and precision were better than ±1 ‰ for δ^2H and ±0.05 ‰ for $\delta^{18}O$ at 1σ. $\delta^{13}C$-DIC was analysed by a Thermo Delta V continuous-flow isotope ratio mass spectrometer (CF-IRMS) coupled to a Gas Bench II. $\delta^{13}C$-DIC values were normalized to the VPDB % scale using international standards NBS19 and LSVEC via two-point normalization.

Figure 3. Sinkhole 1 in March 2019. This sinkhole formed in the winter of 2016 when several smaller sinkholes formed in 2013–2015 coalesced. It is the largest in the study area at over 60 m wide and 10 m deep with a footprint of 1450 m^2. An estimated 6000 m^3 of soil derived from Quaternary deposits have been lost to the underlying karst at this site. The furthest figure is standing on an exposure of limestone bedrock with a small cave entrance into which runoff flows during heavy rainfall.

Results

Field Surveys and Sinkhole Monitoring

Mapped sinkholes are shown in Fig. 2. The first sinkhole noted (sinkhole 2; Fig. 2) formed before harvest operations. At the time of first inspection in January 2011, it was approximately 20 m diameter and 4 m deep. By August 2011, it had expanded to 27 m diameter and 7 m deep. Between January 2011 and July 2018 14 sinkholes formed in the study area, including Sinkhole 1 (Fig. 3) and Sinkhole 3 (Fig. 4) that formed catastrophically over a weekend in 2013. Since 2016, there has been a rapid increase in sinkhole numbers with a second sinkhole cluster forming at the northern end of the plantation (Fig. 2), as well as several isolated features. As previously mentioned, the date of initial collapse of most sinkholes in the study area is unknown. The sinkholes that have formed since 2016 appear to have collapsed during the winter months of May–

Figure 4. A contractor standing on the edge of a sinkhole (the precursor to sinkhole 3, Fig. 2), which formed between the close of the week's work on Friday April 19, 2013 and the return of contractors on Monday April 22, 2013. The contractor is standing on vehicle tracks — a harvesting machine had crossed the area of the sinkhole on the previous Friday.

August. During heavy rain in July 2017 rapid lateral sinkhole expansion of sinkhole 2 by gully erosion and slumping was observed indicating that it is likely that most sinkhole expansion follows wet weather. Between June 2015 and July 2018 all sinkholes expanded and new sinkholes formed (Fig. 2). Although cave entrances were noted during surveys, specifically at Caroline Creek Streamsink (CCS) and in Blue Lake (BL) when dry, the hazard of overburden collapse prevented any cave exploration.

Flow And Rainfall

Flow calculations using Manning's equation were compared to flow measured *in situ*. Estimated flows at CCS exceeded measured flows by 14 %, were lower than measured flows at ECS by 4 % and were lower than measured flows at CCC by 15 % (i.e., the two techniques produced results within 15 % of each other).

The streams at CCS, ECS and CCC have different seasonal behaviour (Fig. 5). The flow in Caroline Creek at CCS is seasonally variable ($\mu = 0.46$, $\sigma = 0.45$ m/s): large flow peaks follow high rainfall and there is a gradual increase in total flow as winter progresses (Fig. 5). From June to July average flow increased by 1.27 $m^3\ s^{-1}$ relative to the January–April average of 0.2 $m^3\ s^{-1}$. In summer Caroline Creek is generally dry. Eastern Creek flows continuously (Fig. 5). At ECS Eastern Creek has relatively consistent diurnal flow peaks and troughs measured from January to April ($\mu = 0.57$, $\sigma = 0.10$ $m^3\ s^{-1}$), probably related to pumping cycles at the nearby limestone

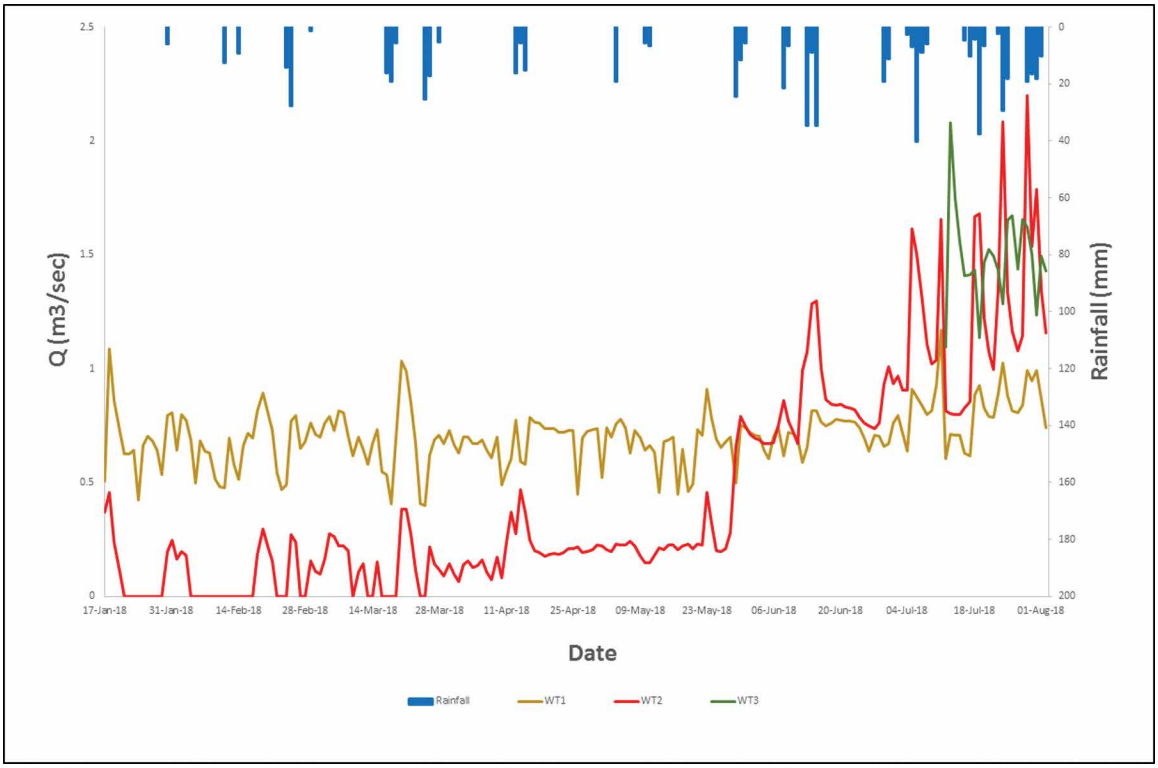

Figure 5. Flow records for Eastern Creek at ECS (brown line), Caroline Creek at CCS (red line) and Caroline Creek at DSS (green line), January 17, 2018 to July 31, 2018. Note the relatively uniform flow of Eastern Creek and the seasonal flow of Caroline Creek. Daily rainfall (mm) shown as blue bars.

quarry; from June to July maximum flow increased only by 0.15 $m^3 s^{-1}$ relative to the January–April average. High flow of Eastern Creek during periods of higher rainfall (May–July) matches that of Caroline Creek (Fig. 5).

Dye-Tracing Results

No background dye was detected in any stream prior to dye-tracing experiments.

Experiment 1

Fluorescein dye was injected into Caroline Creek at Caroline Creek Streamsink (CCS) on June 7, 2017 during low flow (defined as occurring when all of the flow of Caroline Creek enters Caroline Creek Streamsink and no flow continues overland). Charcoal bags were collected after 2 days and 7 days immersion. Dye was detected at both Youngmans Road (YR) and at Dawsons Siding (DS) (Fig. 6, Experiment 1). Flow rates were not recorded during this initial experiment but dye arrived at YR and DS in less than 48 h. Higher dye concentrations were recorded at YR (0.16 NC-ppb) than at DS (0.0048 ppb). The experiment showed that a subsurface connection exists between the Caroline Creek Streamsink (CCS) and the upper reaches of Eastern Creek (YR).

Experiment 2

Fluorescein dye was injected upstream of Eastern Creek Streamsinks (ECS) on January 16, 2018 during low flow when some water was flowing north in the surface channel and some was sinking into Eastern Creek Streamsinks (ECS). Charcoal bags were collected at the following times after injection: Mersey River (MR) 18 and 162 h; Dawsons Siding (DS) 3, 18, 65 and 162 h; Youngmans Road (YR) 4, 18, 42, 65 and 162 h; and Redwater Creek (RC) 66 and 161 h. Dye was detected at both Eastern Creek at Youngmans Road (YR) and Caroline Creek at Dawsons Siding (DS). Flow in Eastern Creek at ECS was recorded as approximately 0.41 $m^3 s^{-1}$. Dye arrived at YR in under 18 h and at DS between 6 and 18 h. Higher concentrations of dye were recorded at DS (2.174 NC-ppb) than at YR (0.033 NC-ppb) (Fig. 6, Experiment 2). Small concentrations of fluorescein were recorded in the Mersey River (MR) (0.006 NC-ppb) and no dye was recorded at Redwater Creek (RC). The experiment showed that a subsurface connection exists between the Eastern Creek Streamsinks (ECS) and the upper reaches of Eastern Creek (YR) but no connection exists between ECS and Redwater Creek (RC).

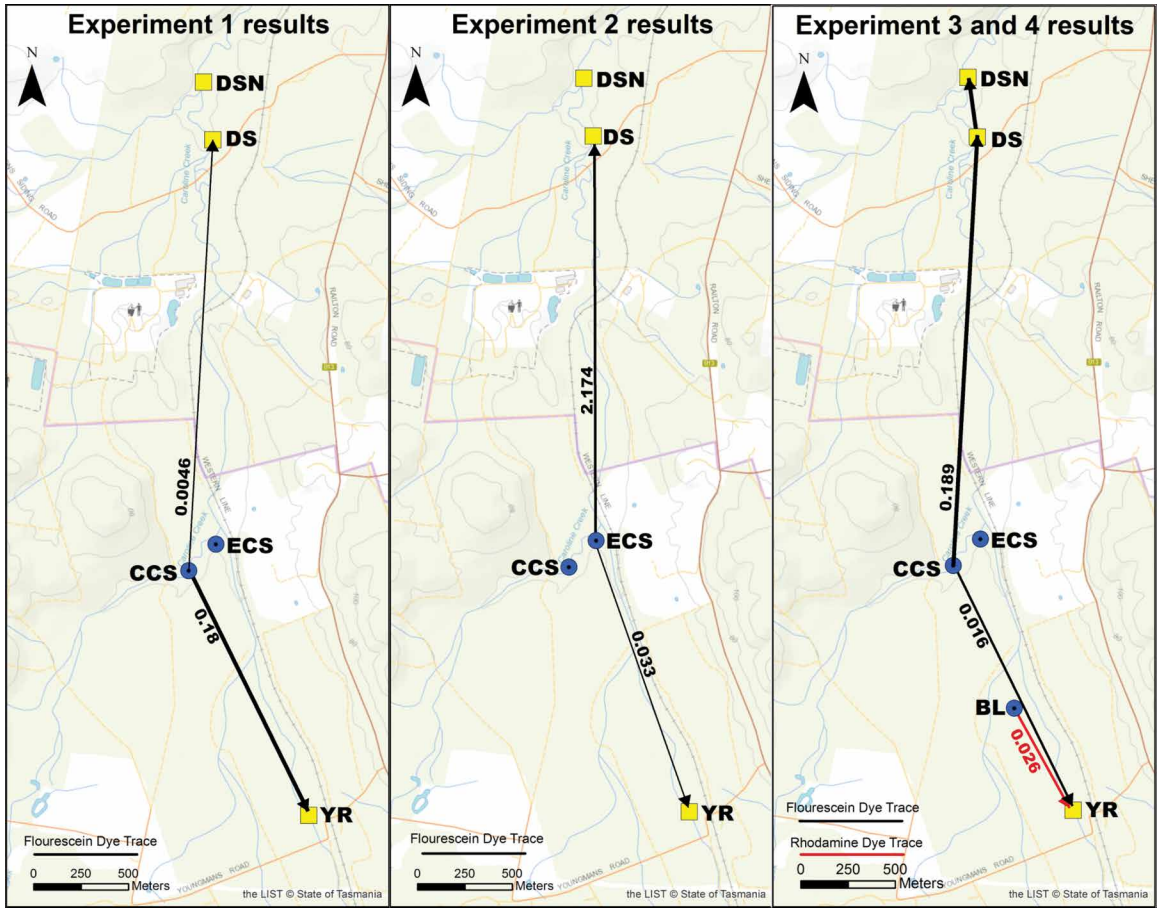

Figure 6. Dye-tracing results for Experiments 1, 2, 3, and 4. Blue circles are dye injection points and yellow squares are sampling sites. Normalized dye concentrations (NC-ppb) are shown next to arrows. Bold arrows indicate dominant flows. Note that Experiments 1 and 2 were conducted during low flows, and Experiments 3 and 4 during high flows.

Experiment 3

Rhodamine WT dye was injected into the sinkhole informally named Blue Lake (BL) on July 26, 2018 (Fig. 6, Experiment 3 and Fig. 7) when flow into Blue Lake (from an overflowing Eastern Creek) was estimated to be 5–7 L s^{-1}. At the time of injection water was ponded in the sinkhole. Two days later water had completely drained into a visible cave at the base of Blue Lake. 0.026 ppb

Figure 7. A. After heavy rain a lake (informally named Blue Lake) forms in Sinkhole 4 (photographed October 26, 2017); a small stream. B. (estimated flow 5–7 L/s) originating from a flooded Eastern Creek flows into it (photographed 26 July 2018). C. 870 g of Rhodamine WT dye was injected into this stream on July 26, 2018. D. By the afternoon of Saturday July 28, 2018 the lake had completely drained and the stream was seen cascading into an unstable vertical shaft at the base of the sinkhole which was over 7 m deep. The shadow line marks the approximate previous water level as shown in C.

of Rhodamine dye was detected in charcoal bags at YR between 22 and 48 h following injection (Fig. 6, Experiment 3). Rhodamine dye was not detected at DSS. No dye was recorded at Redwater Creek (RC). The experiment showed that a subsurface connection exists between Blue Lake and the upper reaches of Eastern Creek (YR) but no connection exists between BL and Redwater Creek (RC).

Experiment 4

Fluorescein dye was injected into the Caroline Creek Streamsink (CCS) on July 27, 2018 during high flow. Approximately one-third of flow was estimated to be entering the streamsink and two thirds to be flowing down the Caroline Creek surface channel. Charcoal bags were collected at the following times after injection: Dawson Siding (DS) 25 h and 172 h; Youngmans Road (YR) 1 h, 27 h 48 h and 171 h; Caroline Creek (CC) upstream of CCS 14 h; Redwater Creek (RC) 169 h. Caroline Creek (CCS) flow was approximately 1.08 $m^3 s^{-1}$. At YR 0.016 NC-ppb of fluorescein was detected (Fig. 6, Experiment 4) which is one-tenth of that observed during low flows (Fig. 6, Experiment 1), despite the concentration of fluorescein being injected being twice that injected in experiments 1 and 2 (Table 1). Most of the dye travelled downstream as surface flow to Dawsons Siding North (DSN) where high concentrations of 0.189 NC-ppb were recorded in under 25 h. The fluorescein dye reached Eastern Creek at YR from Caroline Creek Streamsink (CCS) within 1.25 h.

Fluorescein was first detected at DSN 4.9 h after injection by the fluorimeter and in the activated charcoal bags at DS at 25 h. A peak concentration of 6565 ppb was recorded in the fluorimeter (peak not shown in Fig. 8). Flow velocity was estimated as 0.15 m s^{-1} based on the surface distance between CCS and DSN (c. 2720 m). Four secondary peaks were detected at 52.1 h (168 ppb), 92.2 h (124 ppb), 105.1 h (123 ppb) and 132.5 h (87 ppb) (Fig. 8). These concentration peaks correspond with flow peaks in Caroline Creek (CCS) and Eastern Creek (ECS) upstream of their confluence and in Caroline Creek downstream of the confluence (CCC) (Fig. 8). The time interval between the consecutive five peaks was 46 h, 13 h, 41 h and 27 h (Fig. 8). The experiment confirmed the Experiment 1 result that a subsurface connection exists between Caroline Creek Streamsink (CCS) and the upper reaches of Eastern Creek (YR) and enabled flow rates to be estimated (see Discussion and Conclusions).

No dye was detected in Caroline Creek upstream of the streamsink (CCS) or in Redwater Creek (RC).

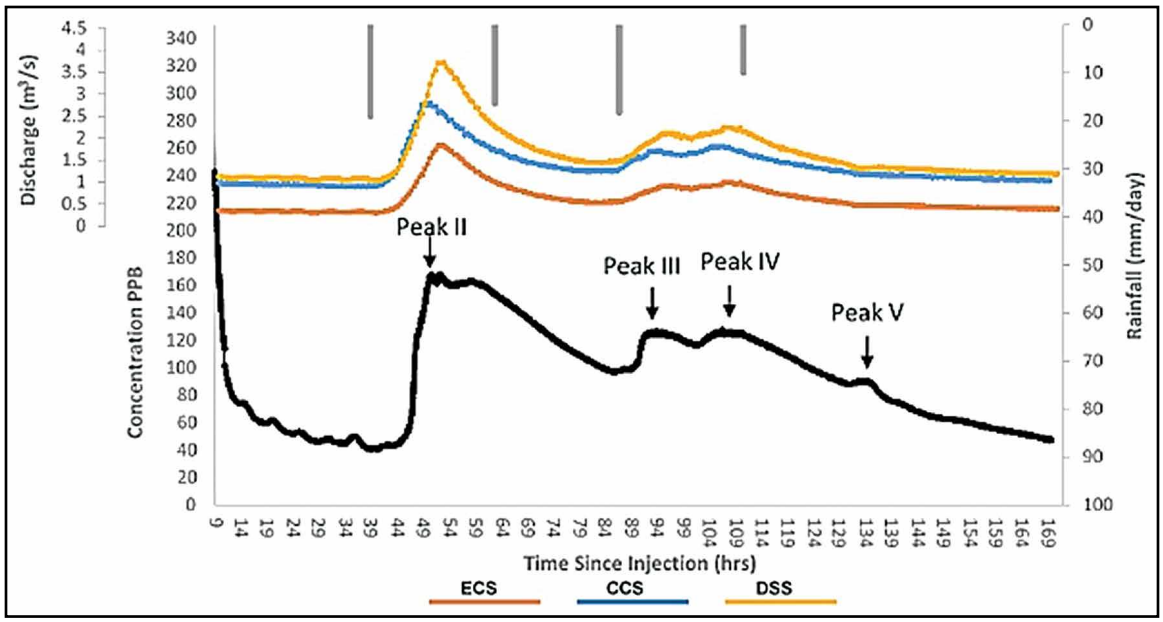

Figure 8. Fluorimeter dye trace record for Caroline Creek at DSN following fluorescein dye injection at CCS on July 27, 2018. The first peak occurred at 4.9 h and is not shown. The record illustrated covers the period 9–169 h following dye injection. Flow rates at ECS, CCS, and DSS are given on the y axis. Daily rainfall (mm/day) is shown by grey bars.

Table 2. Date and location of samples taken for water chemistry.

Date	Sample Location (Figure 2)[a]	Sample Notation s = summer; w = winter
Jan. 16, 2018	DSN	DSNs
Jan. 16, 2018	YR	YRs
July 27, 2018	DS	DSw
July 27, 2018	CCS[b]	CCSw
July 27, 2018	YR	YRw
July 28, 2018	BL	BLw

[a] YR = Youngmans Road; DS = Dawsons Siding; DSN = Dawsons Siding North; BL = Blue Lake; CCS = Caroline Creek Streamsink.
[b] The sample site was upstream of the streamsink

Water Chemistry

Samples were taken from Caroline Creek and Eastern Creek in summer 2017/2018 and winter 2018 (Table 2). The water chemistry results and *in situ* parameters such as temperature, pH and electrical conductivity of water samples are shown in Table 3.

Electrical conductivity (EC) of the water samples ranges from 98 µS cm^{-1} to 503 µS cm^{-1} (Table 3). The Caroline Creek water immediately upstream of the Caroline Creek Streamsink (CCSw) has the lowest EC values recorded (98 µS cm^{-1} during winter). There was no flow in Caroline Creek during summer. Highest EC values were recorded in Eastern Creek (YRs) (485 µS cm^{-1}) and Caroline Creek at Dawsons Siding North (DSNs) (503 µS cm^{-1}) in summer (Table 3). The pH values of the sampled waters range from 7.0 to 8.6 with higher values corresponding to higher EC values. In all

Table 3. Water chemistry, electrical conductivity, pH and temperature during low summer flows and high winter flows.

	Site (Figure 2)[a] and season							
	YR		DSN		BL		CCS	
Parameter	s	w	s	w	s	w	s	w
Temp. (°C)	23	12	19	9	···	10	···	7
pH	7.8	8.6	7.8	7.5	···	8.2	···	7.0
Conductivity (µS/cm)	485	438	503	195	···	405	···	198
Ca^{2+} (mg/L)	63	70	75	43	···	60	···	5
Mg^{2+} (mg/L)	6.1	6.3	5.9	4.5	···	5.6	···	2.6
Na^{+} (mg/L)	21	11	20	11	···	11	···	10
K^{+} (mg/L)	2.9	3.0	1.4	2.1	···	2.3	···	2.0
Cl^{-} (mg/L)	30	19	27	20	···	20	···	17
SO_4^{2-} (mg/L)	41	42	30	29	···	41	···	9
HCO_3^{-} (mg/L)	139	139	140	84	···	115	···	4
$\delta^{18}O$ (‰)	−5.2	−5.2	−5.1	−5.1	···	−5.1	···	−2.4
$\delta^{2}H$ (‰)	−27	−28	−26	−28	···	−29	···	−13
$\delta^{13}C$ (‰)	···	−10.5	···	−12.3	···	−11	···	−11.4

[a] YR = Youngmans Road; DSN = Dawsons Siding North; BL = Blue lake; CCS = Caroline Creek Streamsink; s = summer; w = winter.

but CCSw samples water chemistry is dominated by Ca^{2+} and HCO_3^- ions: Ca^{2+} concentrations are 5 mg L^{-1} in CCSw samples but are in the range 43–75 mg L^{-1} in all other samples. Likewise, HCO_3^- concentrations are 4 mg L^{-1} in CCSw samples but in the range 84–140 mg L^{-1} in all other samples. SO_4^{2-} values follow the same pattern: concentrations are 9 mg L^{-1} in CCSw samples and 29–42 mg L^{-1} in all other samples. Mg^{2+} concentrations are 2.6 mg L^{-1} in CCSw water but about double (range 4.5–6.3 mg L^{-1}) in all other samples. Na^+ and K^+ and Cl^- concentrations are similar in all samples, but Na^+ and Cl^- dominate the ionic composition of CCSw water because of the low levels of other ions.

Samples YRw, YRs, DSNw, DSNs and BLw have chemistry typical of carbonate waters with HCO_3^- and Ca^{2+} as the dominant ions (Knöll and Scheytt, 2018) and pH values in the range of 7.5–8.6 (Table 3). During summer and winter Caroline Creek (downstream of its confluence with Eastern Creek) and Eastern Creek (DSNs, DSNw) and YRs and YRw samples have similar major ion compositions; concentrations of Na^+ and Cl^- are higher in summer. DSNs water is very similar to YRs water but has slightly higher Ca^{2+} concentration. The Blue Lake water during winter (BLw) is similar to the YRw water from which it is largely derived by overland flow, the lower values for pH, conductivity, Ca^{2+}, Mg^{2+}, K^+ and HCO_3^- in BLw probably are due to dilution by rainwater.

Water stable isotope ratios for $\delta^{18}O$ and δ^2H for all samples fall on the Local Meteoric Waterline (LMWL) for Cape Grim, Tasmania (Fig. 9). At Cape Grim (162 km northwest of Railton) the variability of $\delta^{18}O$ and δ^2H isotope ratios in rainfall is reflected by enriched $\delta^{18}O$ isotopes in summer and depleted $\delta^{18}O$ isotopes in winter by a factor of approximately ± –5 (GNIP, 2018). Stable isotope ratios from samples taken in winter are depleted with respect to average rainfall isotope composition and range from −5.2 ‰ to −5.1 ‰ for $\delta^{18}O$ and −28 ‰ to −25 ‰ for δ^2H, respectively. Water in samples from the Blue Lake sinkhole (BLw), Caroline Creek downstream of the recharge zone and confluence (DSNw) and Eastern Creek upstream of the recharge zone and confluence (YRw) are slightly more depleted in winter with values of −5.1 ‰, −5.1 ‰ and −5.2 ‰ for $\delta^{18}O$ and −29 ‰, −25 ‰ and −28 ‰ for δ^2H, respectively. During both summer and winter Eastern Creek (YR) has depleted isotope signatures reflecting winter rainfall with values of −5.2 ‰ $\delta^{18}O$ and −28 ‰ δ^2H in winter and −5.0 ‰ $\delta^{18}O$ and −27 ‰ δ^2H in summer, respectively.

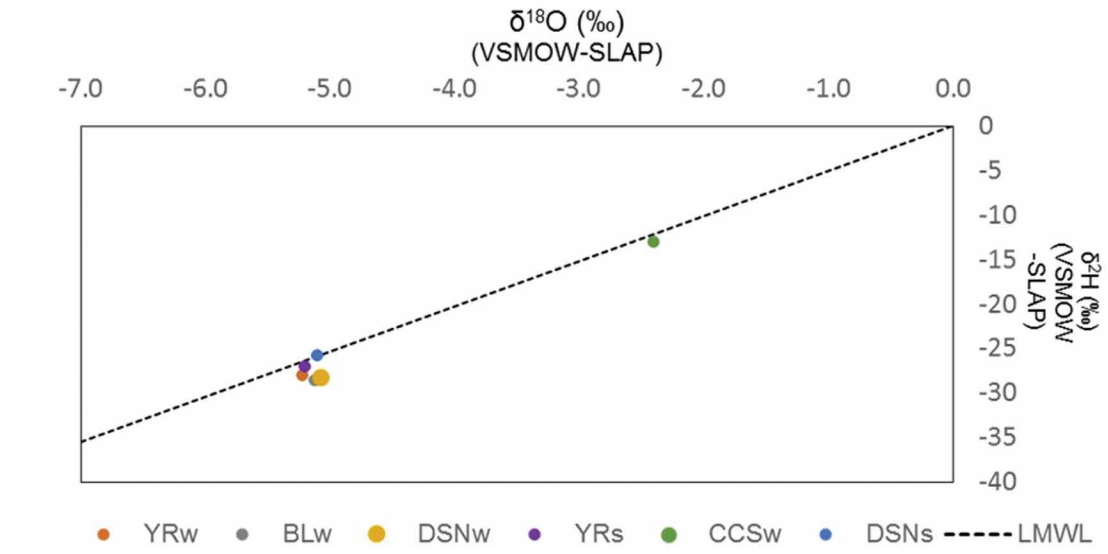

Figure 9. Water-stable isotopes of stream samples, plotted on the LMWL (Cape Grim, Tasmania; Liu et al. 2010).

Carbon isotope ratios ($\delta^{13}C$) were determined for winter samples only (Table 3). The $\delta^{13}C$ ratios range from −16.2 ‰ to −10.5 ‰. There is a direct positive correlation between Ca^{2+} concentrations and $\delta^{13}C$ isotope ratios. Eastern Creek (YRw), Blue Lake (BLw) and Caroline Creek downstream of the recharge zone and confluence (DSNw) have the highest concentrations of Ca^{2+} and highest $\delta^{13}C$ ratios of −10.5 ‰, −11 ‰, −12.3 ‰ and −11.4‰ respectively. Caroline Creek upstream of the recharge zone and confluence (CCSw) water is less enriched in $\delta^{13}C$ (−16.2 ‰) and has comparatively low Ca^{2+} concentrations.

Isotope data (Table 3; Fig. 10) shows that with the exception of sample CCSw, taken from Caroline Creek stream above the streamsink in July (winter), all stream samples taken in both winter and summer have similar $\delta^{18}O$ and δ^2H isotopic composition and plot together.

Karst Disturbance Index

Van Beynen and Townsend (2005) developed a karst disturbance index which North et al. (2009) applied (in slightly modified form) to karst landscapes of Florida and southeast Italy. In the Railton study area, the usefulness of the index is hampered by the lack of data for many indicators used. For example, no information is available on the condition of

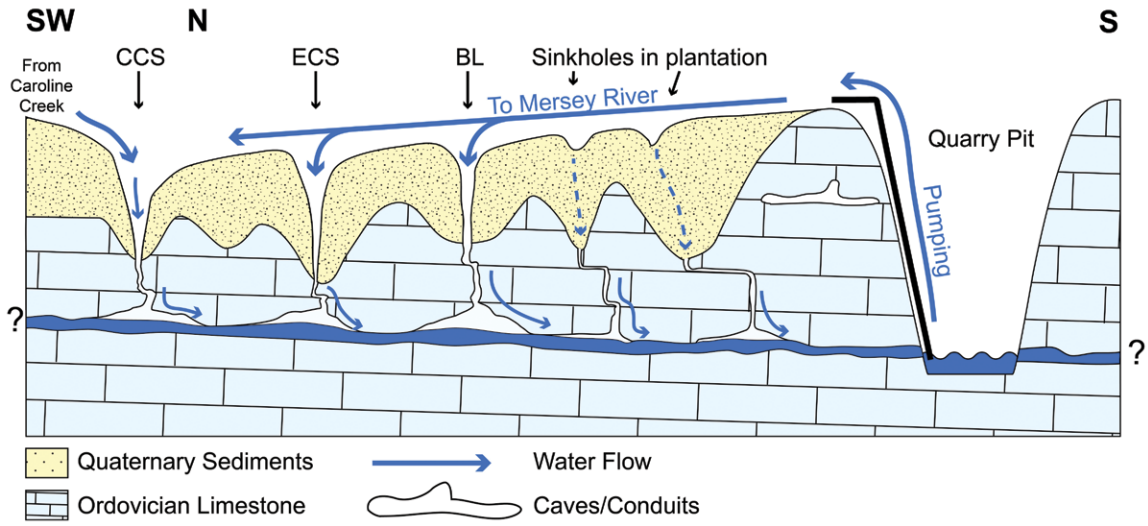

Figure 10. Diagrammatic representation of surface and subsurface flows induced by intersection of cave system at Dulverton Pit and pumping of water from Dulverton Pit to the headwaters of Eastern Creek. Not to scale. This representation is a simplification and the cave system involved may have multiple stream channels.

the caves before human land-use changes of either Aboriginal or European origin or on the condition of stream microbiota. Consequently, only 5 of the 30 criteria listed by North et al. (2009) could be assessed with any confidence on the 0–3 scale used. Maximum scores of 3 (North et al., 2009) were assigned to three severity indicators: quarrying ("large open-cast mines"); erosion ("severe" on account of large sinkhole initiation); and "changes in water table" (likely to exceed 35 m). A score of 2 was assigned to regulatory protection ("weak regulations": the Tasmanian Water Management Act (1999, section 51), is not specific about controlling the effects of quarrying on groundwater). A score of 1 was applied to road building ("some country lanes"). Tires have been dumped in one sinkhole at Railton, but this observation was not included in the disturbance index assessment because scores for industrial pollution chiefly concern liquid pollutants such as oils and water-soluble chemicals (Van Beynen and Townsend, 2005; North et al., 2009). Such contaminants were not noted in Railton sinkholes, although they could present a risk to water quality in the future as they have done elsewhere (Delle Rose et al., 2007; Parise, 2016). The tally of 12 out of a possible 15 gives a karst disturbance index value of 0.8 ("highly disturbed").

Discussion and Conclusions

Sinkhole Characteristics

All the sinkholes noted are cover-collapse sinkholes (Fig. 3 and 4). Sinkholes in the study area tend to concentrate and enlarge along the major syncline fold axis (340°) implying that limestone dissolution (the ultimate control of sinkhole formation) is preferentially occurring along the syncline fold axis, as noted by Yan et al. (2008) and Goldscheider and Neukum (2010). Elsewhere sinkholes occur, often in a linear pattern, where limestone permeability is highest (e.g. Lolcama et al., 2002; Basso et al., 2013; Pepe and Parise, 2014; Kobal et al., 2015; Siska et al., 2016). Although the sinkholes in the study area were commonly circular in plan at the time of initial collapse, they elongate along the trend of karst drainage as a result of gradual soil loss by suffusion processes into the underlying karst aquifer, as described by Zhou and Beck (2008).

Cover-collapse sinkholes are particularly common in areas where more cohesive layers overlie less consolidated deposits (Tharp, 1999) and in areas like the Railton valley where thick deposits (usually sedimentary) mantle karst (Noury et al., 2018; Intrieri et al., 2018). Langer (2001) cited several studies that showed that cover-collapse sinkholes were most likely to form when the water table first declines past the bedrock/soil contact in areas where the unconsolidated sediments overlying limestone are 5–30 m thick as in the Railton area, although other factors like the nature of the clay fraction in the sediments also influence the risk of sinkhole forming. Because cover-collapse sinkholes generally develop from the limestone surface up into the cover sediments (Kaufmann and Quinif, 2002; Soliman et al., 2018) surface collapse is unpredictable, creating an environmental hazard (Waltham, 2008), particularly for machines (Fig. 4).

Subsurface Flows in Relation to Dulverton Pit

Dye experiments 1 and 2 clearly demonstrated that during low stream flows subsurface flow occurs between both the Caroline Creek Streamsink (CCS) and Eastern Creek at Youngmans Road (YR) and between the Eastern Creek Streamsinks (ECS) and Eastern Creek at Youngmans Road (YR) (Fig. 6), approximately following the limestone syncline axis. For flow from both streamsinks to enter the subsurface karst drainage system and then reappear upstream at a higher altitude (>5 m by surface mapping, but >12 m if streamsink depth is taken into account), the subsurface flow

must be pumped to higher elevation, i.e. pumping of incoming water in Dulverton Pit into Eastern Creek headwaters, to maintain dry conditions in the quarry, is responsible for the circulation of dye to the upper (southern) reach of Eastern Creek. Pumping has created a zone of low hydraulic pressure in the south of the study area at the limestone quarry (Dulverton Pit), where the base of the quarry is approximately 60 m below sea level (Google Earth, 2016 imagery). We conclude that quarry deepening and regular dewatering has caused a localized reduction in hydraulic head and a draw-down of the regional water table, as previously shown by Langer (2001). This has resulted in the formation of a cone of depression (Langer, 2001; Lolcama et al*.,* 2002). Cones of depressions around limestone quarries can extend laterally for more than 26 km (Langer, 2001). Therefore, given the closeness of the quarry to the streamsinks (2.85 km) it is highly likely that low hydraulic head at the quarry is causing groundwater flows to be directed south, in the opposite direction to natural surface flows. Flow is likely to occur through a large confined aquifer in a cave system, which would heighten the hydrologic gradient and rates of flow.

In the conceptualization outlined above the quarry site captures groundwater that is subsequently pumped into Eastern Creek and transported as surface flow downstream (Fig. 10). Surface water in Eastern Creek then re-enters the subsurface system via the streamsinks and the cycle continues, i.e. there is a continuous cycle of water from the quarry, to Eastern Creek, and back to the quarry. During high flow fluorescein dye injected into the Caroline Creek Streamsink (CCS) was detected in Eastern Creek (YR) within 1.25 h, indicating a flow speed through the 4.6 km system (from CCS to Dulverton Pit to YR) of about 1 m/s under high inflows. During low flows, when Caroline Creek does not flow consistently, field observations indicate that Eastern Creek is the dominant contributor to the karst aquifer (via the Eastern Creek streamsinks), although entry of water into the aquifer from the upper reaches of Caroline Creek (not investigated) cannot be excluded. Because water is recycled in this way, the quarry requires dewatering throughout the year so that the measured difference between quarry discharge at low and high flows is on average only 0.15 $m^3\ s^{-1}$.

Experiment 3 shows that water entering Blue Lake (from Eastern Creek) also flows into Eastern Creek, higher in the catchment, at Youngmans Road (YR) and this observation is also readily explained by lower hydraulic pressure at the quarry and pumping of water into the upper reaches of Eastern Creek, i.e. drainage from sinkholes, as well as drainage from streamsinks feeds the same aquifer, and subsurface flow is via the subterranean aquifer (cave system) and Dulverton Pit.

Water Chemistry

The differences between the water chemistry of CCSw and water from YR, DSN and BL sites can be explained by CCSw flow being derived entirely from relatively fast overland flow of meteoric water with little mineral dissolution. In contrast DSNs, DSNw, YRs, YRw and BLw water analyses all show evidence of calcite dissolution (high concentrations and a molar ratio of 1:2 of Ca^{2+} and HCO_3^-). Thus, we conclude that the stream water at Youngmans Road (YRs and YRw) and at points downstream (DSNs, DSNw and BLw) has all been influenced by subsurface flow through limestone. The lower levels of total dissolved solids (lower EC) and slightly lower pH in DSNw samples than in YRs, YRw and DSNs samples indicate dilution of DSNw water with direct runoff of meteoric water from Upper Caroline Creek (CCSw) flow. The source of the high SO_4^{2-} in YRs and YRw water (Table 2) is unknown but may be gypsum used as a flocculant used on roads in the area or in the quarry. High Mg^{2+} is unlikely to originate from limestone dissolution as the limestone at Railton contains only 1.5 % MgO (Jennings, 1960). An alternative source is weathering of basalt and dolerite clasts derived from local outcrops within the Quaternary sediments. The range of MgO concentration in dolerite is large (1–11 %), but mean concentrations are c. 6 % (Hergt et al., 1989) and similar MgO concentrations are found in basalts (Compston et al., 1968).

Oxygen isotope ratios are higher ($\delta^{18}O = -2.4$ ‰) in Caroline Creek (CCSw) than in all other samples (Table 3, Fig. 9), most likely because the flow in Caroline Creek upstream of the streamsink is derived from meteoric water. The analysed sample, taken on July 27, 2018, may not be typical of winter rainfall, since it falls in the range of oxygen isotope ratios ($\delta^{18}O = 0$ to -3 ‰) typical of summer rainfall at Cape Grim, northwest Tasmania, rather than in the winter range ($\delta^{18}O = -3$ to -6 ‰) (Liu et al., 2010) (Fig. 9).

All other samples group closely together, with more depleted oxygen and hydrogen isotope ratios indicating that most of these water samples are derived from winter rainfall. Isotope ratios in the field area deviate slightly from those for weighted average Cape Grim rainfall ($\delta^{18}O = -4.0$ ‰ and $\delta^{2}H = -21.5$ ‰), which can be explained either by the distance of the field area from the coast, or the water in the karst system having accumulated over a shorter time period than that over which the Cape Grim average has been derived (~20 years average). As rainfall at Railton is highest in winter and evapotranspiration is highest in summer (when Caroline Creek often ceases to flow), water in the karst system is likely to be largely derived from winter rainfall, but whether it is derived largely from the previous winter's rainfall or over a longer period cannot be ascertained.

$\delta^{13}C$ ratios for most waters are below the average ratios of recharge through soils (-23 to -17 ‰ $\delta^{13}C$) indicating that chemical dissolution of the carbonates ($\delta^{13}C \sim 0$ ‰) in the aquifer and rapid mixing has not only influenced the ionic

composition of the water in the cave system (and all downstream water derived from it) but has also altered its isotopic composition.

Seasonal Flow Variation

Caroline Creek is a seasonally losing stream with periods of no or low flow ($\mu = 0.16$ m^3 s^{-1}, $\sigma = 0.15$ m^3 s^{-1}) during January to April 2018 (Burke, 2018), when all flow immediately upstream of CCS flows into the CCS streamsink. From June to July 2018 Caroline Creek flow responds to rainfall and has more than double the average flow of Eastern Creek ($\mu = 1.43$ m^3 s^{-1}). Losing streams of this nature are common in karst worldwide and indicate subsurface drainage (e.g., Lolcama et al*.,* 2002; O'Driscoll and Dewalle, 2006). In contrast, Eastern Creek flows all year and has low overall flow variability ($\mu = 0.57$, $\sigma = 0.10$ m^3 s^{-1}), because of consistent pumping of groundwater from Dulverton Pit into Eastern Creek to maintain dry quarry conditions. Measurements during high flows between June 12, 2018 and July 3, 2018 indicate that the streamsinks in both Caroline Creek and Eastern Creek contribute averaged flow of 0.37 m^3 s^{-1} into the subsurface system with peaks reaching 1.58 m^3 s^{-1} (i.e., up to 48 % percent of the combined flow in upstream Caroline and Eastern Creeks). This percentage exceeds the maximum autogenic inputs from losing streams measured by other studies (e.g., Scanlon et al*.,* 2002). Therefore, surface-groundwater connectivity of the karst system is very high.

The fluorimeter results confirm the cycling of water between the streamsinks in Eastern Creek and Dulverton Pit. Five peaks in fluorescein concentration were observed at downstream Caroline Creek (DSN) following dye injection at the Caroline Creek streamsinks (CCS) during high flow (Fig. 9 shows the last four peaks). The initial and largest peak occurred 4.9 h after injection and is attributed to overland flow. (The dye had an approximate velocity of 0.21 m s^{-1} which is similar to the measured stream velocity of 0.31 m s^{-1}.) As fluorescein is rapidly decomposed by sunlight and approximately 50 % of fluorescein dye is decomposed within three hours of direct exposure (Feuerstein and Selleck, 1963), it is reasonable to conclude that any fluorescein still present in Caroline Creek surface water after the 4.9 h peak would have been destroyed by exposure to sunlight before the secondary peaks were recorded 50 h after injection. Therefore, the fluorescein dye must have been stored/transported underground following injection for it to be recorded in surface flow after 50 h.

There are two possible explanations for the four secondary peaks in fluorescein concentration. (1) The peaks have been caused by pulses through the karst system resulting from fresh rainfall in the Caroline Creek catchment, an explanation apparently supported by the peaks corresponding with increased flow following rainfall (Fig. 8). However, although such an effect is common in monitored karst springs (e.g. Goldscheider et al*.,* 2008; Filippini et al*.,* 2018), it is unlikely that small pulses of rainfall feeding an aquifer could result in such clear secondary peaks. (2) The peaks are due to recirculation of the dye through the ECS–Dulverton Pit–YR–ECS circuit as a result of quarry pumping. This second explanation is supported by the fact that the peaks coincide with increased flows in Eastern Creek attributed to pumping from Dulverton Pit (Fig. 8). Explanation 2 is therefore more likely to be correct.

Regional Karst Connections

In Experiments 2, 3, and 4 the investigation was extended beyond the immediate study area to determine if dye injected into the karst aquifer system drained to points further afield (Burke, 2018), as Ordovician limestone covers an area of approximately 14 km^2 within the study area and extends northwards to Latrobe and southwards to Kimberley (Kiernan, 1995b). No dye was detected at Redwater Creek (RC) after dye injection, either during low or high flows, indicating that, at present, subsurface drainage from the north does not continue south past Dulverton Pit. No dye was detected in any of the five northern streams during high flows (Burke, 2018). It is therefore unlikely that subsurface drainage continues to minor streams north of the study area. However, fluorescein was noted in charcoal bags installed in the Mersey River during low flows (Burke, 2018), the low value of 0.006 NC-ppb probably being due to downstream dilution of dye carried in Caroline Creek. Analysis of major ions support these dye tracing findings; none of the streams sampled outside the confines of the direct study area (Fig. 1) showed signs of calcite dissolution (Burke, 2018, appendix 3).

The hydrogeology results show that drainage in the Railton karst system is dominated by caves with high subsurface connectivity (Fig. 10). This type of karst system is best described as a 'dominant conduit model' (Vigna and Banzato, 2015; Filippini et al*.,* 2018) in which (1) surface – groundwater connectivity is high and surface water rapidly infiltrates the system; (2) water is efficiently transported through the system by a network of connected subsurface conduits; and (3) flow is towards the zone of lowest hydraulic pressure. Preferential drainage routes are along weaknesses in the rock structure such as faults or folds.

Sinkhole Formation Mechanisms in the Study Area

Sinkholes close to the Railton railway were mapped by Matthews et al. (1983) and in 2003 by the FPA (N. Duhig, unpublished FPA report). Sinkholes close to the quarry first appeared on satellite imagery in 2007 and were relatively slow to form. Sinkhole formation appears to have accelerated by early 2011 when the first sinkholes were observed in the study area. According to Langer (2001) sinkholes can be triggered by events such as water level fluctuations,

increased groundwater velocity and removal of vegetation. Thus, three triggering events can be hypothesised: (1) harvesting of the plantation with subsequent increased soil water saturation and water transmission to subsurface layers; (2) significant flooding after heavy rain in 2011 and 2016 resulting in opening of previously blocked drainage routes; and/or (3) intersection of groundwater and subsurface conduits as a result of deepening of Dulverton Pit.

The study area was harvested in 2013. It is well-known that vegetation clearing removes root support. It also decreases transpiration losses and increases the percolation of surface water into karst aquifers, which can lead to enhanced dissolution (Kiernan, 2002; Urich, 2002). However, large sinkholes began to form before forest harvest and elsewhere plantation harvest in areas of cover-collapse sinkholes in Tasmania has been shown to have no detectable effect on sinkhole development (Slee et al., 2019). Furthermore, the harvest area was previously unforested (cleared) agricultural land and before European settlement was almost certainly covered by native forest which would have been subject to many forest-destroying natural and man-made fires over millennia. Neither fires nor clearing for agriculture has had an effect on the stability of the Quaternary sedimentary deposits. A significant effect of vegetation clearance on sinkhole formation is therefore discounted.

Rainfall at Railton in January 2011 was 201 mm (Bureau of Meteorology, 2019), which is more than three times the 15-year January mean of 60 mm. In June 2016, rainfall was 238 mm, which was more than double the 15-year June average of 102 mm (Bureau of Meteorology, 2019). Annual rainfall in 2011, 2013, and 2016 exceeded the long-term annual average of 1058 mm by 116 mm, 360 mm, and 576 mm respectively. Aerial surveys show that two new sinkholes (sinkholes 7 and 8; Fig. 2) formed in the study area at Railton between 2015 and 2017 and may have formed after high rainfall in June 2016. However, the deviations of monthly rainfall from the mean, noted above, are not exceptional, and similar and higher rainfall totals, as well as numerous droughts, are likely to have occurred many times before records began, causing no collapse. For these reasons, we consider that high rainfall has not initiated sinkhole formation north of Youngmans Road, but episodes of high rainfall have probably accelerated erosion of existing sinkholes.

We conclude that the primary cause of sinkhole collapse at Railton is intersection of groundwater, and specifically a cave system, by the limestone quarry (Dulverton Pit), as predicted by Jennings (1959, p. 7) who warned that "the limestone [at Railton] has been shown by drilling and quarrying to contain fairly large underground cave systems, and if these were encountered below the level of the water table, they would certainly drain embarrassingly large quantities of water into the cut".

The proposed process for sinkhole formation in the study area is as follows: (1) the cone of depression around the quarry has lowered the water table and increased the thickness and extent of the vadose zone in the study area in a manner similar to that described by Langer (2001), Lolcama et al. (2002), Urich (2002), Hobbs and Gunn (2008), Heidari et al. (2011,) and Khanlari et al. (2012); (2) around 2010 to 2011 deepening of Dulverton Pit drained pre-existing caves around the quarry of water, including a cave system extending c. 3 km north of the quarry; (3) streamsinks and sinkholes formed because of the lowering of the water table and the consequent decline of hydraulic support for sediment overlying the limestone; (4) a proportion of stream water that normally flowed north then flowed south to the quarry (Figs. 6 and 10), carrying the sinkhole-derived sediment with it; (5) periods of high rainfall have resulted in sinkhole enlargements—higher stream turbidity in winter (TDS = 18.7 NTU) than in summer (TDS = 2.5 NTU) (Burke, 2018) is attributed to greater sinkhole erosion and collapse during high winter rainfall and flushing of fine sediment from subsurface conduits by winter flows.

The cover-collapse sinkholes documented during this study are similar to sinkholes developed in other karst areas buried by thick Quaternary overburden deposits that have been impacted as a result of regional water table lowering. As mentioned in the Introduction, there are numerous examples of quarrying or withdrawal of water from aquifers lowering water tables and causing sinkholes to form in surrounding land, due to the removal of buoyant support for sediments or soils above the sediment/limestone contact (Kaufmann and Quinif, 2002; Parise and Pascali, 2003; Heidari et al., 2011; Khanlari et al., 2012; Jovanelly, 2014; Dell'Aringa et al., 2014; Jia et al., 2018; Pan et al., 2018). The process is well-illustrated in the review by Langer (2001, fig. 20b) and matches five steps in the process he describes: quarrying dewatering lowers the water table; a stream dries up (in this case two streams flow into streamsinks); underground cavities form in unconsolidated sediments due to loss of buoyant support provided by the previous high water table; ground subsides, resulting in wet areas and tilted trees; and collapse occurs, creating sinkholes.

Hazards and Hazard Prediction

The karst-associated hazards in this area are: (1) unpredictable collapse during forest operations (Fig. 4); (2) threats to infrastructure such as the railway, the electricity transmission line, roads and the Dulverton Tip (Fig. 1); (3) changes to biodiversity of streams resulting from intermittent flows and drying of channels downstream of streamsinks; and (4) changed water chemistry. The study demonstrates that the risks associated with water-table lowering by quarrying in limestone are not limited to classical "cones of depression" immediately around quarries and mines. Effects are magnified if relict subsurface stream channels (cave systems) are intersected by mining, as predicted in this area by Jennings

(1959), and may extend for kilometres, as shown in this study and elsewhere (Langer, 2001). Predicting the presence and orientation of such cave systems is difficult, but they are likely to occur preferentially along features such as fault lines, fracture zones, or as in the case studied, syncline axes. As emphasised by Parise (2016), karst features and their associated water resources are vulnerable and quarrying in karst areas should be carefully designed, planned and controlled. In this karst area, the actual environmental effects and potential negative socio-economic effects of mining on infrastructure and rural land use are large and need to be addressed.

Acknowledgements

Forico Pty Limited allowed access to the study area. We are indebted to James Dick and Simon Cook of Forico Pty Ltd for encouraging the research and acquiring and providing the high-resolution drone imagery used for sinkhole mapping. The Forest Practices Authority Board provided the funding for B. Burke to undertake this project, and travel costs for H. Hofmann. The analysis of the activated charcoal samples was undertaken at Ozark Underground Laboratory, Missouri, USA. We are grateful to Martin Peersmann of the Ministerie van Infrastrutuur en Milieu, Den Haag and two anonymous reviewers for their constructive suggestions for improving the manuscript.

References

Al-Halbouni, D., Holohan, E.P., Taheri, A., Schöpfer, M.P.J., Emam, S., and Dahm, T., 2018, Geomechanical modelling of sinkhole development using distinct elements: model verification for a single void space and application to the Dead Sea area: Solid Earth, v. 9, p.1341–1373. https://doi.org/10.5194/se-9-1341-2018

Augarde, C.E., Lyamin, A.V., and Sloan, S.W., 2003. Prediction of undrained sinkhole collapse: Journal of Geotechnical and Geoenvironmental Engineering, v. 129, p. 197–205. https://doi.org/10.1061/(ASCE)1090-0241(2003)129:3(197)

Basso, A. Bruno, E., Parise, M., and Pepe, M., 2013, Morphometric analysis of sinkholes in a karst coastal area of southern Apulia, Italy: Environmental Earth Sciences, v. 70, p. 2545–2559. https://doi.org/10.1007/s12665-013-2297-z

Baublys, K.A., Hamilton, S.K., Golding, S.D., Vink, S., and Esterle, J., 2015, Microbial controls on the origin and evolution of coal seam gases and production waters of the Walloon Subgroup; Surat Basin, Australia: International Journal of Coal Geology, v. 147–148, p. 85–104. https://doi.org/10.1016/j.coal.2015.06.007

Bonacci, O., 2004, Hazards caused by natural and anthropogenic changes of catchment area in karst: Natural Hazards and Earth System Sciences, v. 4, p. 655–661. https://doi.org/10.5194/nhess-4-655-2004

Brinkmann, R., Parise, M., Dye, D., 2008, Sinkhole distribution in a rapidly developing urban environment: Hillsborough County, Tampa Bay area, Florida: Engineering Geology, v. 99, p. 169–184. https://doi.org/10.1016/j.enggeo.2007.11.020

Brown, A.V., McClenaghan, M.P., Turner, N., Baillie, P.W., Lennox, P.G., McClenaghan, J., Lennox, P., and Williams, P.R., 1982, Geological Atlas 1:50000 series. Huntley. Tasmanian Department of Mines.

Bureau of Meteorology, 2019, Monthly Rainfall, Railton (Dowbiggin Street) station 91332. http://www.bom.gov.au/jsp/ncc/cdio/weatherData/av?p_nccObsCode=139&p_display_type=dataFile&p_stn_num=091332 .

Burke, B., 2018, An investigation into sinkhole formation in Railton, Tasmania [B.Sc. Thesis]: Queensland, University of Queensland.

Calligaris, C., Devoto, S., and Zini L., 2017, Evaporite sinkholes of the Friuli Venezia Giulia region (NE Italy): Journal of Maps, v. 13, p. 406–414. https://doi.org/10.1080/17445647.2017.1316321

Compston, W., McDougall, I., and Heier, K.S., 1968, Geochemical comparison of the Mesozoic basaltic rocks of Antarctica, South Africa, South America and Tasmania: Geochimica et Cosmochimica Acta 32, p. 129–149. https://doi.org/10.1016/S0016-7037(68)80001-8

Cooley, T., 2002, Geological and geotechnical context of cover collapse and subsidence in mid-continent US clay-mantled karst: Environmental Geology, v. 42, p. 469–475. https://doi.org/10.1007/s00254-001-0507-6

Cooper, A.H., Farrant, A.R., and Price, S.J., 2011, The use of karst geomorphology for planning, hazard avoidance and development in Great Britain: Geomorphology, v. 134, p. 118–131. https://doi.org/10.1016/j.geomorph.2011.06.004

Csaky, D., 2003, Review of karst hazards in the Wanneroo area, Perth, Western Australia. Minerals and Geohazards Division, Perth Cities Project. Geoscience Australia report, 44 p.

Dell'Aringa, M., Giannecchini, R., and Puccinelli, A., 2014, Small sinkhole-like features in alluvial plains: the example of Paganico (Lucca Plain, Italy). Natural Hazards and Earth Systems Sciences, v. 1, p. 3413–3448. https://doi.org/10.5194/nhessd-1-3413-2013

Delle Rose, M., Parise M., and Andriani, G.F., 2007, Evaluating the impact of quarrying on karst aquifers of Salento (southern Italy), *in* Parise, M., and Gunn, J., eds.: Natural and anthropogenic hazards in karst areas: Recognition, Analysis and Mitigation. Geological Society of London, Special Publication 279, p. 153–171. https://doi.org/10.1144/SP279.13

Doctor, D.H., and Young, J.A., 2013, An Evaluation of Automated GIS Tools for Delineating Karst Sinkholes and Closed Depressions from 1-Meter LiDAR-Derived Digital Elevation Data: https://scholarcommons.usf.edu/cgi/viewcontent.cgi?referer=http://scholar.google.com.au/&httpsredir=1&article=1156&context=sinkhole_2013. https://doi.org/10.5038/9780979542275.1156

Donaldson, R.C., 1984, An inspection of sinkholes at Railton: Tasmania Department of Mines 1984/88.

Eberhard, R., 1994, Inventory and management of the Junee River karst system, Tasmania: Forestry Tasmania, Hobart, 125 p.

Eberhard, R., 1998, Planning for karst management in multiple-use forest: The Junee-Florentine karst study: Tasforests, v. 10, p. 33–47.

Eberhard, R., 2007, Land Classification and Tasmania's Karst Estate – A GIS Review, AKMA Journal, v. 66, p.10–14.

Feuerstein, D. L., and Selleck, R. E., 1963, Fluorescent tracers for dispersion measurement: Journal of the Sanitary Engineering Division, v. 89, p. 1–22.

Filippini, M., Squarzoni, G., De Waele, J., Fiorucci, A., Vigna, B., Grillo, B., Riva, A., Rossetti, S., Zini, L., Casagrande, G., and Stumpp, C., 2018, Differentiated spring behavior under changing hydrological conditions in an alpine karst aquifer: Journal of Hydrology, v. 556, p. 572–584. https://doi.org/10.1016/j.jhydrol.2017.11.040

Flett, V., Maurice, L., Finlayson, A., Black, A.R., MacDonald, A.M., Everest, J., and Kirkbride, M.P., 2017, Meltwater flow through a rapidly deglaciating glacier and foreland catchment system: Virkisjökull, SE Iceland: Hydrology Research, v. 48, p. 1666–1681. https://doi.org/10.2166/nh.2017.205

Forest Practices Authority, 1987, Forest Practices Code: Forest Practices Authority, Hobart.

Forest Practices Authority, 2015, Forest Practices Code: Forest Practices Authority, Hobart.

Frisbee, M.D., Meyers, Z.P., Miller, J.B., Gleason, C.L., Stewart-Maddox, N.S., Larson, E.B., Granger, D.E., Saksena, S., Dey, S., and Frisbee, E.E., 2019, Processes leading to the re-activation of a sinkhole in buried karst and the subsequent drying of waterfalls in a small catchment located in northern Indiana, USA: Journal of Cave and Karst Studies, v. 81, p. 69–83. https://doi.org/10.4311/2017ES0116

GNIP, 2018, Global Network of Isotopes in Precipitation, Water Resources Program, International Atomic Energy Agency, Vienna. http://www-naweb.iaea.org/napc/ih/IHS_resources_gnip.html.

Goldscheider, N., and Neukum, C., 2010, Fold and fault control on the drainage pattern of a double-karst-aquifer system, Winterstaude, Austrian Alps: Acta Carsologica, v. 39, p. 173–186. https://doi.org/10.3986/ac.v39i2.91

Goldscheider, N., Meiman, J., Pronk, M., and Smart, C., 2008, Tracer tests in karst hydrogeology and speleology: International Journal of Speleology, v. 3791, p. 27–40. https://doi.org/10.5038/1827-806X.37.1.3

Grimes, K.G., 1994, The south-east karst province of South Australia: Environmental Geology, v. 23, p. 134–148. https://doi.org/10.1007/BF00766987

Grimes, K.G., 1999, The water below: an introduction to karst hydrology and the hydrological setting of the Australian karsts: Proceedings of the 13th Australasian Conference on Cave and Karst Management, p. 24–31.

Gutiérrez-Santolalla, F., Gutiérrez-Elorza, M., Marín, C., Desir, G., and Maldonado, C., 2005, Spatial distribution, morphometry and activity of La Puebla de Alfindén sinkhole field in the Ebro river valley (NE Spain): applied aspects for hazard zonation: Environmental Geology, v. 48, p. 360–369. https://doi.org/10.1007/s00254-005-1280-8

Gutiérrez, F., Parise, M., De Waele, J., and Jourde, H., 2014, A review on natural and human-induced geohazards and impacts in karst: Earth Science Reviews, v. 138, p. 61–88. https://doi.org/10.1016/j.earscirev.2014.08.002

Heidari, M., Khanlari, G.R., Taleb Beydokhti, A.R., and Momeni, A.A., 2011, The formation of cover collapse sinkholes in North of Hamedan, Iran: Geomorphology, v. 132, p. 76–86. https://doi.org/10.1016/j.geomorph.2011.04.025

Hergt, J.M., Chappell, B.W., McCulloch, M.T., McDougall, I., and Chivas, A.R., 1989, Geochemical and isotopic constraints on the origin of the Jurassic dolerites of Tasmania: Journal of Petrology, v. 30, p. 841–883. https://doi.org/10.1093/petrology/30.4.841

Hobbs S. L., and Gunn, J., 1998, The hydrogeological effect of quarrying karstified limestone: options for prediction and mitigation: Quarterly Journal of Engineering Geology and Hydrogeology, v. 31, p. 147–157. https://doi.org/10.1144/GSL.QJEG.1998.031.P2.10

Hunt, B.B., Smith, B.A., Adams, M.T., Heirs, S.E., and Brown N., 2013, Cover-collapse sinkhole development in the Cretaceous Edwards limestone, Central Texas: NCKRI Symposium 2, 13th sinkhole conference, p. 89–101. https://doi.org/10.5038/9780979542275.1117

Hyatt, J.A., and Jacobs, P.M., 1996, Distribution and morphology of sinkholes triggered by flooding following Tropical Storm Alberto at Albany, Georgia, USA: Geomorphology, v. 17, p. 305–316. https://doi.org/10.1016/0169-555X(96)00014-1

Intrieri, E., Fontanelli, K., Bardi, F., Marini, F., Carlà, T., Pazzi, V., Di Filippo, M., and Fanti, R., 2018, Definition of sinkhole triggers and susceptibility based on hydrogeomorphological analyses: Environmental Earth Sciences, v. 77, p. 4. https://doi.org/10.1007/s12665-017-7179-3

Jennings, I.B., 1959, Geology and site investigations in the vicinity of the Goliath Portland cement Company's works, Railton, Tasmania. Part 2: Mineral Resources Tasmania Report UR1960_046_61.

Jennings, I.B., 1960, Geology and site investigations in the vicinity of the Goliath Portland cement Company's works – Railton, Tasmania: Mineral Resources Tasmania Report TR4_62_90.

Jennings, I.B., 1961, Geological sequence in recent drilling near the Goliath Cement company's works – Railton. Mineral Resources Tasmania Report TR5_114_117.

Jia, L., Lujuan, L., Meng, Y., Wu, Y., Pan, Z., and Yin, R., 2018, Responses of cover-collapse sinkholes to groundwater changes: a case study of early warning of soil cave and sinkhole activity on Datansha Island in Guangzhou, China: Environmental Earth Sciences, v. 77, p. 488. https://doi.org/10.1007/s12665-018-7603-3

Jones, R., Cosgrove, R., Allen, J., Cane, S., Kiernan, K., Webb, S., Loy, T., West, D., and Stadler, E., 1988, An archaeological reconnaissance of karst caves within the southern forests region of Tasmania, September 1987: Australian Archaeology, v. 26, p. 1–23.

Jovanelly, T.J., 2014, Sinkholes and a disappearing lake: Victory Lake case study: Journal of Cave and Karst Studies: v. 76, p. 217–229. https://doi.org/10.4311/2012ES0272

Kaufmann, O., and Quinif, Y., 2002, Geohazard map of cover-collapse sinkholes in the 'Tournaisis' area, southern Belgium: Engineering Geology, v. 65, p. 117–124. https://doi.org/10.1016/S0013-7952(01)00118-1

Kaufmann, G., and Romanov, D., 2016, Structure and evolution of collapse sinkholes: combined interpretation from physico-chemical modelling and geophysical field work: Journal of Hydrology, v. 540, p. 688–698. https://doi.org/10.1016/j.jhydrol.2016.06.050

Khanlari, G., Heidari, M., Momeni, A.A., Ahmadi, M., and Beydokhti, A.T., 2012, The effect of groundwater overexploitation on land subsidence and sinkhole occurrences, western Iran: Quarterly Journal of Engineering Geology and Hydrogeology, v. 45, p. 447–456. https://doi.org/10.1144/qjegh2010-069

Kiernan, K., 1989, Karst, Caves and Management at Mole Creek, Tasmania. A report to the Forestry Commission and National Parks & Wildlife Service, Tasmania 1984: Department of Parks, Wildlife and Heritage Occasional Paper no.22. Forestry Commission, Hobart, 140 p.

Kiernan, K., 1990, Underground drainage at Mole Creek, Tasmania: Australian Geographical Studies, v. 28, p. 224–239. https://doi.org/10.1111/j.1467-8470.1990.tb00614.x

Kiernan, K., 1993, The Exit Cave Quarry: Tracing waterflows and resource policy evaluation. Helictite, v. 31, p.27–42.

Kiernan, K., 1995a, Karst management in commercial forests, *in* Spate, A.P., Bell. P., and Henderson, K. eds: Cave Management in Australasia: v. 7, p. 37–40.

Kiernan. K., 1995b, An atlas of Tasmanian Karst v. 1–2: Research Report No.10, Tasmanian Forest Research Council, Inc. Hobart, Tasmania.

Kiernan, K., Eberhard, R., and Shannon, C.H.C., 1994, Further hydrogeological investigations of the Mill Creek-Kansas Creek area, Northern Tasmania: Tasforests, v. 6, p. 7–22.

Kiernan, K. 2002, Sinkhole Manual: Forest Practices Authority, Hobart.

Knöll, P., and Scheytt, T., 2018, A tracer test to determine a hydraulic connection between the Lauchert and Danube karst catchments (Swabian Alb, Germany): Hydrogeology Journal, v. 26, p. 429–437. https://doi.org/10.1007/s10040-017-1678-x

Kobal, M., Bertoncelj, I., Pirotti, F., Dakskobler, I., and Kutnar, L., 2015, Using lidar data to analyse sinkhole characteristics relevant for understory vegetation under forest cover—Case study of a high karst area in the Dinaric Mountains: PLOS ONE 10(3): e0122070. https://doi.org/10.1371/journal.pone.0122070

LaMoreaux, P.E., Powell, W.J., and LeGrand, H.E., 1997, Environmental and legal aspects of karst areas: Environmental Geology, v. 29, p. 23–26. https://doi.org/10.1007/s002540050100

Langer, W.H., 2001, Potential environmental impacts of quarrying stone in karst: a literature review: US Department of the Interior, US Geological Survey, Open-File Report OF-01-0484. https://doi.org/10.3133/ofr01484

Lauber, U., Ufrecht, W., and Goldscheider, N., 2014, Spatially resolved information on karst conduit flow from in-cave dye tracing: Hydrology and Earth System Sciences, v. 18, p. 435–445. https://doi.org/10.5194/hess-18-435-2014

Lipar, M., Stepišnik, U., and Ferk, M., 2019, Multiphase breakdown sequence of collapse doline morphogenesis: an example from Quaternary aeolianites in Western Australia: Geomorphology v. 327, p. 572–584. https://doi.org/10.1016/j.geomorph.2018.11.031

Liu, J., Fu, G., Song, X., Charles, S.P., Zhang, Y., Han, D., and Wang, S., 2010, Stable isotope compositions in Australian precipitation: Journal of Geophysical Research, v. 115, D23, https://doi.org/10.1029/2010JD014403

Lolcama, J.l., Cohen, H.A., and Tonkin, M.J., 2002, Deep karst conduits, flooding, and sinkholes: lessons for the aggregates industry: Engineering Geology, v. 65, p. 151–157. https://doi.org/10.1016/S0013-7952(01)00122-3

Marcus, W.A., Roberts, K., Harvey, L., and Tackman, G., 1992, An evaluation of methods for estimating Manning's n in small mountain streams: Mountain Research and Development, v. 12, p. 227–239. https://doi.org/10.2307/3673667

Martinotti, M.E., Pisano, L., Marchesini, I., Rossi, M., Peruccacci, S., Brunetti, M.T., Melillo, M., Amoruso, G., Loiacono, P., Vennari, C., Vessia, G., Trabace, M., Parise, M., and Guzzetti, F., 2017, Landslides, floods and sinkholes in a karst environment: the 1–6 September 2014 Gargano event, southern Italy: Natural Hazards and Earth System Sciences, v. 17, p. 467–480. https://doi.org/10.5194/nhess-17-467-2017

Matthews. W.L., Hudspeth. J.W., and Donaldson, R.C., 1983, Sinkholes at Railton railway station: Tasmania Department of Mines, v. 39, p. 1–6.

McClenaghan, M.P., 2003, Railton Sheet 4442, Digital Geological Atlas 1: 25000 series: Mineral Resources Tasmania' Hobart.

McIntosh, P.D., Eberhard, R., Slee, A., Moss P., Price D.M., Donaldson P., Doyle R., and Martins J., 2012, Late Quaternary extraglacial cold-climate deposits in low and mid-altitude Tasmania and their climatic implications: Geomorphology, v. 179, p. 21–39. https://doi.org/10.1016/j.geomorph.2012.08.009

Miles, K.E., Hubbard, B., Quincey, D.J., Miles, E.S., Irvine-Fynn, T.D.L., and Rowan, A.V., 2019, Surface and subsurface hydrology of debris-covered Khumbu Glacier, Nepal, revealed by dye tracing, Earth and Planetary Science Letters: v. 513, p. 176–186. https://doi.org/10.1016/j.epsl.2019.02.020

North, L.A., van Beynen, P.E., Parise, M., 2009, Interregional comparison of karst disturbance: West-central Florida and southeast Italy: Journal of Environmental Management, v. 90, p. 1770–1781. https://doi.org/10.1016/j.jenvman.2008.11.018

Noury, G., Perrin, J., Li-Hua Luu, L-H., Philippe, P., and Gourdier. S., 2018, Role of floods on sinkholes occurrence in covered karst terrains: case study of Orléans area (France) during the 2016 meteorological event and perspectives for other karst environments:15th Multidisciplinary Conference on Sinkholes and the Engineering and Environmental Impacts of Karst, April 2018, Shepherdstown, W.Va. https://doi.org/10.5038/9780991000982.1014

O'Driscoll, M.A., and DeWalle, D.R., 2006, Stream–air temperature relations to classify stream–ground water interactions in a karst setting, central Pennsylvania, USA: Journal of Hydrology, v. 329, p. 140–153. https://doi.org/10.1016/j.jhydrol.2006.02.010

Osborne, R.A.L., 1994, Caves, cement, bats, and tourists: karst science and limestone resource management in Australia, Journal and Proceedings, Royal Society of New South Wales, v. 127, p. 1–22.

Pan, Z., Jiang, X., Lei, M., Guan, Z., Wu, Y., and Gao, Y., 2018, Mechanism of sinkhole formation during groundwater-level recovery in karst mining area, Dachengqiao, Hunan province, China: Environmental Earth Sciences: v. 77, p. 799. https://doi.org/10.1007/s12665-018-7987-0

Parise, M., 2015, Karst geo-hazards: causal factors and management issues: Acta Carsologica, v. 44, p. 401–414. https://doi.org/10.3986/ac.v44i3.1891

Parise, M., 2016, Modern resource use and its impact in karst areas – mining and quarrying: Zeitschrift für Geomorphologie, v. 60 (Suppl. 2), p, 199–216. https://doi.org/10.1127/zfg_suppl/2016/00312

Parise, M., and Pascali, V., 2003, Surface and subsurface environmental degradation in the karst of Apulia (southern Italy): Environmental Geology, v. 44, 247–256. https://doi.org/10.1007/s00254-003-0773-6

Parise, M., Pisano, L., and Vennari, C., 2018, Sinkhole clusters after heavy rainstorms: Journal of Cave and Karst Studies, v. 80, p.28–38. https://doi.org/10.4311/2017ES0105

Pepe, M., and Parise, M., 2014, Structural control on development of karst landscape in the Salento Peninsula (Apulia, SE Italy): Acta Carsologica, v. 43, p. 101–114. https://doi.org/10.3986/ac.v43i1.643

Polk, J.S., North, L.A., Federico, R., Ham, B., Nedvidek, D., McClanahan, K., Kambesis, P., and Marasa, M.J., 2015, Cars and Karst: Investigating the National Corvette Museum Sinkhole, NCKRI Symposium 5, 14th sinkhole conference, p. 477–481. https://doi.org/10.5038/9780991000951.1079

Poulain, A., Watlet, A., Kaufmann, O., Van Camp, M., Joude, H., Mazzilli, N., Rochez, G., Deleu, R., Quinif, Y., and Hallet, V., 2018, Assessment of groundwater recharge processes through karst vadose zone by cave percolation monitoring: Hydrological Processes, v. 32, p. 2069–2083. https://doi.org/10.1002/hyp.13138

Ray, G.A., and Megahan, W.F., 1979, Measuring cross sections using a sag tape: a generalized procedure: General Technical Report INT–GTR–47. Ogden, UT: US Department of Agriculture, Forest Service, Intermountain Forest and Range Experiment Station, v. 12, p. 47.

Scanlon, B.R., Healy, R.W., and Cook, P.G., 2002, Choosing appropriate techniques for quantifying groundwater recharge: Hydrogeology Journal, v. 10, p. 18–39. https://doi.org/10.1007/s10040-001-0176-2

Sharples, C., 2002, Karst survey: Settlement block, Florentine valley (explanatory notes and data dictionary): Report for Norske Skog, New Norfolk, Tasmania.

Sharples, C., 2018, A dye tracing experiment at the Settlement: looking for a minor master cave in the Florentine Valley: Speleo Spiel (Journal of the Southern Tasmanian Caverneers), v. 425, p.12–14.

Siska, P.P., Goovaerts, P., and Hung, I.K., 2016, Evaluating susceptibility of karst dolines (sinkholes) for collapse in Sango, Tennessee, USA: Progress in Physical Geography, v. 40, p. 579–597. https://doi.org/10.1177/0309133316638816

Slee, A., McIntosh, P., Webb, J., Sharples, C., and Williams, K., 2019, Managing geomorphic values within Tasmanian plantations on karst terrain: Australian Forestry, v. 82, p. 127–138. https://doi.org/10.1080/00049158.2019.1656704

Soliman, M.H., Perez, A.L., Nam, B.H., and Ye, M., 2018, Physical and numerical analysis on the mechanical behaviour of cover-collapse sinkholes in central Florida: 15th sinkhole conference NCKRI Symposium, v. 7, 405–415. https://doi.org/10.5038/9780991000982.1040

Tharp, T. M., 1999, Mechanics of upward propagation of cover-collapse sinkholes: Engineering Geology, v. 52, p. 23–33. https://doi.org/10.1016/S0013-7952(98)00051-9

Urich, P. B., 2002, Land use in karst terrain: review of impacts of primary activities on temperate karst ecosystems: Department of Conservation Wellington.

van Beynen, P.E., and Townsend, K.M., 2005, A disturbance index for karst environments: Environmental Management, v. 36, p. 101–116. https://doi.org/10.1007/s00267-004-0265-9

Vigna, B., and Banzato, C., 2015, The hydrogeology of high-mountain carbonate areas: an example of some Alpine systems in southern Piedmont (Italy): Environmental Earth Sciences, v. 74, p. 267–280. https://doi.org/10.1007/s12665-015-4308-8

Waltham, T., 2008, Sinkhole hazard case histories in karst terrains: Quarterly Journal of Engineering Geology and Hydrogeology, v. 41, p. 291–300. https://doi.org/10.1144/1470-9236/07-211

Water Management Act 1999. https://www.legislation.tas.gov.au/view/whole/htmL/inforce/current/act-1999-045 [accessed July 2, 2019].

Yan, C., Luo, G., Wang, Y., Chen, M., Zhan, Q., Wan, G., Chen, X., Zheng, G., and Guo, J., 2008, Compressive structural control on karst development, *in* Yuhr, L.B., Alexander, E.C., and Beck, B.F., eds: Sinkholes and the Engineering and Environmental Impacts of Karst, p. 54–61. https://doi.org/10.1061/41003(327)6

Zhou, W., and Beck, B.F., 2008, Management and mitigation of sinkholes on karst lands: an overview of practical applications: Environmental Geology, v. 55, p. 837–851. https://doi.org/10.1007/s00254-007-1035-9

Zhou, W., and Lei, M., 2018, Summary editorial for karst hydrogeology: advances in karst collapse studies: Environmental Earth Sciences, v. 77, p. 803. https://doi.org/10.1007/s12665-018-7990-5

Seriwat Saminpanya and Nopporn Denkitkul. Micromorphology, mineralogy, and geochemistry of sediments at the Tham Lod rock shelter archaeological site in Mae Hong Son, Thailand: suggestions of a late Pleistocene climate.. *Journal of Cave and Karst Studies*, v. 82, no. 1, p. 51-68. DOI:10.4311/2019ES0111

MICROMORPHOLOGY, MINERALOGY, AND GEOCHEMISTRY OF SEDIMENTS AT THE THAM LOD ROCK SHELTER ARCHAEOLOGICAL SITE IN MAE HONG SON, THAILAND: SUGGESTIONS OF A LATE PLEISTOCENE CLIMATE

Seriwat Saminpanya[1,C] and Nopporn Denkitkul[2]

ABSTRACT

Sediments from an archaeological pit at the Tham Lod rock shelter in Mae Hong Son, Thailand, reveal sparse palaeoenvironment and palaeoclimate information in the north-western region of Thailand and Southeast Asia. This study is a pioneering work for the site. Micromorphological, mineralogical, and geochemical methods were applied for analyses. The sediment profile was divided into two zones: the upper 0–338 cm depth and the lower 338–450 cm depth. Intense chemical weathering occurred in the lower zone, indicated by low quantities of kaolinite and high chemical index of alteration (CIA, 64.55–73.36%), reflecting greater humidity. The upper zone yielded mild CIA (<47.21%) and contained ubiquitous smectite, indicating drier conditions. Overall sediments (along the profile, 0–450 cm depth) were affected by leaching and thin section analyses suggested a wet/dry cycle during diagenesis under humid tropical conditions. Micromorphological and geochemical analyses indicated that mudstone, sandstone, and limestone were major parent materials of sediments deposited mainly in a fluvial environment in the lower zone, which changed to a colluvial environment in the upper zone. The palaeoclimate during 12,770–33,340 yr BP was in the Last Glacial Maximum Period, characterized by drier and cooler than the present climate. The period ≥33,340 yr BP was wet and cool. Evidence of prehistoric human occupation, including bone and charcoal fragments, appeared in sediments in the upper zone, suggesting animal hunting for survival.

Introduction

The rock shelter at Tham Lod in Mae Hong Son, Thailand has been extensively studied by many scholars in particular of archaeology and geoarchaeology (e.g., Khaokhiew, 2003; Marwick and Gargan, 2011; Marwick, 2013; Chitkament et al., 2016). However, valuable information which can be retrieved from the site is palaeoclimate information, which is in scarce in the studied region. Marwick and Gargan (2011) focused on oxygen isotope sequence of bivalves from the site and addressed the Pleistocene monsoon variability in northwestern Thailand. They demonstrated that the area was under the conditions of wet during ~35,000–20,000 yr BP and dry during ~20,000–12,000 yr BP. The monsoon-climate variability for the more recent period, back to ~400 yr BP, of the region was also derived from stalagmites and tree-rings (Clemens et al., 2010; Muangsong et al., 2014). Alternatively, we have been interested in a meaningful proxy, the sediment of the site, which records the palaeoclimatic conditions to the region during the late Pleistocene.

Unconsolidated sediment of the site is a crucial candidate to be studied in more detail and from a different viewpoint for valuable palaeoclimate data. A focus on analyzing sediment samples from the pit profiles can help reveal some information about the palaeoclimate and palaeoenvironment. The multiple techniques used in this research have been used to interpret the local and regional precipitation and humidity conditions (Sheldon and Tabor, 2009). The results of this study are beneficial to complete the data inventory of Thailand and Southeast Asia (SEA) and to reveal the palaeoclimate in terms of understanding the interrelationship between the prehistoric human habitat and the palaeoclimate in the late Pleistocene Epoch.

Materials and Methods

Micromorphological, mineralogical, and geochemical contexts are used in this work. Depositional sediments can record evidence or processes (Selley, 1985) that can be observed via micromorphology following the guidelines of Stoops et al. (2010). The aspect of geochemistry regarding the chemical processes of alteration, elemental signatures, and mineralogy, including clay-based minerals, can reveal the weathering intensity, sediment provenance, climatic environments, and anthropogenic input to the site.

Study area

The Tham Lod rock shelter site is located in the well-known archaeological pit in the Pang Mapha district in Mae Hong Son Province, Thailand. The shelter is located in a karst area at latitude 19°34′03″ N and longitude 98°16′46″ E, with an elevation of ~640 m above mean sea level (Fig. 1). The pit is situated in a boundary of the Tham Lod Natural and Wildlife Education Center. The details of its physical characteristics have already been reported by Marwick (2013) and Chitkament et al. (2016).

[1]Department of General Science, Faculty of Science, Srinakharinwirot University, Bangkok 10110, Thailand
[2]Faculty of Environment and Resource Studies, Mahidol University, Salaya, Nakhon Pathom 73170, Thailand
[c]Corresponding author: seriwat@g.swu.ac.th

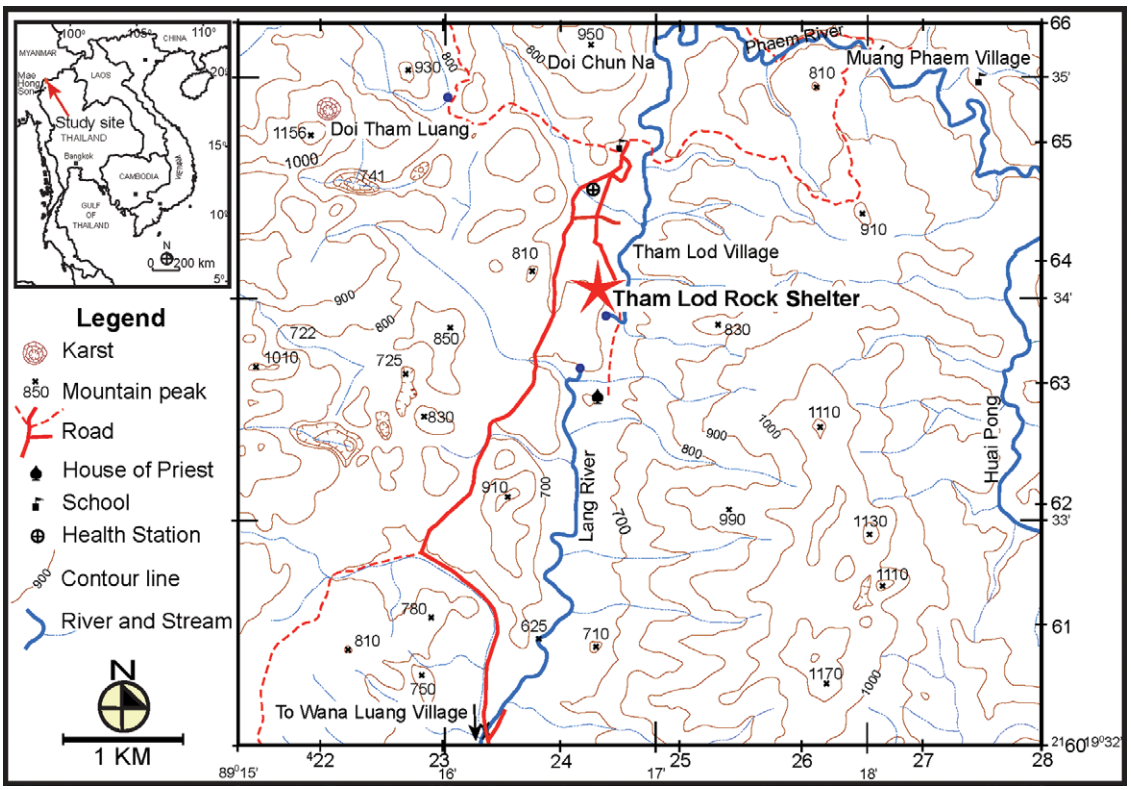

Figure 1. Location of Tham Lod rock shelter (adapted from a topographic map by the Royal Thai Survey Department, 1999).

The regional geology of the area surrounding the site consists of rocks composed of Silurian-Devonian phyllite and quartzite, Carboniferous clastic and chemical sedimentary rocks, Permian limestone, and Triassic granite (Department of Mineral Resources, Thailand, 2017). Permian limestone hosts the site and displays typical karst morphology, including rock shelters, caves, sinkholes, and polje. The rock shelter is situated near the Lang River, which contains gravel from different kinds of rocks, e.g., granite, andesite, chert, sandstone, shale, quartzite, and flint. The shelter (Fig. 2a) is the wall of an open doline basin filled with unconsolidated fluvial sediments of the Lang River located south of the basin (Khaokhiew, 2003). Some reports have covered this site; e.g., Chitkament et al. (2016) described the stone artifacts of Hoabinhian culture, typified by sumatralith stones. The site is very significant in terms of its two human burials in the late Pleistocene Epoch (Marwick, 2013).

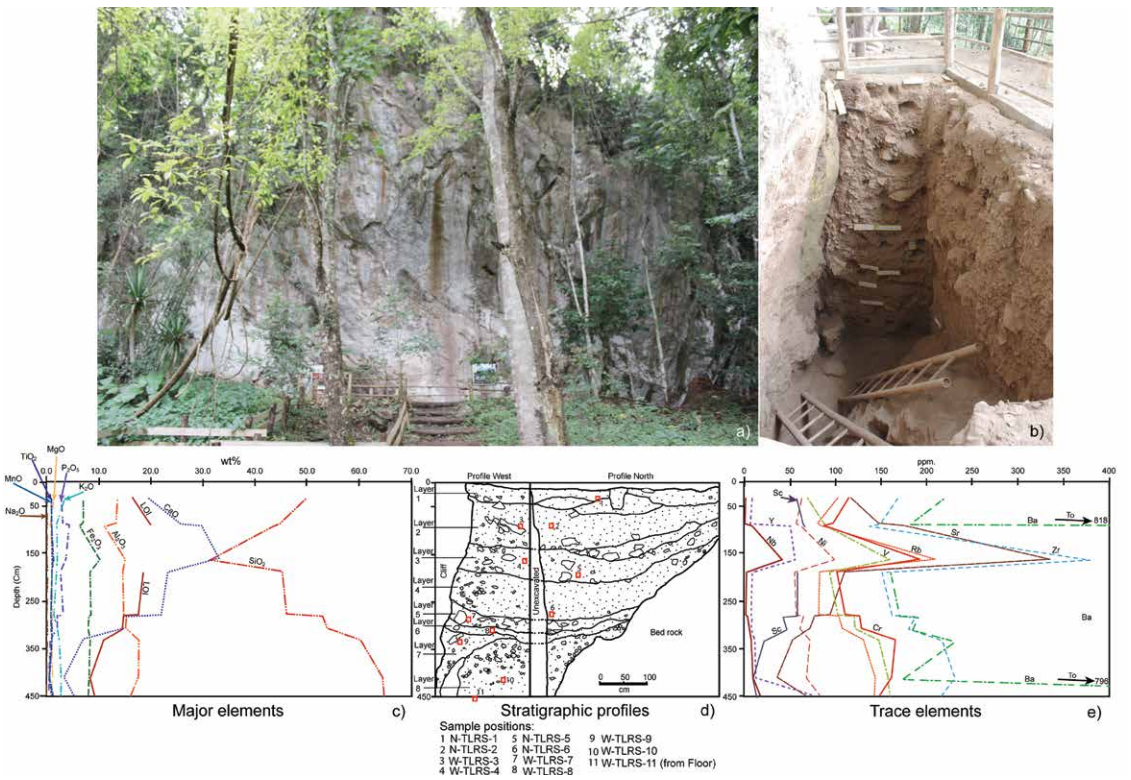

Figure 2. a) Tham Lod rock shelter, Pang Mapha district, Mae Hong Son Province, south view; b) profiles of the archaeological excavation pit under the shelter, as seen, the host limestone wall (left) profile west (middle) and profile north (right); c) and e) plots of major and trace elements along the profile in d).

Sample collection

Unconsolidated sediment samples were collected from the profiles of an archaeologically excavated pit (4.5 meters deep) under the Tham Lod rock shelter. Eight layers of sediment were clearly designated based on different colors, textures,

grain sizes, and archaeological materials observed in the field (Fig. 2d). Eleven samples weighing one or two kilograms each were collected and placed in plastic bags, and geochemical, grain size, and X-ray diffraction (XRD) analyses were performed. After this work, eight samples for polished thin section preparation were collected using Kubiena boxes. The field observation and sample collection were performed in November 2013 and the samples were stored in the dry and cool condition of the laboratory.

Field observations and descriptions were performed using the naked eye and a 10X loupe. A binocular microscope was used in a laboratory to observe the samples in more detail with the Munsell soil-color charts (Munsell Color (Firm), 2012) for color description. The particle size analysis employed the classic hydrometer method (Bedaiwy, 2012). The polished thin sections were examined under a polarizing microscope following the guidelines of Stoops et al. (2010). The XRD Philips X'Pert with MPD software was assigned to qualitatively analyze clay minerals with sample preparation following the standard method of Jackson (2005) by using ethylene glycol treatment before launching the XRD analysis. The chemical composition of the samples was obtained by X-ray fluorescence (XRF) on a Philips Magix Pro PW 2400 instrument with a sequential wavelength dispersive spectrometer, and sixteen international standards were run from the U.S. Geological Survey Reference Material (AGV-2, BCR-2, BHVO-2, BIR-1, DNC-1, DTs-2, GSP-2, QLO-1, RGM-1, STM-1, and W-2), International Atomic Energy Agency (SOIL-5 and SOIL-7), and British Chemical Standards (No. 368, No. 393, and No. 372/1). The XRF sample preparations included fused beads (a mixture of sample+lithium bromide+lithium) for major element analysis and pressed powders (a mixture of sample+boric acid+XRF multi-mix) under pressure of eighteen tons for trace element analysis. The loss on ignition (LOI) was determined by weight loss after heating approximately 1.0 grams of the powdered sample at 1,000 °C for 2 hours. LOI is used to estimate organic and carbonate contents of the studied samples. Organic matter is oxidized at ~500–550 ºC and then carbonate will be combusted at 800 − 1000 ºC (Dean, 1974; Bengtsson and Enell, 1986; Heiri et al., 2001). The intensity of chemical weathering of sediments is illustrated by the chemical index of alteration (CIA) and we used an equation proposed by Nesbitt and Young (1982) as follows:

$$\mathrm{CIA} = 100 \times \frac{\mathrm{Al_2O_3}}{\mathrm{Al_2O_3} + \mathrm{CaO} + \mathrm{K_2O} + \mathrm{Na_2O}}$$

The principle of the equation relates to feldspar weathering by hydration and clay mineral products and/or the presence of alkali elements (K and Na) in sediments. An elevated Al content may be linked with increasing clay content and decreasing Ca, K, and Na contents, causing higher CIA values (Nesbitt and Young, 1982). The dates for the sediments were derived from Marwick and Gagan (2011), where this issue was discussed in detail.

Results

Field and binocular observations

The sediments were mainly allogenic, and smaller amounts of rocks were present. Layers 1 and 2 contain two human burials at 50 and 80 cm depths, respectively, with shells and artifacts, such as glass beads, potsherds, and metals (Marwick and Gagan, 2011). Layer 3 contains clay and silt particles with charcoal, calcretes, and quartzite and limestone pebbles. Layers 4 and 5 contain more abundant animal bones and stone tools, while layers 6 and 7 have slight amounts of these materials. Layer 8 has no archaeological objects.

Based on field observations, the lower part, especially layers 7 and 8, contains abundant pebbles and cobbles, mainly composed of sandstone. Layers 1 to 6 have less abundant pebbles and cobbles but also include limestone fragments fallen from the cliff, calcretes, travertine fragments, mica grains, and bone and charcoal fragments. The field descriptions are shown in Table 1.

Observations via binocular microscopy show that the color of the sediment matrix is brown (7.5YR4/4). Most samples show a blocky aggregate structure. Angular limestone fragments and subrounded quartz grains appear in most of the samples. A description of the matrix of eight samples is shown in Table 2.

Particle size analysis

The particle size analysis from eleven samples is plotted in a diagram in Figure 3. Layers 1 and 3 contain more sand particles, and the number of sand particles decreases in the deeper parts (layers 6, 7, 8, 9, and 11).

Thin section observation

The matrix of the profile was inspected via thin sections. Most show a loose arrangement and poorly-sorted fabrics. Brown clay aggregates are observed and contain inclusions of quartz grains. Fe/Mn-oxide nodules are abundant in almost all samples. The quartz grains are poorly sorted, and bone fragments appear in some samples. More detailed descriptions are presented in Table 3 and Figure 4.

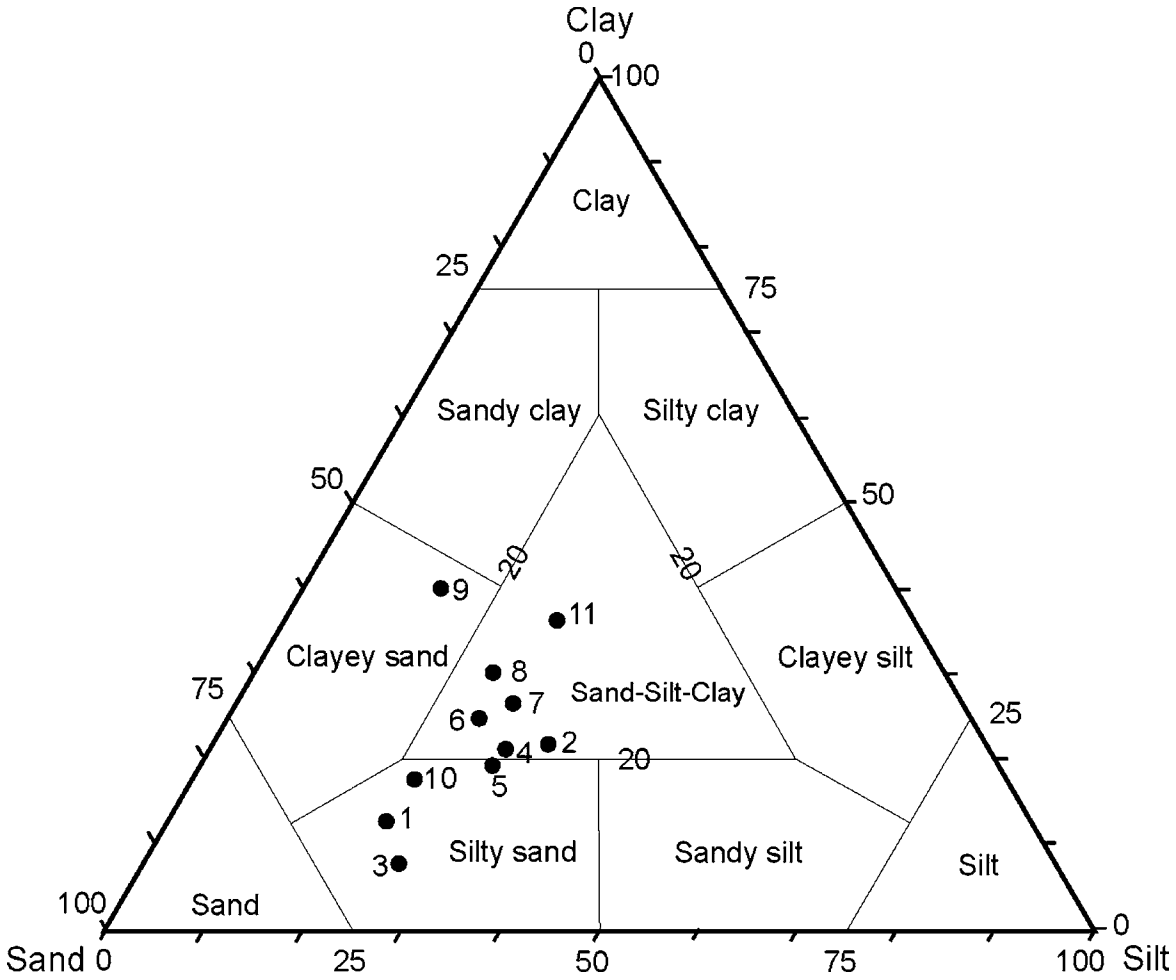

Figure 3. Ternary diagram (from Shepard, 1954) showing particle-size distribution of 11 samples. [Sample ID/ Depth: 1) N-TLRS-1/ 35 cm; 2) N-TLRS-2/ 88 cm; 3) W-TLRS-3/ 93 cm; 4) W-TLRS-4/ 164 cm; 5) N-TLRS-5/ 190 cm; 6) N-TLRS-6/ 280 cm; 7) W-TLRS-7/ 283 cm; 8) W-TLRS-8/ 309 cm; 9) W-TLRS-9/ 333 cm; 10) W-TLRS-10/ 412 cm; 11) W-TLRS-11/ 450 cm].

Mineralogy

The qualitative XRD results show the amounts of clay minerals (kaolinite, illite, and smectite), quartz, and calcite in the samples (Fig. 5). Layers 7 and 8 contain higher levels of kaolinite, but layers 1 to 6 have trace amounts of this mineral. In contrast, smectite shows dominant or large amounts in the upper layers, especially layers 1 to 4, and then decreases to small quantities in the lower layers 7 and 8.

Geochemistry

Based on the differences in element contents in the profile, the profile can be divided into two zones (upper from 0–338 cm depth and lower from 338–450 cm depth) (Fig. 2). All of the element contents are presented in Table 4.

Discussion

Micromorphology, mineralogy, and geochemistry of the Tham Lod site in its archaeological regional context and palaeoclimate are discussed in this section.

Micromorphology

The appearances of the sediments presented in Figure 4 and the description of sediment observations in Tables 1–3 indicate that most clasts are poorly sorted, suggesting a fluvial environment with a strong current in terms of deposition, especially in the lower zone. Some layers consist of a variety of grain sizes, with pebbles and cobbles of various rock types. The gravel is mixed with reddish brown and yellowish brown clay, and the coarse particles are poorly sorted. The upper zone reflects the fluvial environment, together with the effects of air-fall materials, e.g., dust and rock debris, and anthropogenic sediments. The upper zone contains large angular limestone fragments fallen from the overhanging wall of the shelter. This feature suggests a dominantly colluvial environment. The lower zone has poorly sorted clastic sediments and aggregates with various particle sizes from clay to sand with mostly sub-angular to angular shapes, as well as ubiquitous pebbles and cobbles. This combination suggests that the water currents were very strong under the condition of the channel entrenchment of the Lang River, and during the flooding period of the river, its sediments would be disturbed. These sediments represent the fluvial facies associated with the palaeo-river Lang, now located approximately 100 meters north of the site. The transition boundary between these two depositional environments took place at approximately 32,000 yr BP (Marwick and Gagan, 2011).

Wet/dry features chiefly involve water retention in sediments and the reduction and oxidation of Fe/Mn by chemical

Table 1. Description of sediments from field observations.

Layer	Upper to Lower Limits of Layer, cm[a]	Description
Layer 1 (top layer)	0–72	The matrix is mainly composed of clay and silt particles. The reddish clay matrix incorporates very fine mica grains. Boulders of quartzite are well rounded and have low sphericity.
Layer 2	72–141	The matrix is composed of small pieces of charcoal and bone with clay, plant roots, mica grains (1.5 mm across), and white materials. Very angular limestone gravel with a maximum size of 7×5×1.5 cm is present. Small pieces of broken stalagmites and stalactites are found. In the upper part of the layer are platy limestone fragments and a sandstone pebble (10×20×30 cm).
Layer 3	141–207	The matrix is composed of clay and silt particles with an inclusion of charcoal. Calcretes have irregular shapes (5×4×3 cm; 3×3.6×1.6 cm). Unknown green materials are present and a rounded quartzite pebble (10×30×15 cm) with low sphericity. Angular limestone pebbles (25×30×25 cm) with low sphericity are found.
Layer 4	207–288	In a matrix of clay and silt particles are abundant small pieces of bones, some calcretes (max. 3 mm across) and small numbers of mica grains (< 1%). Black materials, probably charcoal, also appear. Well-rounded quartzite pebbles (max. 15×7×9 cm) with low sphericity and angular limestone pebbles (max. 10×15×5 cm) are found.
Layer 5	288–317	The yellow matrix is composed mainly of clay and silt with less than 1% muscovite grains (<1 mm across). Clastic materials in this layer are coated with lime. Some calcretes are found. Angular gravel is abundant (> 80%) with an average size of 3×5×4 cm. A very angular pebble of slate (1.5×4×2.5 cm) with low sphericity is present.
Layer 6	317–338	The matrix is composed of mainly clay particles with white bone fragments and angular to subangular quartz gravel with low sphericity (max. 3×1.5×2.5 cm) are found. Black angular pebbles of travertine (max. 8×5×4 cm) with low sphericity are present.
Layer 7	338–450	The matrix is composed of clay, quartz sand, and marl rock. Clay with grey-black spots is present in lenses (20×70 cm) along with very angular black chert granules (max. 2×1×0.5 cm). A layer of quartzite pebbles (up to 2.5×4×3 cm), which are very angular to well-rounded and have low sphericity, is found.
Layer 8 (bottom layer)	338–450+	This layer is divided into 2 sublayers: 1) Upper layer – The matrix is composed of clay with sand-size mica and quartz particles. The layer contains well-rounded and moderately spherical pebbles and cobbles (max. 7×6×18 cm) of mainly grey sandstone (~80%). 2) Lower layer – The layer contains brown-red clay, angular to rounded quartz sand, granules (<2%), and white mica grains (~1 mm across).

[a] Note that layers are nonparallel. The numbers shown here represent the maximum thicknesses.

processes and include two main features: Mn-Fe-oxide and redox pedo-features. The first feature refers to Fe/Mn-oxides in sediments such as impregnated Fe/Mn nodules (Blokhuis et al., 1969; Kabakchiev and Galeva, 1973; Tsuji et al., 1975; Sleeman and Brewer, 1984; Blokhuis et al., 1990; Tawornpruek et al., 2006). The first feature found in the thin sections is the presence of Fe/Mn coatings, Fe/Mn hypocoatings, and Mn nodules (Figs. 4d, 4g). These features indicate the conditions of humidity, wet/dry cycles and the leaching process during diagenesis at the study site. The existence of the blocky and granular textures of clay aggregates, as well as oxic materials in almost all samples, indicate that the sediments were in the pedogenic process of clay cementation, and the water availability in the sediments implies a humid climate. The calcitic crystallitic b-fabric features in most samples are derived from limestone fragments by solutions dissolved from the limestone host rock of the shelter, percolated through the voids and cavities and then precipitated as calcretes during diagenesis. This interpretation supports the hypothesis that after their deposition, sediments were subjected to alternately wet and dry conditions. The abundant limestone fragments, calcretes, and calcitic crystallitic b-fabric features in the upper zone layers correspond to high CaO contents and high LOI (Santisteban et al., 2004). LOI shows higher values in the upper zone, which suggests that the upper zone was affected by a higher rate of deposition by air-fall particles.

The richness in oxic materials (e.g., Fe/Mn-oxides) represents water retention and high leaching in sediments. Oxic materials and microstructure aggregates are found at depths between 288 and 450 cm (samples W-TLRS-7, 8, 9, 10, and 11). The aggregates are cemented by clay and silt particles. From the grain size analyses, clay fractions dominate in these samples (26.8%, 29.8%, 39.8%, 17.8%, and 36.2%, respectively). Sample W-TLRS-10 (at 412 cm depth) shows

Table 2. Description of sediment samples from observations via a binocular microscope.

Sample/Layer	Upper to Lower Limits of Layer, cm[a]	Depth of Sampling, cm	Description
N-TLRS–1 (Layer 1)	0–72	35	The colour of the layer is brown (7.5YR4/4) with loose arrangement of subangular to well-rounded quartz grains. Blocky aggregations of soil and muscovite grains (up to 3×1 mm) are found.
N-TLRS–2 (Layer 2)	72–141	88	Blocky aggregations of soil and loose arrangements poorly sorted coarse grains of quartz are cemented by brown (7.5YR4/4) clay. Muscovite grains (~0.2–0.5 mm) and white limestone fragments (3×3 mm) are found.
N-TLRS–5 (Layer 3)	141–207	190	The matrix colour is brown (7.5YR4/4). Polycrystalline calcite aggregates (max. 7×9 mm) are found. Blocks with angular and low sphericity limestone fragments (8×5 mm) are coated by reddish-brown clay.
N-TLRS–6 (Layer 4)	207–288	280	Quartz sand grains (max. 0.5×0.5 mm) are coated by brown clay (7.5YR4/4). Aggregations of carbonate nodules (max. 6×5 mm), white bone fragments and angular to subangular limestone fragments (max. 1.5×1 mm) are present.
W-TLRS–7 (Layer 5)	288–317	283	Brown (7.5YR4/4) clay forms the matrix. Angular calcite grains (max. 0.05 mm across) and limestone fragments (max. 0.2 mm across) with low sphericity are present.
W-TLRS–8 (Layer 6)	317–338	309	Brown (7.5YR4/4) clay forms the matrix. Angular limestone fragments (max. 7 mm across) with low sphericity and aggregated calcite crystals (~1.5 mm across) are present.
W-TLRS–9 (Layer 7)	338–450	333	The colour of aggregated clay in the matrix is brown (7.5YR4/4). Calcite grains (up to 1.5 mm across) are found. Angular limestone fragments (up to 3.5 mm across) with low sphericity are present.
W-TLRS–10 (Layer 8)	338–450+	412	The matrix consists of brown (7.5YR4/4) clay. A calcite crystal (0.5 mm across) and sub-rounded quartz grains (max. 1 mm across) are found. Aggregations of angular to sub-angular limestone fragments (max. 1.5 mm across) are present.

[a] Note that layers are nonparallel. The numbers shown here represent the maximum thicknesses.

reddish-brown clay cementation and clay aggregates that imply more extensive oxic materials formed during water retention in the lower zone than in the upper zone, which corresponds with their chemical index of alteration (CIA) and mean annual precipitation (MAP) values.

Although sample N-TLRS-6 (280 cm depth) is located in the upper zone, it shows distinctively intense clay aggregates, granular microstructures, and clay cementations. This combination is regarded as the effect of highly oxic materials. This sample is different from all other samples from the upper zone, indicating an interrupting period of more humid climate conditions. However, the other samples in the upper zone (N-TLRS-1, 2, W-TLRS-3, 4, and N-TLRS-5, from 0 to 207 cm depth) contain less oxic materials and an aggregate structure, suggesting that their deposition took place in a less humid environment.

Mineralogy

Kaolinite is a climatic indicator and the product of a high weathering intensity environment (Dixon, 1989; Alam et al., 2008; Hong et al., 2013). The results reveal that the kaolinite contents of the lower zone (from 338 to 450 cm depths in particular) are more prominent than those of the upper zone. This result suggests strong chemical weathering and more humid conditions or tropical/subtropical climates for the lower zone. The less distinctive kaolinite peaks, but not those of smectite, in the upper zone reflect a low level of chemical weathering and a drier environment (Fig. 5). Smectite, an alteration product of mafic minerals, is usually stable in arid, semi-arid, warm and dry or temperate climates (Pal, 2014). It can exist for a short period under humid or tropical conditions and can readily transform to kaolinite (Pal et al., 1989; Bhattacharyya et al., 1993). Smectite usually forms in poorly drained tropical to subtropical areas of low relief, marked by flooding in the humid seasons and substantial pore water retention in the soil during dry seasons (Chamley, 1989). These results strongly confirm that the upper zone of the Tham Lod rock shelter represents drier conditions.

Geochemistry

Although the profile has been subdivided into two zones as mentioned above, geochemical variations can be found at the depths of 93 cm, 164 cm, 412 cm, and 450 cm (Fig. 2). At 93 cm, there are relatively low Al_2O_3, Fe_2O_3, and TiO_2 contents but rich in P_2O_5, Y, Sr, and Ba contents. This layer contains abundant fragments of bone reflecting the high

Table 3. Description of thin section samples.

Sample/ Layer	Upper to Lower Limits of Layer, cm[a]	Depth of Sampling, cm	Description
N-TLRS-1/ (Layer 1)	0–72	35	The sediment is loose and poorly sorted. Quartz grains (<0.1–0.2 mm across, 40%), are mainly angular to sub-angular, but some are well-rounded. Nodules of quartz silt to sand particles are present. There are some muscovite grains (<1%) with prismatic angular and sub-rounded shapes. Calcite crystals (max. 1.2×1 mm, 50%) with blocky, lenticular, cylindrical, or tabular habits are present. The groundmass is composed of Fe-oxide coatings with yellow-brown colour (10%) on the nodules. The nodules are in aggregates with well-rounded shapes (~0.1 mm across). Bone and charcoal fragments are also found.
N-TLRS-2/ (Layer 2)	72–141	88	The texture is mainly loose and poorly sorted. Quartz grains (0.05–1.2 mm across) (40%) are mainly angular to well-rounded with low to high sphericity. Individual grains contain cracks, exhibit blocky, stubby, and prismatic habits and form aggregates (20%) with granular habit (clear reddish-brown colour). Quartz grains also appear as an inclusion in a nodule. Calcite crystals show b-fabric (~5%). Fe-oxide hypocoatings also appear in the aggregates (15%). Bone and quartzite fragments are found. Voids account for approximately 20%.
W-TLRS-5/ (Layer 3)	141–207	190	The sediment is mainly loose and poorly sorted. Quartz sand grains (~60%) are angular to well-rounded with moderate sphericity and have granular, blocky or cylindrical habits. Calcite crystals (<0.1–0.2 mm across, ~5%) show b-fabric, and some crystals (~0.3–0.2 mm across) have rhombohedral shape with cleavages. There are 35% cavities. Bone, sandstone, and limestone fragments are present.
N-TLRS-6/ (Layer 4)	207–288	280	The sediment is in loose aggregates with abundant plasma. The aggregates contain inclusions of clastic quartz grains. Cracks account for ~15% of voids. Bone fragments (~5%) display yellow-orange colour (PPL) with sizes ranging from <0.1 mm to 2.5×3 mm and are most abundant in this layer. The bone fragments are included in clay aggregates, and some are single grains. Fe-oxide hypocoatings occur in aggregates and on quartz grains. There are some Fe/Mn-oxide nodules (0.03–0.05 mm across, ~10%). The groundmass shows crystalline b-fabric due to the presence of calcite grains, and some calcite grains are observed inside aggregates. Quartz sand grains (0.5×0.6 mm across) and quartz silt grains (~70%) are poorly sorted and show blocky or prismatic habits.
W-TLRS-7/ (Layer 5)	288–317	283	The sediments display granular aggregates that contain zigzag voids (~10%). The ratio between oxic materials and carbonate materials is 40:60. Quartz sand grains (<0.05 to 1 mm across, 70%) with blocky habits show sub-angular to angular to well-rounded shapes, are poorly sorted and have moderate to high sphericity. Individual grains show fractures. Coarse-grained quartz particles are mostly angular to sub-angular. Bone fragments (max. 0.2×1 mm, <5%) are present in calcitic groundmass. The groundmass contains a mixture of calcitic and oxic materials. Fe-oxides (~5%) coatings on groundmass and aggregates are reddish-brown. Fe/Mn-oxide nodules (~10%) with sizes of ~1.5–0.05 mm across are present. Compacted and poorly sorted peds are of various sizes (from <0.1 mm to 0.6×0.8 mm), and some are found inside large clay aggregates and abundant plasma microstructures. Crumb structure is rich with clastic quartz inclusions.
W-TLRS-8/ (Layer 6)	317–338	309	Abundant plasma microstructures in both crystallitic b-fabric and undifferentiated b-fabric have proportions of 50:50 and contain Fe-oxides (~20%). Crumb structure is also present. Small curved and zigzag voids appear in the aggregates. Quartz grains (~30%) are mostly sub-angular to well-rounded and show blocky habits; sizes range from <0.05 mm to 0.1×0.2 mm. Some quartz grains are included in Fe/Mn-oxide nodules. Fe/Mn-oxide nodules (~30%) 0.05–0.1 mm across are present. Fe-oxides (~10%) coatings form on quartz grains, bone/charcoal fragments, and nodules. There are some calcite crystals and limestone fragments.
W-TLRS-9/ (Layer 7)	338–450	333	Clay aggregates are ~0.1–6 mm across. There are three types of b-fabric: 1) undifferentiated b-fabric; 2) crystallitic b-fabric; and 3) speckled b-fabric. Quartz grains (from <0.05 mm to 0.8×1.2 mm, 80%) are poorly sorted, well-rounded to angular; they have low to high sphericity and prismatic, blocky and vermiform habits. Mica grains (~5%), hypocoatings (~10%), and Fe/Mn-oxide nodules (~5%) are present. Fe-oxides coat clay aggregates and fill in fractures.

Table 3. (Continued).

Sample/ Layer	Upper to Lower Limits of Layer, cm[a]	Depth of Sampling, cm	Description
W-TLRS-10/ (Layer 8)	338–450	412	The groundmass shows plasma structures of calcitic crystallitic b-fabric and undifferentiated b-fabric. Quartz grains (<0.05 mm to 0.8×1.2 mm, 40%) are poorly sorted and angular to well-rounded with low to high sphericity and have prismatic, stubby, and vermiform habits. Mica grains (~5%), hypocoatings (~30%), and Fe/Mn-oxide nodules (~5%) are present. Voids (20%) are curved and zigzag. Speckled b-fabric is also found. Fe/Mn-oxides also appear in aggregates. Fe-oxides coat the aggregates and fill in the voids.

[a] Note that layers are nonparallel. The numbers shown here represent the maximum thicknesses.

value of P_2O_5. Sr^{2+} substitutes readily for Ca^{2+} of calcite in limestone fragments in the layer. Ba reflects the rich illite or feldspar in the sediments due to the substitution of Ba for K in these minerals. Ba can be rich in karst soils e.g., in Italy (Iacoviello and Martini, 2013). High Y probably comes along with carbonate sediments because of the similarity of the ionic size of Sr and Ca (Krauskopf and Bird, 1995).

At the depth of 164 cm, there are several maximum values of some major and trace elements (Fe_2O_3, MgO, MnO, CaO, Ni, V, Rb, Y, Nb, Cr, Sr, and Zr). The abrupt change in climate condition to the highest episode is characterized by the maximum estimated temperature (17.3 ºC). The sediment is rich in mafic elements (Fe/Mg/Mn/Ca/Ni/V/Cr), indicating the heavy input of the products of sediment from older mafic source rocks. Some trace elements can be explained in the same way as the 93 cm depth and they may be derived from the same mafic sources. Except for Rb, a large-ion lithophile, and Nb+Zr, a high field-strength element, tend to be derived from felsic rocks (Krauskopf and Bird, 1995) because these elements are lithophile and incompatible and they usually end up in the crust (or felsic environment). Zr also reflects the minerals zircon and monazite in quartz sand particles in the studied sediment. At the depth of 412 cm, and 450 cm the sediment was under the strong current, heavy rainfall, and high weathering rate, characterized by the SiO_2 rich and less CaO/LOI. Some traces are relatively high e.g., V, Rb, Y, Ba, and Zr. These traces have their sources and behaviors of substitution as explained before. For example, Ba manifests the feldspar and mica, and Zr mirrors the quartz sand in the sediments.

Weathering intensity

The triangular diagram (Fig. 6) shows that the upper zone sediments have CIA values lower than those of the lower zone. This result suggests that the lower zone was affected by a higher chemical weathering intensity than the upper zone. A trend of higher alteration increases with the depth along the profile. Samples at depths between 338 and 450 cm in the lower zone are very similar with high CIA values and greater amounts of kaolinite than in the lower zone. These results suggest the distinctive chemical weathering of sediments and a humid environment. The CIA values of the upper zone sediments at depths between 35 and 338 cm are lower; i.e., less chemical weathering and higher contents of smectite in this zone reflect a drier environment or lower humidity.

Palaeoprecipitation and palaeotemperatures

Palaeoprecipitation or palaeorainfall in terms of mean annual precipitation (MAP) was derived by excluding K content from the CIA (CIA–K). The values were estimated with the equation MAP (mm/yr) $= 221.1e^{0.0197\,(CIA\text{-}K)}$ from Maynard (1992) using the major elements of samples that were converted to moles before calculation. The MAP values report the maximum and minimum of 935 and 687 mm yr^{-1} in the lower zone, and of 447 and 309 mm yr^{-1} in the upper zone (Fig. 7). These results demonstrate that past precipitation in the younger upper zone was less than that in the lower/older zones. The levels of palaeorainfall before 33,340 yr BP were higher than in the younger period.

The palaeotemperature in degrees Celsius is estimated by the mean annual temperature (MAT) equation of Hamer et al. (2007), $T(°C) = 46.9C + 4$.

C or clayeyness refers to the Al/Si ratio after their wt% oxides (Al_2O_3 and SiO_2) have been converted to moles. The equation is applicable to a wide range of palaeotemperature estimates (Hamer et al., 2007). The Al/Si ratio is related to silicate parent material during Al accumulation (Retallack et al., 2000). The MAT and MAP values of the samples are displayed in Figure 7. The MAT had similar values throughout the profile (10.88–12.98 ºC), except for the maximum value at a depth of 164 cm (17.32 ºC). These values can provide useful data for the palaeoclimate to the area. More work needs to be conducted in detail to refine these equations for the study area.

Distinct and non-distinct humidity

The kaolinite and smectite contents, CIA and MAP values agree well and reveal that the lower zone sediment, representing ≥34,130 yr BP, experienced greater humidity than the upper zone, representing 12,270–33,340 yr BP (Marwick and Gagan, 2011). Kaolinite in the lower zone is at a higher level than in the upper zone, and the lower zones have low-

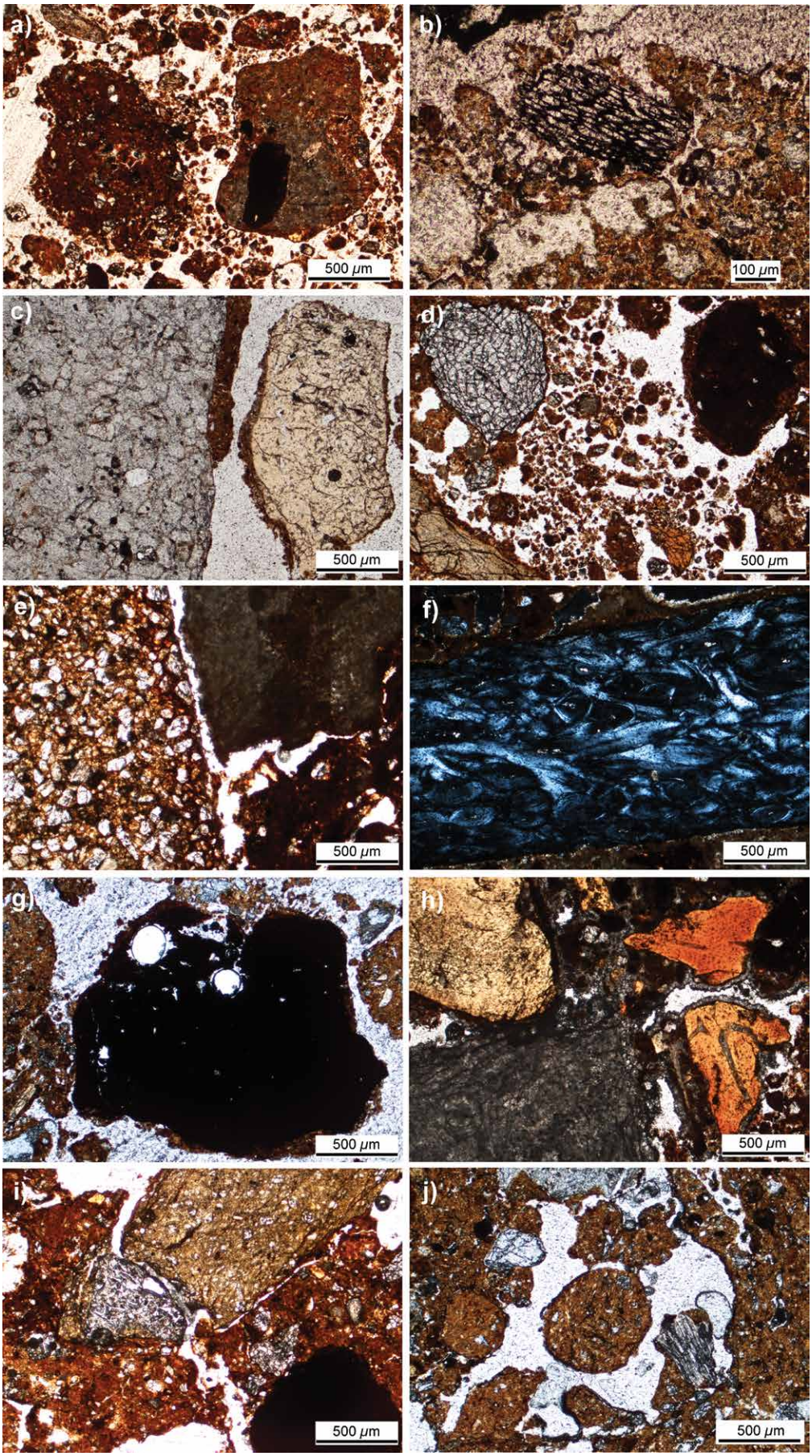

Figure 4. Features of thin sections under the microscope: a) clay aggregates with quartz inclusion (left), Mn-oxide nodule, and light-colored calcareous aggregate with black Mn-oxide inclusion (slide no. N-TLRS-1_A_N_2_a_PPL, in Layer 1); b) a charcoal fragment (centre) surrounded by clay and silt groundmass (slide no. N-TLRS-1_C_W_1_a_100x_PPL, in Layer 1); c) a quartzite fragment (left) and a yellow bone fragment (right) coated with brown clay aggregate containing quartz-silt inclusions (slide no. N-TLRS-2_C_W_1_a_PPL, Layer 2); d) fractured quartz grains (top left), Mn-oxide nodule (top right), yellow and orange bone fragments (bottom left and other areas), and groundmass containing brown clay aggregates with quartz silt inclusions (slide no. N-TLRS-2_C_W_1_b_PPL, Layer 2); e) a sandstone fragment (left), a limestone fragment (top right), and a brown clay aggregate with quartz inclusions (bottom right) (slide no. N-TLRS-5_C_W_3_b_PPL, Layer 3); f) a piece of bone under cross polarization (grey area) with clay groundmass (top and bottom) (slide no. N-TLRS-6_B_E_2_c_XPL, Layer 4); g) a large black Mn-oxide nodule coated with brown clay, and brown clay aggregates (left and right) with a tiny bone fragment and quartz inclusions (slide no. W-TLRS-7_B_N_c_PPL, Layer 5); h) yellow to orange bone fragments disseminated in the slide, some grains coated by tiny calcite grains, grey limestone fragment (lower left) containing a fossil of fusulinid, and groundmass of brown clay particles (slide no. W-TLRS-8_A_W_3_c_PPL, Layer 6); i) reddish brown clay groundmass holding quartz grains, a yellow quartz-silt and clay aggregate (centre top), Mn-oxide (bottom right), and heavily fractured quartz grains (centre) (slide no. W-TLRS-9_C_S_2_a_PPL, Layer 7); j) a yellow brown aggregate with quartz silt inclusions, a large quartz grain (top left), calcite aggregate (top centre), and mica grain showing 1-directional cleavage (centre right) (slide no. W-TLRS-10_B_N_PPL, Layer 8).

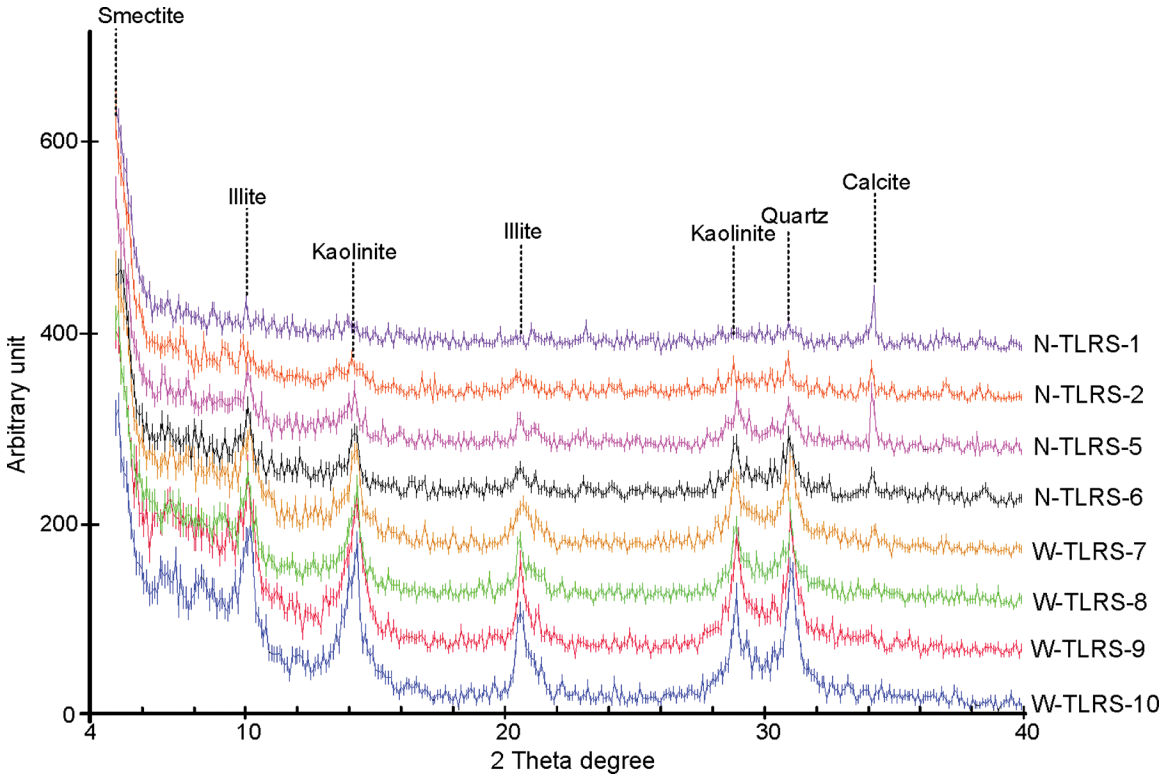

Figure 5. XRD peaks of clay minerals (smectite, illite, and kaolinite), quartz and calcite for sediment samples from different depths.

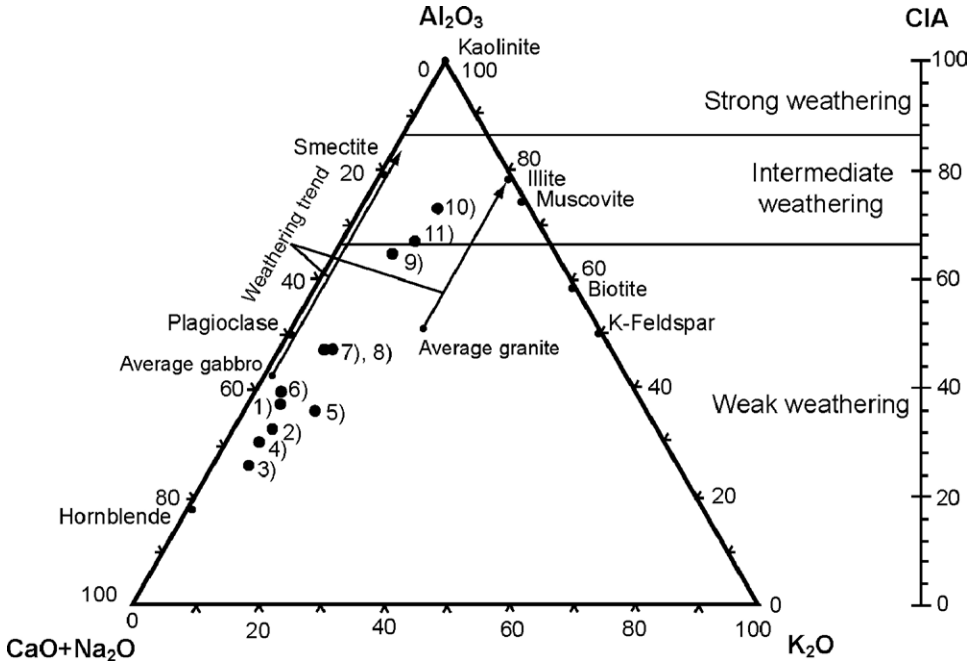

Figure 6. Triangular diagram of CIA using of Al_2O_3, K_2O, and $CaO+Na_2O$ contents (after Nesbitt and Young, 1982; 1984; 1989). [Sample ID/ Depth as in Figure 3].

er quantities of smectite, an aridity-indicative mineral. Conversely, the values of CIA and MAP are less prominent, and quantities of aridity-indicative smectite are higher in the upper zone. These results imply a lower humidity environment in the upper zone.

Other geochemical signatures

Trace elements in unconsolidated sediments are significant for the determination of various parameters, such as weathering intensity, leaching, sediment provenance (Sheldon and Tabor, 2009), and palaeoclimate conditions (Aubert and Pinta, 1977). At this point, the ratios of Ti/Al, Ba/Sr, and other trace elements ascertain the provenance of sediments and palaeoclimate reconstruction.

Ti/Al: provenance and weathering intensity

Ti/Al can be used for tracing sediment provenance; after wt% oxide conversion to molecules of TiO_2 and Al_2O_3. This ratio is significant for parent granitic or basaltic rocks. The Ti concentration may vary between different rock types, while the concentration of Al is relatively constant, but both are immobile. The ratio should remain constant during diagenesis if the pH is 5.5–8 (Sheldon, 2006). Therefore, if this ratio increases, the sediments might come from a more mafic parent. Moreover, the ratio also determines the level of weathering intensity; the lower the ratio is, the higher the leaching process (high weathering intensity), and their provenance possibly contained mudstone and sandstone (Maynard, 1992; Sheldon, 2006) (Fig. 8). Chen et al. (2013) found that Ti/Al decreases due to distance from the parent host. The Ti/Al values are low throughout the profile with an average molar ratio of 0.080, suggesting that the sediments existed under conditions of high weathering intensity.

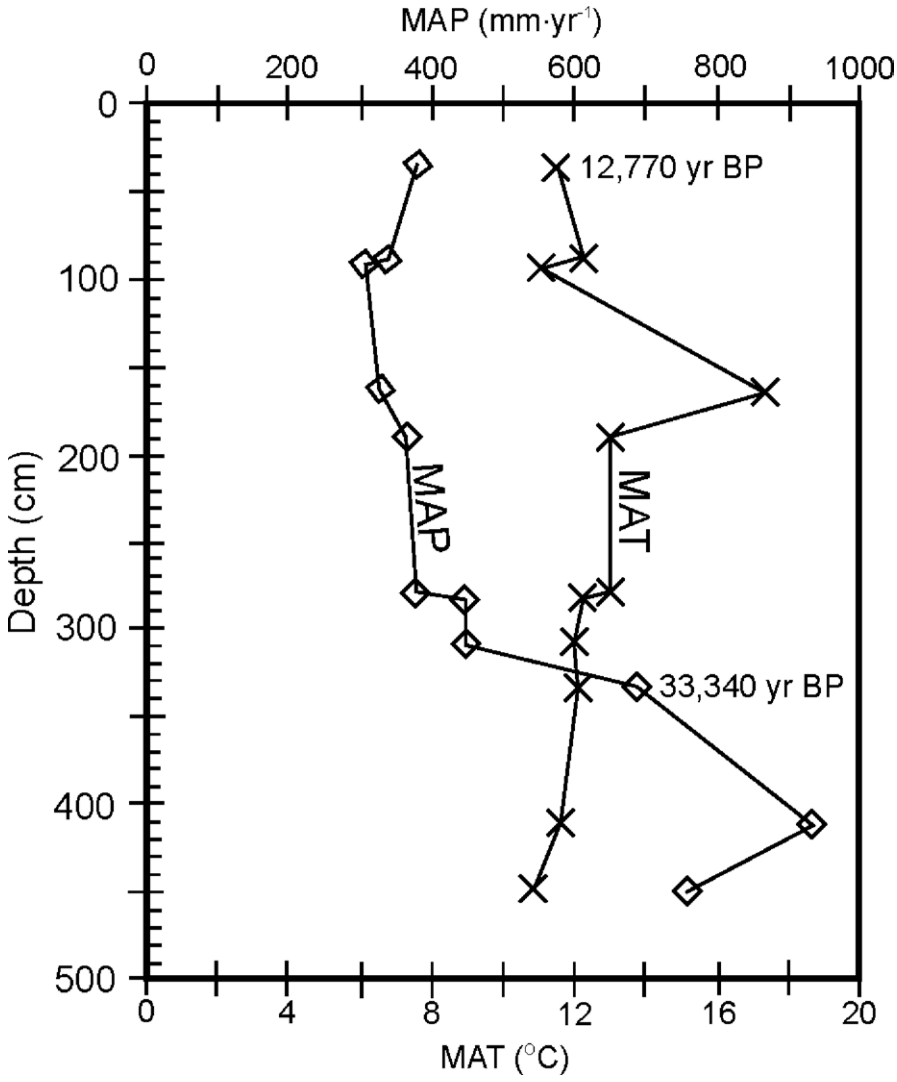

Figure 7. Mean Annual Precipitation (MAP) and Mean Annual Temperature (MAT) of the study site.

Ba/Sr: leaching intensity

Heavily-leached sediments have depleted Ba/Sr ratios, and an increase in value reflects less leaching (Sheldon, 2006). All of our results reveal low Ba/Sr ratios near the top of the profile, while the ratio increases in the lower profile, indicating that most layers of the upper zones were more intensely leached than those in the lower zone. This feature could possibly be caused by rainwater that worked through the profile during diagenesis and over time, as the site is situated in a tropical climate environment.

Other trace elements

Other trace elements, e.g., Ni, V, Rb, and Cr, play significant roles as indicators of the sedimentary environment. Their range may reflect the past humidity conditions in the depositional environment (Aubert and Pinta, 1977) or tropical/humid regions, and some ranges can determine the sediment provenance, as discussed below.

The highest contents of nickel are in ultramafic rocks (e.g., peridotite, dunite: 1,200–2,000 ppm) and their metamorphic products (e.g., serpentinite: 500 ppm), as well as in mafic rocks (e.g., basalt, gabbro: 150 ppm). However, nickel is low in acid rocks (e.g., granite: 5–10 ppm) and in sediments, e.g., sandstones: 90 ppm, loams and clays: 90–100 ppm, loessic loams: 20–30 ppm, calcareous rocks: 10–20 ppm, and certain quartz-like rocks: 2 ppm (Aubert and Pinta, 1977).

Hydromorphic (excess moisture) alluvial sandy clay sediments in Chad and Madagascar contain 20–30 ppm and 45–60 ppm of Ni, respectively. A study in Madagascar found that sandy loam and sandy clay sediments of its flood terrace and alluvial bank contain 178–120 ppm of Ni (Aubert and Pinta, 1977). The Ni contents in this study range from 55 to 99 ppm, with an average of 67 ppm and closely match the alluvial hydromorphic sandy clay sediments located in the tropical/humid regions of Madagascar. The values may be governed by parent rocks.

The parent rock plays an important role in vanadium-bearing sediments (e.g., granite: 3–60 ppm, gneiss: 100–150 ppm, amphibolite: 100–300 ppm, phyllite: 50–200 ppm, mafic material: 200–300 ppm) (Aubert and Pinta, 1977). The V contents of the samples in this study range from 70 to 160 ppm with an average of 119 ppm. Vanadium contents in sediments in tropical/humid regions range from traces to 300 ppm, and leached hydromorphic soil attains 100 ppm. Therefore, the results of the V content from this study may indicate an ancient tropical/humid climate environment.

Rubidium, a rare alkali metal element, is found in rocks at low values (i.e., lithosphere: 3–7 ppm, ultramafic rocks: 2 ppm, mafic volcanic rocks: 45 ppm, acid volcanic rocks: 200 ppm, metamorphic rocks and clays: 200 ppm, sandstone: 60 ppm, and carbonate rocks: 3 ppm) (Turekian and Wedepohl, 1961; Aubert and Pinta, 1977). Rubidium is also found in the soil of humid and tropical regions, ranging from $<$3 to 100 ppm. Our samples contain high Rb values ranging from 81 to 210 ppm with an average of 116 ppm and covering the range of humid/tropical hydromorphic sediments in Madagascar (90–180 ppm; Nalovič, 1969). The values from this study may be affected by the acidic parent rocks.

Parent rocks play a major role in determining Cr content in sediment, and Cr is a relatively stable element. The average values of different rocks include acid eruptive rocks (e.g., granite, charnockite: 20–40 ppm), ultramafic rocks (e.g.,

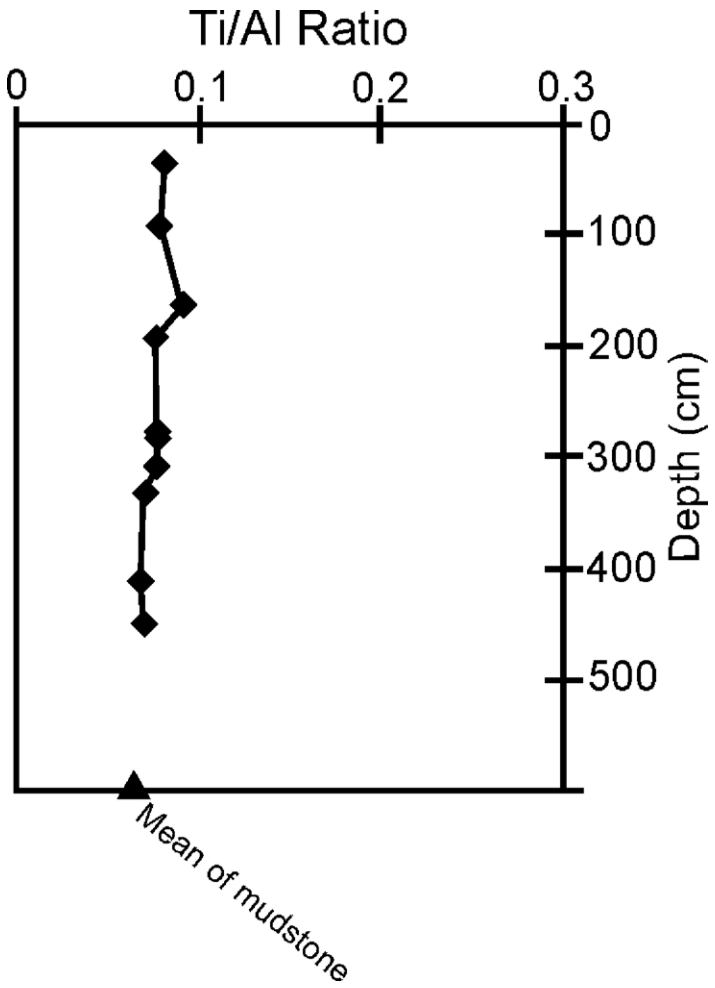

Figure 8 Plot of Ti/Al ratio against profile depth showing sediment provenance (mean values of rocks/soil from Maynard, 1992; Sheldon, 2006). The samples strongly agreed well with a mean of mudstone, suggesting derivation from a high weathering intensity environment.

dunite, peridotite: 2,000–3,000 ppm), and mafic rocks (e.g., basalt, dolerite: 100–300 ppm). Clays contain relatively higher Cr (100–110 ppm) than sandstones and limestones (Vinogradov, 1959; Turekian and Wedepohl, 1961). The results of this study show that Cr contents range from 87 to 192 ppm with an average of 130 ppm and are comparable to the hydromorphic clayey sediments in Chad (80–250 ppm), located in a humid/tropical zone (Aubert and Pinta, 1977).

Tham Lod site in its archaeological regional context

Prehistoric human occupation at the site, as reported by Marwick and Gagan (2011) and Chitkament et al. (2016), produced lithic and faunal remains throughout the profile and ceramics and metal items in the upper layer (Holocene Epoch). The site and the surrounding areas typically contain Hoabinhian assemblages, and the studied site has been classified in the Early Hoabinhian Phase (Kiernan et al., 1988). The Chalcolithic human occupations, which emphasized food production, were abundant according to the Neolithic record in northern Atlantic Spain (Straus, 2018).

Bone fragments and charcoal debris (Fig. 4) are visible in the profile in layers 2–4, >12,770–30,970 yr BP (Marwick and Gagan, 2011), and many thin sections contain bone fragments. Micromorphology provides evidence of profuse bone fragments in layers 3, 4, and 5 (23,050–31,760 yr BP, Marwick and Gagan, 2011), which strongly confirm human occupation from as early as 32,000 yr BP. The archaeological record reveals the involvement of prehistoric humans and palaeoclimate/environment interrelationships. The P_2O_5 values in the sediments at depths between 35 and 283 cm (from samples N-TLRS-1 to W-TLRS-7, 12,770–31,760 yr BP) are higher than those in the lower zone (238 to 450 cm, >31,760 yr BP, Marwick and Gagan, 2011). This result reflects the heavy input of animal and human bones in the site (Kehl et al., 2014) during this period (12,770 to 31,760 yr BP, Marwick and Gagan, 2011). Comparable to this site and dated to this period is the cave in Istria, Croatia, where the uppermost Late Upper Palaeolithic occupation layers 12,460 yr BP contain an abundance of lithic cores, flakes, and tools from local flints (Miracle, 2001).

Humans occupied the upper zone because the environment was less humid and the shelter floor was above the Lang River water as the area became a terrace. The dominant sources of sediments are autochthonous and anthropogenic and develop colluvial deposition under the shelter. Most of the archaeological sites located on the low terraces and bedrock promontories along the main river channel and its tributary streams suggest traditional hunter-gatherer lifestyles supplemented by a pastoral economy (Chlachula and Krupyanko, 2016). Many lithic raw materials were brought to the shelter because the site was a manufactury of stone tools, and fragments (<100 mm) and core stones, mainly grey sandstone, are found. This feature could be interpreted as the prospering of Hoabinhian tools in the period between approximately 26,000 and 20,000 yr BP, while the climate was stable during the Last Glacial Maximum (LGM) (Penny, 2001; Marwick and Gagan, 2011; Chitkament et al., 2016).

Climate changes influence resources and ecology, as well as influence Hoabinhian technology (Marwick, 2013). The lower zones, especially layers 7 and 8 (>34,130 yr BP), contain abundant fluvial pebbles and cobbles; the site was submerged in the palaeoriver Lang, and no human activity evidence is found in this period. New occupations arose during the warm mid-glacial (MIS 3; 55,000–24,000 yr BP) climatic variations marked by the shift in forest vegetation. The Hoabinhian technologies suggest a culture similar to that of the late Pleistocene in north-central Asia (Chlachula, 2017). Favorable environmental conditions during the mid-last glacial interval (30,000–24,000 yr BP) encouraged an expansion of occupations that matched and synchronized with Upper Palaeolithic cultures (Slobodin, 1999; Ponkratova, 2007).

Table 4 Relative quantity of clay minerals and chemical composition of sediment samples at Tham Lod rock shelter.

Sample	N-TLRS-1	N-TLRS-2	W-TLRS-3	W-TLRS-4	N-TLRS-5	N-TLRS-6	W-TLRS-7	W-TLRS-8	W-TLRS-9	W-TLRS-10	W-TLRS-11	Average
Depth of sampling (cm)	35	88	93	164	190	280	283	309	333	412	450	
In layer	1	2	2	3	3	4	5	6	7	8	8	
Age (Year, Marwick and Gargan, 2011)	12,770	N/A	17,510	23,050	24,640	30,970	31,760	33,340	34,130	N/A	N/A	
Relative quantity of clay minerals												
Kaolinite	Small	Trace	Small	Small	Trace	Trace	Small	Small	Moderate	Moderate	Moderate	
Illite	Small	Trace	N/A	Small	Trace	Trace	Small	Small	Small	Small	Moderate	
Smectite	Dominant	Large	N/A	N/A	Large	Large	Moderate	Moderate	Small	Small	N/A	
Major elements (wt%)												
Al_2O_3	13.54	13.46	11.18	15.13	14.67	14.96	15.70	15.52	17.70	17.71	16.14	15.06
Fe_2O_3	7.20	7.28	6.37	10.25	8.39	8.59	8.17	8.03	8.40	8.18	8.05	8.08
P_2O_5	2.86	3.21	4.35	3.76	2.88	3.36	2.38	2.17	0.98	0.44	0.51	2.45
K_2O	3.62	2.14	2.01	2.14	1.86	1.43	2.03	2.08	2.53	2.86	2.74	2.31
MgO	1.52	1.31	1.06	1.54	1.43	1.43	1.30	1.26	1.10	1.10	0.92	1.27
MnO	0.91	0.98	0.85	1.41	1.07	1.06	0.95	0.85	0.94	0.60	0.58	0.93
Na_2O	0.16	0.15	0.13	0.05	0.19	0.17	0.13	0.14	0.09	0.08	0.07	0.12
SiO_2	49.74	44.80	43.55	31.39	45.26	46.08	53.02	53.76	60.20	64.59	64.82	50.65
TiO_2	0.85	0.83	0.69	1.08	0.86	0.90	0.91	0.92	0.97	0.95	0.89	0.90
CaO	19.56	25.84	29.79	33.19	23.37	22.01	15.39	15.25	7.06	3.45	5.23	18.20
Total (Recast to 100%, no LOI)	99.96	100.00	99.99	99.94	100.00	100.00	99.97	99.96	99.96	99.95	99.96	99.97
LOI	16.42	19.67	19.97	N/A	18.57	17.6	14.78	14.48	10.88	8.35	9.13	14.99
Trace elements (ppm.)												
Ni	63	57	62	99	55	57	65	61	72	68	83	67
V	70	88	90	160	94	103	121	122	148	158	160	119
Rb	103	81	84	210	83	82	104	108	131	144	143	116
Y	9	7	51	56	9	8	9	8	12	13	78	24
Nb	1	0	8	41	2	1	3	5	7	9	17	9
Th	N/A	N/A	8	N/A	N/A	N/A	N/A	N/A	N/A	N/A	18	13
Cr	114	97	87	192	101	110	126	128	165	161	148	130
Sr	117	147	175	335	110	94	77	72	53	36	67	117
Ba	219	182	818	N/A	161	171	191	185	232	174	796	313
Sc	57	64	66	N/A	58	58	42	46	21	9	13	43
Zr	168	149	137	379	151	162	188	180	217	231	216	198
CIA Value	36.68	32.36	25.93	29.92	36.6	38.79	47.21	47.02	64.55	73.36	66.6	45.37
Al/Si Ratio	0.16	0.18	0.15	0.28	0.19	0.19	0.17	0.17	0.17	0.16	0.15	0.18
Ti/Al Ratio	0.08	0.079	0.078	0.091	0.075	0.077	0.075	0.076	0.07	0.068	0.07	0.08
Ba/Sr Ratio	1.87	1.24	4.68	N/A	1.45	1.81	2.49	2.57	4.38	4.82	11.96	3.73
MAP (mm/yr)	379	342	309	328	366	377	447	446	687	935	757	488
MAT (°C)	11.5	12.3	11.1	17.3	13.0	13.0	12.2	12.0	12.1	11.6	10.9	12.4

N/A = Not available; CIA = Chemical Index of Alteration; MAP = Mean Annual Precipitation; MAT = Mean Annual Temperature.

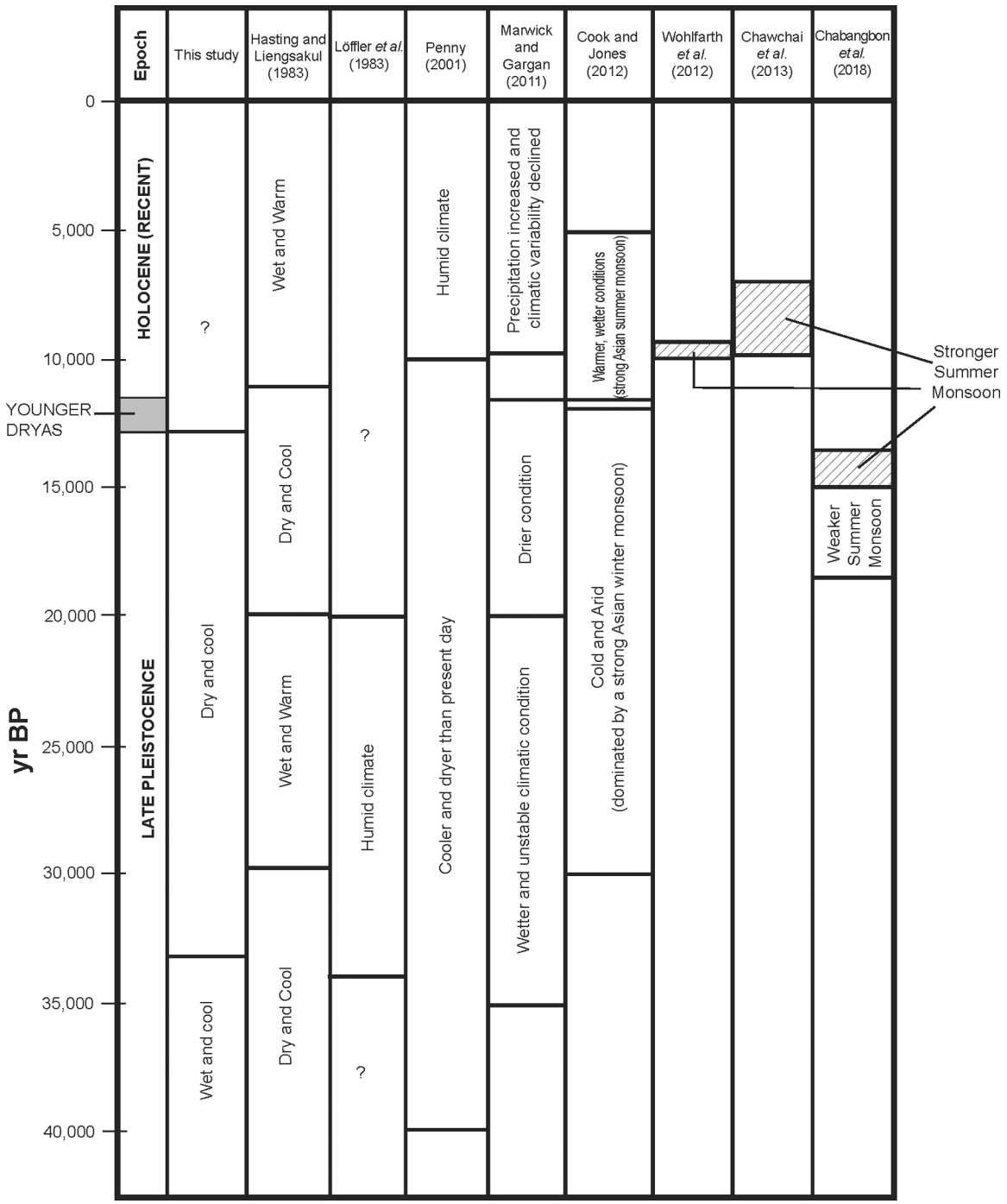

Figure 9 Palaeoclimate from the Late Pleistocene to early Holocene at the study site, compared to other locations in Thailand and Southeast Asia.

Our research demonstrates the linkage between the environment and resource changes during the last millennia of MIS 2 and the first millennia of MIS 1 (Straus, 2018) and related to the cultural changes during the Pleistocene-Holocene transition in this prehistoric archaeological site. Core and flake technology, which appeared periodically, and structured space utilization (MIS 2-3, 30,000–40,000 yr BP), although scarce, indicate migration, dispersion, or increase in human activity in caves such as Longquan cave in the Beiyao site, Henan Province, China (Mellars, 2005; Du et al., 2016; Tang et al., 2017).

Palaeoclimate

Palaeoclimate and palaeoenvironment investigations from continental unconsolidated sediments have been performed by several scholars (e.g., Goldberg, 2000; Courty and Vallverdu, 2001; Woodward and Goldberg, 2001; Woodward et al., 2001; Karkanas, 2002). The data from sediments at Lake Kumphawapi, northeast Thailand, imply the late Pleistocene palaeoclimate of Thailand and Southeast Asia (Hasting and Liengsakul, 1983; Pramojanee and Hastings, 1983; Penny, 2001). Marwick and Gagan (2011) invoked cool and dry climate conditions in the studied site. Our study reveals palaeoclimates between ~34,130 yr BP and ~12,770 yr BP. Palynological study of the glacial-age vegetation in peat profiles from northeast Thailand demonstrates the climatic conditions between 40,000 and 10,000 yr BP, which were cooler and drier than at the present (Penny, 2001). The ^{14}C dating of wood and pollen in sediments showed climate changes in Thailand as follows: 60,000–30,000 yr BP: dry and cool; 30,000–20,000 yr BP: wet and warm; and 20,000–11,000 yr BP: dry and cool (Hasting and Liengsakul, 1983). This sequence can be compared and contrasted with the conclusions in some points, especially in the upper zone of the profile (33,340–12,770 yr

BP, Marwick and Gagan, 2011), showing a mean annual precipitation range (309–447 mm/yr) less than that of the lower zone (≥34,130 yr BP) with an average of 687–935 mm/yr. In the episode before 33,340 yr BP, the area would have been subjected to a wetter climate with an average total precipitation of 935 mm yr^{-1} and a mean annual temperature ranging from 10.88 to 12.13 °C. Oxygen isotope ratios in stalagmites from caves in Socotre Island, Indian Ocean (Burns et al., 2003), suggested that the changes in monsoon precipitation and climate from 42,000 to 55,000 yr BP are linked to varying intensities of tropical convective activity in tropical hydrological cycles in the Indian Ocean and over Southeast Asia. The stalagmites from Yelang Cave, central Guizhou, China (Zhao et al., 2017) showed that from 33,400 to 36,000 yr BP, the area was dry very cold and dry climates with poor vegetation and warming and very wet climates with the best vegetation coverage during 9,000–11,500 yr BP corresponding to a maximum insolation.

Stalagmites from Songjia Cave, central China, (Zhou et al., 2008) showed significant variation in past climate and environment. The coldest climatic phase since the Last Glacial Maximum was clearly recorded between 17,600 and 14,500 yr BP, suggesting that there were synchronous and significant climatic changes across monsoonal China and strong remote connections between the North Atlantic and East Asia regions during the period 20,000–10,000 yr BP. The late Pleistocene palaeoclimate from Sun and Li (1999) in an area of the South China Sea revealed that from the glacial period variations appeared between cool/humid and dry/temperate as climatic cycles on the millennial scale. The climatic condition of 15,000–11,300 yr BP was explained by significant vegetation changes that increased the amount of tropical/subtropical broad-leaved taxa with a spike of mangrove pollen approximately 14,000 yr BP. Moreover, a cold phase lasted from 12,800 to 11,500 yr BP during the Younger Dryas period. This interpretation also explains the climatic conditions of the Holocene Epoch (the last 11,500 yr BP), which are similar to those of the present time (Sun and Li, 1999). The episode fell within the period of the end of the last ice age (~15,000–8000 yr BP), and sea level rise impelled the human population to change their lifestyle from hunting to agriculture (Birch and Linden, 2018). The sea level change during the postglacial period caused substantial changes in the natural environment and human ecology.

However, Figure 9 summarizes and compares the palaeoclimate of Thailand during the period between the late Pleistocene and the early Holocene. Our data indicate that 33,340 to 12,700 yr BP was cooler and drier than the present time, which coincided with the Last Glacial Maximum Period. This result agrees well with certain literature for the same periods e.g., Penny (2001). However, the data from 20,000 to 35,000 yr BP do not seem to agree with Hasting and Liengsakul (1983), Löffler, et al. (1983), and Marwick and Gagan, (2011), which might be the variation of the climate in local areas. The recent average annual rainfall and temperature (30 years, from 1981–2010) at the Pang Mapha station near the study area were 1,200 mm yr^{-1} and 25.5°C, respectively (Climatological Center, Thai Meteorological Department, 2018), compared to the cooler and drier palaeoclimate from this study during the period of 34,130–12,770 yr BP.

After 34,130 yr BP, the MAP ranged from 309 to 447 mm yr^{-1} and the MAT was from 11.1 to 13 °C, which indicates that the LGM affected South East Asia climate and the climate of Pang Mapha area. An abrupt change from a more humid environment to drier conditions, is evidenced by the record in the studied sediments at the depth of 333 cm or about 34,130 yr BP. Before that, the MAP rising up to 935 mm yr^{-1}, which is close to the present value (1,200 mm yr^{-1}), but the MAT is lower than the present value (25.5 °C), suggesting that the present climate in the area is affected by the dense forest. In other words, the vegetation of SEA in the late Pleistocene would have been more abundant than the present time. The forest kept more humidity for the area even the temperature is relatively lower than the present.

Conclusion

Micromorphology, mineralogy, and geochemistry provide distinct and non-distinct data about humidity or wet and dry cycles in the area of Pang Mapha in Mae Hong Son, Thailand and SEA. The data reveal that the late Pleistocene climate was humid and tropical. During the time ≥33,340 yr BP, the climate was wet and cool, and later from 33,340 to 12,770 yr BP, it was drier and cooler than the present day with certain variability to the short warmer/wetter period. Prehistoric humans occupied the site between 33,340 and 12,770 yr BP (during the Last Glacial Maximum Period) which is in agreement with high phosphate contents. The animal and human bones at the site suggest animal hunting by ancient humans.

Acknowledgments

Our special thanks to Nathsuda Pumijumnong, Monthira Yuttitham, and Worachart Wisawapipat for their suggestions to develop this article. This work was supported by Thailand Research Funds, TRF (grant number RDG55H0006). We are in debt to the people, working on the Highland Archeological Project in Pang Mapha, conducted by Rasami Shoocongdej, who facilitated our fieldwork. We thank the students of the Department of General Science, SWU for their help in collecting and analyzing samples as well as the Land Development Department and Royal Irrigation Department for sample analyses. We would also like to thank Simon McIver, Tipa Thep-Ackrapong, Alfredo Villarroel, Kanu Priya Mohan, and Pitthayut Saminpanya who proofread the manuscript. Thanks also go to Richard I. Macphail for his consultation on thin-section identification.

References

Alam, A.K.M.M., Xie, S., Saha, D.K., and Chowdhury, S.Q., 2008, Clay mineralogy of archaeological soil: an approach to paleoclimatic and environmental reconstruction of the archaeological sites of the Paharpur area, Badalgacchiupazila, Naogaon district, Bangladesh: Environmental Geology, v. 53, p. 1639–1650. https://doi.org/10.1007/s00254-007-0771-1

Aubert, H., and Pinta, M., 1977, Trace elements in soils: New York, Elsevier Scientific, 394 p.

Bedaiwy, M.N.A., 2012, A simplified approach for determining the hydrometer's dynamic settling depth in particle-size analysis: Catena, v. 97, p. 95–103. https://doi.org/10.1016/j.catena.2012.05.010

Bengtsson, L., and Enell, M., 1986, Chemical analysis, *in* Berglund, B.E., ed., Handbook of Holocene Palaeoecology and Palaeohydrology: Chichester, John Wiley & Sons Ltd., p. 423–451.

Bhattacharyya, T., Pal, D.K., and Deshpande, S.B., 1993, Genesis and transformation of minerals in the formation of red (Alfisols) and black (Inceptisols and Vertisols) soils on Deccan basalt in the Western Ghats, India: Journal of Soil Science, v. 44, p. 159–171. https://doi.org/10.1111/j.1365-2389.1993.tb00442.x

Birch, S.E.P., and Linden, M.V., 2018, A long hard road… Reviewing the evidence for environmental change and population history in the eastern Adriatic and western Balkans during the Late Pleistocene and Early Holocene: Quaternary International, v. 465, p. 177-191. https://doi.org/10.1016/j.quaint.2016.12.035

Blokhuis, W.A., Kooistra, M.J., and Wilding, L.P., 1990, Micromorphology of cracking clayey soils (Vertisols), *in* Douglas, L.A., ed., Micromorphology: A Basic and Applied Science. Developments in Soil Science, Volume 19: Amsterdam, Elsevier, p. 123–148. https://doi.org/10.1016/S0166-2481(08)70323-4

Blokhuis, W.A., Pape, T., and Slager, S., 1969, Morphology and distribution of pedogenic carbonate in some Vertisols of the Sudan: Geoderma, v. 2, p. 173–200. https://doi.org/10.1016/0016-7061(69)90037-8

Burns, S.J., Fleitmann, D., Matter, A., Kramers, J., and Al-Subbary, A.A., 2003, Indian Ocean Climate and an Absolute Chronology Over Dansgaard/Oeschger Events 9 to 13: Science, v. 301, p. 1365–1367. https://doi.org/10.1126/science.1086227

Chabangbon, A., Yamoah, K.K.A., Phantuwongraj, S., and Choowong, M., 2018, Climate in Sundaland and Asian monsoon variability during the last deglaciation: Quaternary International, v. 479, p. 141–147. https://doi.org/10.1016/j.quaint.2017.04.017

Chamley, H., 1989, Clay Sedimentology: Heidelberg, Springer–Verlag., 644 p. https://doi.org/10.1007/978-3-642-85916-8

Chawchai, S., Chabangborn, A., Kylander, M., Löwemark, L., Mörth, C.-M., Blaauw, M., Klubseang, W., Reimer, P.J., Fritz, S.C., and Wohlfarth, B., 2013, Lake Kumphawapi – an archive of Holocene palaeoenvironmental and palaeoclimatic changes in northeast Thailand: Quaternary Science Reviews, v. 68, p. 59–75. https://doi.org/10.1016/j.quascirev.2013.01.030

Chen, H.-F., Yen, P.-Y., Song, S.-R., Hsu, S.C., Yang, T.N., Wang, Y., Chi, Z., Lee, T.-Q., Chen, M.-T., Cheng, C.-L., Zou, J., and Chang, Y.-P., 2013, The Ti/Al molar ratio as a new proxy for tracing sediment transportation processes and its application in aeolian events and sea level change in East Asia: Journal of Asian Earth Sciences, v. 73, p. 31–38. https://doi.org/10.1016/j.jseaes.2013.04.017

Chitkament, T., Gaillard, C., and Shoocongdej, R., 2016, Tham Lod rock shelter (Pang Mapha district, north-western Thailand): Evolution of the lithic assemblages during the Late Pleistocene: Quaternary International, v. 416, p. 151–161. https://doi.org/10.1016/j.quaint.2015.10.058

Chlachula, J., 2017, Chronology and environments of the Pleistocene peopling of North Asia: Archaeological Research in Asia, v. 12, p. 33–53. https://doi.org/10.1016/j.ara.2017.07.006

Chlachula, J., and Krupyanko, A.A., 2016, Sequence stratigraphy and environmental background of the late Pleistocene and Holocene occupation in the Southeast Primor'ye (the Russian Far East): Quaternary Science Reviews, v. 142, p. 120–142. https://doi.org/10.1016/j.quascirev.2016.03.018

Clemens, S.C., Prell, W.L., and Sun, Y., 2010, Orbital-scale timing and mechanisms driving Late Pleistocene Indo□Asian summer monsoons: Reinterpreting cave speleothem $\delta^{18}O$: PALEOCEANOGRAPHY, v. 25, p. 1–19. https://doi.org/10.1029/2010PA001926

Climatological Center, Thai Meteorological Department, 2018, Mae Hong Son Climate, [WWW Document], n.d. URL http://climate.tmd.go.th/data/province/เหนือ/ภูมิอากาศแม่ฮ่องสอน.pdf (accessed on 24 June 2018).

Cook, C.G., and Jones, R.T., 2012, Palaeoclimate dynamics in continental Southeast Asia over the last ~30,000 Cal yrs BP: Palaeogeography, Palaeoclimatology, Palaeoecology, v. 339–341, p. 1–11. https://doi.org/10.1016/j.palaeo.2012.03.025

Courty, M.A., and Vallverdu, J., 2001, The microstratigraphic record of abrupt climate changes in cave sediments of the Western Mediterranean: Geoarchaeology, v. 16, p. 467–499. https://doi.org/10.1002/gea.1002

Dean, W.E.Jr., 1974, Determination of carbonate and organic matter in calcareous sediments and sedimentary rocks by loss on ignition: Comparison with other methods: Journal of Sedimentary Petrology, v. 44, p. 242–248. https://doi.org/10.1306/74D729D2-2B21-11D7-8648000102C1865D

Department of Mineral Resources, Thailand, 2017, Geological Map 1:250,000 (http://wms2.dmr.go.th/gisdmr_kml.html) (accessed on 29 November 2018).

Dixon, J.B., and Weed, S.B., 1989, Minerals in soil environments, 2nd ed.: Madison, Soil Science Society of America, 89 p. https://doi.org/10.2136/sssabookser1.2ed.c5

Du, S., Li, X., Zhou, L., Pang, H., Bar-Yosef, O., and Wu, X., 2016, Longquan Cave: an early Upper Palaeolithic site in Henan Province, China: Antiquity, v. 90, p. 876–893. https://doi.org/10.15184/aqy.2016.108

Goldberg, P., 2000, Micromorphology and site formation at Die Kelders Cave I, South Africa: Journal of Human Evolution, v. 38, p. 43–90. https://doi.org/10.1006/jhev.1999.0350

Hamer, J.M., Sheldon, N.D., and Nichols, G.J., 2007, Global aridity during the Early Miocene? A terrestrial palaeoclimate record from the Ebro Basin, Spain: The Journal of Geology, v. 115, p. 601–608. https://doi.org/10.1086/519780

Hasting, P.J., and Liengsakul, M., 1983, Chronology of the late Quaternary climatic changes in Thailand, *in* Proceedings, The First Symposium on *Geomorphology* and Quaternary Geology of Thailand: Bangkok, Department of Geology, Chulalongkorn University, p. 24–34.

Heiri, O., Lotter, A.F., and Lemcke, G., 2001, Loss on ignition as a method for estimating organic and carbonate content in sediments: reproducibility and comparability of results: Journal of Paleolimnology, v. 25, p. 101–110. https://doi.org/10.1023/A:1008119611481

Hong, H., Gu, Y., Yin, K., Wang, C., and Li, Z., 2013, Clay record of climate change since the mid- Pleistocene in Jiujiang, south China: Boreas, v. 42, p. 173–183. https://doi.org/10.1111/j.1502-3885.2012.00276.x

Iacoviello, F., and Martini, I., 2013, Clay minerals in cave sediments and *terra rossa* soils in the Montagnola Senese karst massif (Italy): Geological Quarterly, v. 57, p. 527–536. https://doi.org/10.7306/gq.1111

Jackson, M.L., 2005, Soil Chemical Analysis: Advanced course, revised 2nd ed.: Medison, Parallel Press, 930 p.

Kabakchiev, I., and Galeva, V., 1973, Comparative micromorphological investigation of cernozemsmonitzas and chernozems [in Bulgarian]: Pochvoznanie i Agrokhimiya, v. 8, p. 11–24.

Karkanas, P., 2002, Micromorphological studies of Greek prehistoric sites, New insights in the interpretation of the archaeological record: Geoarchaeology, v. 17, p. 237–259. https://doi.org/10.1002/gea.10012

Kehl, M., Eckmeier, E., Franz, S.O., Lehmkuhl, F., Soler, J., Soler, N., Reicherter, K., and Weniger, G.C., 2014, Sediment sequence and site formation processes at the Arbreda Cave, NE Iberian Peninsula, and implications on human occupation and climate change during the Last Glacial: Climate of the Past, v. 10, p. 1673–1692. https://doi.org/10.5194/cp-10-1673-2014

Khaokhiew, C., 2003, Geoarchaeology: site formation process of Tham Lod rock shelter, Pang Mapha District, Mae Hong Son Province [M.Sc. thesis]. Bangkok, Silpakorn University. 164 p. (in Thai).

Kiernan, K., Spies, J., and Dunkley, J., 1988, Prehistoric occupation and burial sites in the mountains of the Nam Khong area, Mae Hong Son province, northwestern Thailand: Australian Archaeology, v. 27, p. 24-44. https://www.jstor.org/stable/40286659

Krauskopf, K., and Bird, D.K., 1995, Introduction to Geochemistry, 3rd ed.: New York, McGraw-Hill, Inc., 640 p.

Löffler, E., Thaompson, W.P., and Liengsakul, M., 1983, Geomorphological development of the Tung Kula Ronghai, *in* Proceedings, The First Symposium on *Geomorphology* and Quaternary Geology of Thailand: Bangkok, Department of Geology, Chulalongkorn University, p. 123–130.

Marwick, B., 2013, Multiple Optima in Hoabinhian flaked stone artifact palaeoeconomics and palaeoecology at two archaeological sites in Northwest Thailand: Journal of Anthropological Archaeology, v. 32, p. 553–564**.** https://doi.org/10.1016/j.jaa.2013.08.004

Marwick, B., and Gagan, M.K., 2011, Late Pleistocene monsoon variability in northwest Thailand: an oxygen isotope sequence from the bivalve *Margaritanopsis laosensis* excavated in Mae Hong Son province: Quaternary Science Reviews, v. 30, p. 3088–3098. https://doi.org/10.1016/j.quascirev.2011.07.007

Maynard, J.B., 1992, Chemistry of modern soils as a guide to interpreting Precambrian palaeosols: The Journal of Geology, v. 100, p. 279–289. https://doi.org/10.1086/629632

Mellars, P., 2005, The impossible coincidence. A single-species model for the origins of modern human behavior in Europe: Evolutionary Anthropology, v. 14, p. 12–27. https://doi.org/10.1002/evan.20037

Miracle, P., 2001, Feast or Famine? Epi-Paleolithic subsistence in the northern Adriatic basin: Documenta Praehistorica, v. 26, p. 177–197. https://doi.org/10.4312/dp.28.10

Muangsong, C., Cai, B., Pumijumnong, N., Hu, C., and Cheng, H., 2014, An annually laminated stalagmite record of the changes in Thailand monsoon rainfall over the past 387 years and its relationship to IOD and ENSO: Quaternary International, v. 349, p. 90–97. https://doi.org/10.1016/j.quaint.2014.08.037

Munsell Color (Firm), 2012, Munsell soil color charts: with genuine Munsell color chips. Grand Rapids, MI: Munsell Color.

Nalovič, L., 1969, Etude spectrographique des éléments traces et leur distribution dans quelques types de sols de Madagascar: Cahiers ORSTOM.Série Pédologie , v. VII, p. 133–181.

Nesbitt, H.W., and Young, G.M., 1982, Early Proterozoic climates and plate motions inferred from major element chemistry of lutites: Nature, v. 299, p. 715-717. http://dx.doi.org/10.1038/299715a0

Nesbitt, H.W., and Young, G.M., 1984, Prediction of some weathering trends of plutonic and volcanic rocks based on thermodynamic and kinetic considerations: Geochimica et Cosmochimica Acta, v. 48, p. 1523–1534. https://doi.org/10.1016/0016-7037(84)90408-3

Nesbitt, H.W., and Young, G.M., 1989, Formation and diagenesis of weathering profiles: The Journal of Geology, v. 97, p. 129–147. https://doi.org/10.1086/629290

Pal, D.K., 2014, Clay and other minerals in soils and sediments as evidence of climate change: A review: Gondwana Geological Magazine, v. 29, p. 87–94.

Pal, D.K., Deshpande, S.B., Venugopal, K.R., and Kalbande, A.R., 1989, Formation of di- and trioctahedral smectite as evidence for paleoclimatic changes in southern and central peninsular India: Geoderma, v. 45, p. 175–184. https://doi.org/10.1016/0016-7061(89)90049-9

Penny, D., 2001, A 40,000 year palynological record from north-east Thailand; implications for biogeography and palaeo-environmental reconstruction: Palaeogeography, Palaeoclimatology, Palaeoecology, v. 171, p. 97–128. https://doi.org/10.1016/S0031-0182(01)00242-5

Ponkratova, I.Yu., 2007, Ushki 5 Site (Kamchatka): recent investigations, problems and perspectives (the Palaeolithic Period): Kolymskyy Gumanitarnyy Almanach, v. 2007, p. 13–20 (in Russian).

Pramojanee, P., and Hastings, P.J., 1983, Geomorphological and palynological investigation of sea level changes in Chantaburi, SE Thailand, *in* Proceedings, The First Symposium on *Geomorphology* and Quaternary Geology of Thailand: Bangkok, Department of Geology, Chulalongkorn University, p. 35–51.

Retallack, G.J., 2000, Depth to pedogenic carbonate horizon as a palaeoprecipitation indicator? Comment and Reply COMMENT: Geology, v. 28, p. 572–572. https://doi.org/10.1130/0091-7613(2000)28<572a:DTPCHA>2.0.CO;2

Royal Thai Survey Department, 1999, Topographic Map, Series L7018, Sheet 4648 II – Doi Phak Kut, Scale 1:50,000, Bangkok, Thailand.

Santisteban, J.I., Mediavilla, R., López-Pamo, E., Dabrio, C.J., Zapata, M.B.R., García, M.J.G., Castaño, S., and Martínez-Alfaro, P.E., 2004, Loss on ignition: a qualitative or quantitative method for organic matter and carbonate mineral content in sediments?: Journal of Palaeolimnology, v. 32, p. 287–299. https://doi.org/10.1023/B:JOPL.0000042999.30131.5b

Selley, R.C., 1985, Ancient Sedimentary Environments and their sub-surface diagnosis, 3rd ed.: London, Chapman & Hall, 317 p. https://doi.org/10.1007/978-1-4615-5421-9

Sheldon, N.D., 2006, Abrupt chemical weathering increase across the Permian–Triassic boundary: Palaeogeography, Palaeoclimatology, Palaeoecology, v. 231, p. 315–321. https://doi.org/10.1016/j.palaeo.2005.09.001

Sheldon, N.D., and Tabor, N.J., 2009, Quantitative palaeoenvironmental and palaeoclimatic reconstruction using palaeosols: Earth-Science Reviews, v. 95, p. 1–52. https://doi.org/10.1016/j.earscirev.2009.03.004

Shepard, F.P., 1954, Nomenclature based on sand-silt-clay ratios: Journal of Sedimentary Research, v. 24, p. 151–158. https://doi.org/10.1306/D4269774-2B26-11D7-8648000102C1865D

Sleeman, J.R., and Brewer, R., 1984, Micromorphology of some Australian cracking clay soils: *in* McGarity, J.W., Hoult, E.H., and So, H.B., eds., Properties and Utilization of Cracking Clay Soils, Reviews in Rural Sciences 5: University of New England, Armadale, Australia, p. 73–82.

Slobodin, S.B., 1999, Archaeology of Kolyma and Continental Priokhotye in Late Pleistocene and Early Holocene: NEISRI FEB RAS (in Russian): North-Eastern Federal University; North-East Interdisciplinary Science Research Institute, Magadan, 234 p. (in Russian).

Stoops, G., Marcelino, V., and Mees, F., eds., 2010, Interpretation of micromorphological features of soils and regoliths: Amsterdam, Elsevier, 752 p. https://doi.org/10.1016/C2009-0-18081-9

Straus, L.G., 2018, Environmental and cultural changes across the Pleistocene-Holocene transition in Cantabrian Spain: Quaternary International, v. 465, p. 222–233. https://doi.org/10.1016/j.quaint.2016.10.005

Sun, X., and Li, X., 1999, A pollen record of the last 37 ka in deep sea core 17940 from the northern slope of the South China Sea: Marine Geology, v. 156, p. 227–244. https://doi.org/10.1016/S0025-3227(98)00181-9

Tang, Z., Du, S, and Liu, F., 2017, Late Pleistocene changes in vegetation and the associated human activity at Beiyao Site, Central China: Review of Palaeobotany and Palynology, v. 244, p. 107–112. https://doi.org/10.1016/j.revpalbo.2017.04.002

Tawornpruek, S., Kheoruenromne, I., Suddhiprakarn, A., and Gilkes, R., 2006, Microstructure and water retention of Oxisols in Thailand: Soil Research, v. 43, p. 973–986. https://doi.org/10.1071/SR05039

Tsuji, G.Y., Watanabe, R.T., and Sakai, W.S., 1975, Influence of soil microstructure on water characteristics of selected Hawaiian soils: Soil Science Society of America Journal, v. 39, p. 28–33. https://doi.org/10.2136/sssaj1975.03615995003900010011x

Turekian, K.K., and Wedepohl, K.H., 1961, Distribution of the elements in some major units of the Earth's crust: Geological Society of America Bulletin, v. 72, p. 175-192. https://doi.org/10.1130/0016-7606(1961)72[175:DOTEIS]2.0.CO;2

Vinogradov, A.P., 1959, The Geochemistry of Rare and Dispersed Chemical Elements in Soils, 2nd ed. (translated from Russian): New York, Consultants Bureau, 209 p.

Wohlfarth, B., Klubseang, W., Inthongkaew, S., Fritz, S.C., Blaauw, M., Reimer, P.J., Chabangborn, A., Löwemark, L., and Chawchai, S., 2012, Holocene environmental changes in northeast Thailand as reconstructed from a tropical wetland: Global and Planetary Change, v. 92–93, p. 148–161. https://doi.org/10.1016/j.gloplacha.2012.05.008

Woodward, J.C., and Goldberg, P., 2001, The sedimentary records in Mediterranean rock shelters and caves: Archives of environmental change: Geoarchaeology, v. 16, p. 327–354. https://doi.org/10.1002/gea.1007

Woodward, J.C., Hamlin, R.H.B., Macklin, M.G., Karkanas, P., and Kotjabopoulou, E., 2001, Quantitative sourcing of slackwater deposits at Boila rock shelter: A record of late glacial flooding and palaeolithic settlement in the Pindus Mountains, Northwest Greece: Geoarchaeology, v. 16, p. 501–536. https://doi.org/10.1002/gea.1003

Zhou, H., Zhao, J., Feng, Y., Gagan, M.K., Zhou, G., and Yan, J., 2008, Distinct climate change synchronous with Heinrich event one, recorded by stable oxygen and carbon isotopic compositions in stalagmites from China: Quaternary Research, v. 69, p. 306–315. https://doi.org/10.1016/j.yqres.2007.11.001

Zhao, M., Li, H.-C., Shen, C.-C., Kang, S.-C., and Chou, C.-Y., 2017, $\delta^{18}O$, $\delta^{13}C$, elemental content and depositional features of a stalagmite from Yelang Cave reflecting climate and vegetation changes since late Pleistocene in central Guizhou, China: Quaternary International, v. 452, p. 102–115. https://doi.org/10.1016/j.quaint.2016.07.022

GUIDE TO AUTHORS

The *Journal of Cave and Karst Studies* is a multidisciplinary journal devoted to cave and karst research. The *Journal* is seeking original, unpublished manuscripts concerning the scientific study of caves or other karst features. Authors do not need to be members of the National Speleological Society, but preference is given to manuscripts of importance to North American speleology.

LANGUAGES: The *Journal of Cave and Karst Studies* uses American-style English as its standard language and spelling style, with the exception of allowing a second abstract in another language when room allows. In the case of proper names, the *Journal* tries to accommodate other spellings and punctuation styles. In cases where the Editor-in-Chief finds it appropriate to use non-English words outside of proper names (generally where no equivalent English word exist), the *Journal* italicizes them. However, the common abbreviations i.e., e.g., et al., and etc. should appear in roman text. Authors are encouraged to write for our combined professional and amateur readerships

CONTENT: Each paper will contain a title with the authors' names and addresses, an abstract, and the text of the paper, including a summary or conclusions section. Acknowledgments and references follow the text. Manuscripts should be limited to 6,000 words and no more than 10 figures and 5 tables. Larger manuscripts may be considered, but the *Journal* reserves the right to charge processing fees for larger submissions.

ABSTRACTS: An abstract stating the essential points and results must accompany all articles. An abstract is a summary, not a promise of what topics are covered in the paper.

STYLE: The *Journal* consults The Chicago Manual of Style on most general style issues.

REFERENCES: In the text, references to previously published work should be followed by the relevant author's name and date (and page number, when appropriate) in brackets. All cited references are alphabetical at the end of the manuscript with senior author's last name first, followed by date of publication, title, publisher, volume, and page numbers. Geological Society of America format should be used (see http://www.geosociety.org/documents/gsa/pubs/GSA_RefGuide_Examples.pdf). Please do not abbreviate periodical titles. Web references are acceptable when deemed appropriate. The references should follow the style of: Author (or publisher), year, Webpage title: Publisher (if a specific author is available), full URL (e.g., http://www.usgs.gov/citguide.html), and the date the website was accessed in brackets. If there are specific authors given, use their name and list the responsible organization as publisher. Because of the ephemeral nature of websites, please provide the specific date. Citations within the text should read: (Author, Year).

SUBMISSION: Manuscripts are to be submitted via the PeerTrack submission system at http://www.edmgr.com/jcks/. Instructions are provided at that address. At your first visit, you will be prompted to establish a login and password, after which you will enter information about your manuscript and upload your manuscript, tables, and figure files. Manuscript files can be uploaded as DOC, WPD, RTF, TXT, or LaTeX. Note: LaTeX files should not use any unusual style files; a LaTeX template and BiBTeX file may be obtained from the Editor-in-Chief. Table files can be uploaded as DOC, WPD, RTF, TXT, or LaTeX files and figure files can be uploaded as TIFF, AI, EPS, or CDR files. Extensive supporting data may be placed on the Journal's website as supplemental material at the discretion of the Editor-in-Chief. The data that are used within a paper must be made available upon request. Authors may be required to provide supporting data in a fundamental format, such as ASCII for text data or comma-delimited ASCII for tabular data.

DISCUSSIONS: Critical discussions of papers previously published in the *Journal* are welcome. Authors will be given an opportunity to reply. Discussions and replies must be limited to a maximum of 1000 words and discussions will be subject to review before publication. Discussions must be within 6 months after the original article appears.

MEASUREMENTS: All measurements will be in Systeme Internationale (metric) except when quoting historical references. Other units will be allowed where necessary if placed in parentheses and following the SI units.

FIGURES: Figures and lettering must be neat and legible. Figure captions should be on a separate sheet of paper and not within the figure. Figures should be numbered in sequence and referred to in the text by inserting (Fig. x). Most figures will be reduced, hence the lettering should be large. Photographs must be sharp and high contrast. Figures must have a minimum resolution of 300 dpi for acceptance. Please do not submit JPEG images.

TABLES: See http://caves.org/pub/journal/PDF/Tables.pdf to get guidelines for table layout.

COPYRIGHT AND AUTHOR'S RESPONSIBILITIES: It is the author's responsibility to clear any copyright or acknowledgement matters concerning text, tables, or figures used. Authors should also ensure adequate attention to sensitive or legal issues such as land owner and land manager concerns or policies and cave location disclosures.

PROCESS: All submitted manuscripts are sent out to at least two experts in the field. Reviewed manuscripts are then returned to the author for consideration of the referees' remarks and revision, where appropriate. Revised manuscripts are returned to the appropriate Associate Editor who then recommends acceptance or rejection. The Editor-in-Chief makes final decisions regarding publication. Upon acceptance, the senior author will be sent one set of PDF proofs for review. Examine the current issue for more information about the format used.

Journal of Cave and Karst Studies

Volume 82 Number 1 March 2020

CONTENTS

Article 1
Sinkhole Susceptibility Assessment based on Morphological, Imagery, and Contextual Attributes Derived from Gis and Imagery Data
Xiaomin Qiu, Shuo-Sheng Wu, and Yan Chen

Article 18
Dynamics of Collembola (Hexapoda) in a Forested Limestone Scree Slope, Western Carpathians, Slovakia
Michal Rendoš, Dana Miklisová, Ľubomír Kováč, and Andrej Mock

Article 31
A Reactivated Cave System Induces Rapidly Developing Cover-Collapse Sinkholes in Tasmania, Australia
Bianca Burke, Adrian Slee, Peter D. Mcintosh, Harald Hofmann, and James Shulmeister

Article 51
Micromorphology, Mineralogy, and Geochemistry of Sediments at the Tham Lod Rock Shelter Archaeological Site in Mae Hong Son, Thailand: Suggestions of a late Pleistocene Climate
Seriwat Saminpanya and Nopporn Denkitkul